UNIMORE
UNIVERSITÀ DEGLI STUDI DI
MODENA E REGGIO EMILIA

Department of Engineering "Enzo Ferrari"

Doctorate School in Information and Communication Technologies (ICT) - XXXVIII Cycle

---

Advanced Control Architecture for Physical Human-Robot Interaction in Rehabilitative and Surgical Robotics

---

Candidate:
Dario Onfiani

Supervisor:
Prof. Luigi Biagiotti

Coordinator:
Prof. Luigi Rovati

Academic Year 2024-2025

Index

List of Figures

List of Tables

List of Acronyms

AAN assist-as-needed. 20, 25, 69, 70

ADL Activities of Daily Living. 3, 66, 69, 87, 96

cobot collaborative robot. 2, 3, 4, 5, 67

DMP Dynamic Movement Primitive. 17, 68

DoF degrees of freedom. 14, 15

DS Dynamical System. 17

DTW Dynamic Time Warping. 27, 28, 29, 30

EMG Electromyography. iv, 2, 6, 7, 26, 98

FRVF Forbidden Region Virtual Fixture. i, 10, 11, 14, 19, 67

GMM Gaussian Mixture Model. 18

GMR Gaussian Mixture Regression. 29, 30

GVF Guidance Virtual Fixture. i, 9, 10, 14, 25, 26, 67

HIC Hybrid Impedance Control. 7, 68, 71, 83, 84, 124

IQR Interquartile Range. 114, 115

KT Kinesthetic Teaching. 1, 4, 13, 14, 25, 101, 102, 104, 105, 113

LbD Learning by Demonstration. 1, 2, 4, 6, 7, 13, 27, 32, 68

LMM Linear Mixed Model. 113, 117

LTB Lübeck Toolbox. 111

MAV Mean Absolute Value. 107

MIS Minimally Invasive Surgery. 3, 14, 99

NASA-TLX NASA Task Load Index. 2

OR Operating Room. 110

PF Potential Field. 16

pHRI Physical Human-Robot Interaction. 1, 2, 3, 4, 5, 6, 11, 12, 33, 35, 36, 42, 48, 67

R&D Resection and Dissection. ix, 2, 3, 26, 100, 101, 102, 103, 109, 121

RASS Robotically Assisted Surgical Systems. 100

RCM Remote Center of Motion. 14

RL Reinforcement Learning. 18

SSA Spatial Sampling Algorithm. 1, 2, 5, 6, 7, 25, 27, 28, 29, 30, 31, 32, 35, 76, 88, 89, 123

SUS System Usability Scale. 112, 117

TCP Tool Center Point. x, 102, 105, 112, 113, 116

TDPC Time-Domain Passivity Controllers. 125

VF Virtual Fixture. x, 1, 2, 4, 5, 6, 7, 9, 12, 14, 19, 21, 22, 35, 49, 64, 67

Abstract

The increasing prevalence of Physical Human-Robot Interaction (pHRI) and collaborative robots (cobots) presents new opportunities in high-specialization fields, particularly in clinical and medical settings. However, enabling non-expert users, such as therapists and surgeons, to effectively leverage these technologies requires systems that are intuitive to program, safe to interact with, and highly specialized for the given task. Several methods can be considered in order to facilitate users who are not familiar with cobots. In particular, this thesis proposes to consider a comprehensive framework for advanced VF, based on an admittance control logic, that allows to face the above mentioned challenges.

The framework's foundation addresses intuitive robot programming. Beginning with a Learning by Demonstration (LbD) approach based on Kinesthetic Teaching (KT), this thesis introduces a novel solution to the fundamental problem of trajectory misalignment. The developed Spatial Sampling Algorithm (SSA) decouples a trajectory's geometry from its temporal execution. By producing an arc-length-based representation, the SSA generates a regular curve that inherently prevents the "stagnation" phenomenon—a common failure mode in time-dependent methods—thereby ensuring a fluid and robust time-agnostic interaction.

The theoretical core of this thesis lies in the rigorous analysis and design of specialized VFs, a topic also explored in-depth in a dedicated survey. A fundamental contribution is the formal stability analysis for constrained admittance controllers, a critical aspect of safe pHRI. This analysis incorporates real-world non-idealities often overlooked, such as joint elasticity, system delays, and actuator saturation. Using Nyquist analysis and the describing function method, it is demonstrated how these effects combine to create limit cycles and undesired oscillations. Furthermore, this discussion directly informs a novel parameter adaptation strategy, designed to maximize user transparency by minimizing perceived effort, while guaranteeing system stability under all operating conditions.

This robust theoretical and methodological framework is then validated in two complex clinical applications. For Rehabilitative Robotics, a complete system for upper-limb therapy was developed. This includes a novel optimization

method for cobot placement based on a payload index to maximize therapeutic efficacy. The system implements a virtual channel with non-linear elastic forces, uniquely combining soft guidance within the channel with hard, boundary-based constraints. Experimental validation, including user-perception analysis (NASA Task Load Index (NASA-TLX)), confirmed a reduction in interaction forces and perceived workload compared to standard methods.

For Surgical Robotics, an anisotropic VF was designed specifically for delicate Resection and Dissection (R&D) procedures. This specialized VF preserves freedom of movement along the task-relevant line while constraining orthogonal directions to enhance safety. To overcome the rigidity of traditional VF, a dynamic adaptation mechanism was introduced. By inferring operator intent—such as the need to reposition—from Electromyography (EMG) signals, the surgeon can dynamically modulate or disengage the constraint via muscle co-contraction, significantly improving flexibility and safety.

In summary, this thesis delivers a holistic and experimentally validated solution that addresses the entire development chain for advanced pHRI: from the intuitive definition of tasks (LbD + SSA) and the theoretical analysis of safety (Stability and Transparency), to the implementation of specialized (Rehabilitation VF) and adaptive (Surgical VF + EMG) systems. The result is a comprehensive framework that makes collaborative robotics a safe, intuitive, and effective tool for specialists in the clinical domain.

Chapter 1

Introduction

1.1 The Rise of Collaborative Robotics in Complex Domains

The traditional paradigm of robotics, defined by powerful manipulators operating in isolated and caged environments, is undergoing a fundamental transformation. We are entering an era defined by physical, cognitive, and collaborative interaction between humans and machines. This shift, broadly termed Physical Human-Robot Interaction, has been catalyzed by the advent of a new class of manipulators: the collaborative robots. Unlike their industrial predecessors, cobots are designed with inherent safety mechanisms, lightweight structures, and advanced sensing, enabling them to share a workspace and physically cooperate with human users.

This evolution is not merely an industrial trend; it unlocks revolutionary potential in complex, high-stakes domains where human expertise is irreplaceable, but human physical capabilities are a limiting factor. The most prominent of these domains is medicine.

In rehabilitative robotics, cobots offer a solution to the growing demand for intensive, repetitive, and personalised therapy. They can be employed as end-effector devices to guide a patient's limb, replicating Activities of Daily Living (ADL) or providing consistent, data-driven exercises for upper-limb recovery after neurological injuries. The ability to precisely modulate forces and adapt to patient progress makes them powerful tools for therapists.

In robot-assisted surgery, particularly in Minimally Invasive Surgery (MIS), this collaborative paradigm enhances the surgeon's capabilities. Rather than replacing the surgeon, the robot acts as an intelligent, steady hand. It can provide enhanced dexterity, scale motion, filter tremors, and guide instruments with superhuman precision, especially in delicate procedures like Resection and Dis-

section (R&D) that operate near sensitive anatomical structures.

The integration of cobots promises to augment human capabilities across all these domains. However, this potential brings significant new challenges that are universal to all pHRI applications. For any interaction to be effective, the robot cannot simply be a passive, safe tool; the physical collaboration itself must be intelligently structured, guided, and controlled.

1.2 The Research Problem

The bridge from a passive, safe cobot to an effective collaborative partner is built on software-defined guidance. This necessity drives the core problem addressed by this thesis: the need for advanced guidance systems, known as Virtual Fixtures, that are not merely effective, but are also provably safe, intuitive for non-expert users, transparent in their operation, and adaptive to both the operator and the dynamic clinical context.

This dissertation argues that existing solutions fail to adequately address these four interconnected challenges simultaneously:

1. **The Intuition Problem:** How can a non-expert, such as a surgeon or therapist, efficiently and intuitively program a complex robotic task? Learning by Demonstration via Kinesthetic Teaching is a promising solution, but it is fundamentally flawed. When a user demonstrates a task, they impart both geometry and timing. If the user pauses or hesitates randomly during the demonstration, standard time-dependent algorithms encode these pauses as part of the skill. This leads to the *"stagnation phenomenon"*: when the user later interacts with the robot to repeat the task, the controller fails to properly map the applied forces to motion, causing the robot to arbitrarily stall or become unresponsive in those specific locations. Solving this requires fully decoupling the spatial path from the execution time.

2. **The Safety and Transparency Problem:** How can we guarantee that the robot's guidance is stable and feels natural? Admittance control is the dominant paradigm for creating soft, compliant VFs. However, a "stable" controller on paper can become dangerously unstable in practice. Real-world non-idealities—such as actuator saturation, system delays, and joint elasticity—are typically ignored in formal analyses. This gap between theory and reality means that controllers are often tuned conservatively, sac-

rificing performance and transparency (i.e., feeling "heavy" or "sluggish") to avoid undesired oscillations, undermining the very purpose of the cobot.

3. **The Adaptation Problem:** How can a robot adapt when the context changes? A pre-programmed VF, even one that is stable and intuitive, is rigid. In a surgical procedure, tissue may move; in rehabilitation, a patient may fatigue. An operator may need to deviate from the path to handle an unexpected event. A rigid VF that cannot adapt to the user's real-time intent ceases to be an assistant and becomes an obstacle.

4. **The Clinical Translation Problem:** How can generalized control theories be effectively translated into specialized medical applications? Many theoretical frameworks lack validation in realistic scenarios. Bridging the gap between abstract mathematical stability and practical, task-specific implementation—such as handling the unique kinematics of upper-limb rehabilitation or the delicate, discontinuous nature of surgical dissection—remains a critical hurdle for the adoption of collaborative robotics in healthcare.

These gaps reveal the need for a holistic framework that integrates a robust programming-by-demonstration method, a rigorous stability analysis that accounts for real-world dynamics, and an intuitive adaptation mechanism based on user intent, fully validated in realistic clinical scenarios.

1.3 Objective of the Thesis

The primary objective of this thesis is to develop and validate a complete framework for the design and control of advanced VFs for pHRI, enabling non-expert users in the medical field to employ collaborative robots safely, intuitively, and effectively.

To overcome the aforementioned challenges, this research pursues four specific goals:

1. **Robust Task Encoding:** To develop a time-agnostic alignment methodology (SSA) capable of extracting pure geometric constraints from noisy human demonstrations, thereby eliminating temporal artifacts like the stagnation phenomenon.

2. **Stability Under Constraints:** To formally analyze the stability boundaries of admittance-controlled VFs, explicitly incorporating hardware non-idealities to safely maximize transparency.

3. **Intent-Based Adaptation:** To design adaptive architectures that continuously modulate the virtual constraints in real-time by inferring the operator's intent from physiological signals.

4. **Clinical Validation:** To instantiate and validate the developed framework within two highly complex domains: upper-limb rehabilitation and soft-tissue robotic surgery.

1.4 Main Contributions

This dissertation presents several novel contributions to the field of pHRI and robotic control, which are supported by peer-reviewed publications. The main contributions are:

1. **A Comprehensive Survey of Virtual Fixtures.** A systematic review and novel taxonomy of VF research from the last decade, categorized by acquisition, formulation, and implementation methods.

2. **Novel Application of Spatial Alignment for LbD.** The introduction of the SSA as a robust re-parameterization tool for Kinesthetic Teaching. This directly resolves interaction failures caused by human temporal inconsistencies during task demonstration.

3. **A Formal Stability Analysis of Admittance-Controlled VFs.** A rigorous Describing Function analysis that, for the first time, models the combined effects of joint elasticity, system delays, and actuator saturation, directly informing a safe parameter adaptation strategy.

4. **An Optimized Framework for Upper-Limb Rehabilitation.** An end-to-end system featuring a novel workspace optimization method (based on a vertical payload index) and a Hybrid Impedance VF that seamlessly transitions between active and passive therapy modes.

5. **An Adaptive Anisotropic VF Based on User Intent.** A surgical framework featuring an EMG-driven interface (Virtual Clutch). This allows the surgeon to dynamically modulate the constraint geometry via muscle contraction, significantly reducing cognitive workload during complex Resection and Dissection procedures.

1.5 Structure of the Thesis

This dissertation is structured as a unified monograph that logically progresses from the analysis of the state of the art to the methodological foundations, followed by the theoretical control framework, and finally culminating in the experimental validation across two distinct clinical domains.

Chapter 2 provides a comprehensive review of the state of the art in Virtual Fixtures. Based on a systematic survey of the literature, it establishes a rigorous taxonomy for classifying constraints based on their acquisition, formulation, and implementation, highlighting the open challenges that this thesis aims to address.

Chapter 3 details the methodological foundations for intuitive task definition. It introduces the core concepts of Learning by Demonstration (LbD) and presents the Spatial Sampling Algorithm (SSA) as a novel solution for robust trajectory alignment. This chapter demonstrates how decoupling the geometric path from the temporal execution is the necessary prerequisite for stable admittance control.

Chapter 4 addresses the theoretical core of safe interaction. It presents the unified control framework developed in this work, providing formal proofs of passivity and asymptotic stability for the interconnected human-robot system using Lyapunov theory and the framework of dissipative systems.

Chapter 5 bridges the gap between theoretical validity and real-world implementation. It extends the stability analysis to non-ideal operating conditions, investigating the impact of parasitic effects such as time delays, discretization, and actuator saturation. Through sensitivity analysis, it identifies the stability boundaries for variable admittance control.

Chapter 6 presents the first major application of the proposed framework: upper-limb rehabilitation. It details the system's design, introducing a novel workspace optimization method based on a payload index. Furthermore, it validates the Hybrid Impedance Control (HIC) architecture, demonstrating its ability to seamlessly transition between passive and active interaction modes.

Chapter 7 presents the second application: robot-assisted surgery. It focuses on adaptive control based on user intent for Resection and Dissection tasks. Specifically, it details the design of an anisotropic VF and introduces a novel EMG-based interface (Virtual Clutch) that allows the surgeon to dynamically modulate the constraint geometry in real-time.

Chapter 8 concludes the thesis by summarizing the main contributions, discussing the limitations of the current work, and outlining promising directions

for future research in collaborative robotics for healthcare.

Chapter 2

Virtual Fixtures in Human-Robot Interaction

The objective of this chapter is to provide a comprehensive overview of the domain of this thesis: the Virtual Fixture. Starting from the fundamental concepts of physical interaction, it presents a detailed taxonomy of VFs based on recent literature, with a particular focus on the developments occurred between 2015 and 2025 [1]. This chapter analyzes the types of fixtures, the methods for their definition, and the frameworks for their implementation.

2.1 Virtual Fixture Types

A VF is a software-generated constraint or guidance field applied through a robot's control system to assist a human operator [2]. Since their inception, Virtual Fixtures have been investigated to enhance safety, precision, and efficiency in robotic applications [3]. From the perspective of their functional impact on the user, they can be broadly classified into two main categories: Guidance Virtual Fixtures and Forbidden Region Virtual Fixtures [4].

2.1.1 Guidance Virtual Fixture (GVF)

Guidance Virtual Fixtures, also referred to as "assistive virtual fixtures" or "guidance constraints", are designed to actively attract or guide an operator's motion along a desired geometric entity. The primary goal of a GVF is to enhance task accuracy, precision, and efficiency by facilitating the tracking of a specific path or the maintenance of a correct orientation [5].

These fixtures act by "pushing", "pulling", or simply "guiding" the user toward a reference geometry, which can be a point, a curve, or a surface. Prominent examples in literature include:

- **Rehabilitation:** A GVF can be implemented as a "virtual channel" defined by a parametric curve $\varphi(s)$. The system guides the patient's limb along this path, ensuring the exercise is performed correctly while allowing for tracking errors to stimulate motor learning [6], [7].

- **Surgery:** A GVF can define the precise line for a dissection or suturing task, providing selective freedom of movement along the task-relevant direction while constraining undesired motions to protect surrounding tissues [8], [9].

- **Industry:** A GVF can assist in complex assembly tasks, such as "peg-in-hole" operations, by guiding the robot's tool toward the mounting location or maintaining alignment during collaborative transport [10], [11].

Functionally, the assistance provided by a GVF can be rendered in two main ways. It can act *actively*, generating a haptic feedback force that "drags" the user toward the correct position. Conversely, it can act *passively*; in this case, the constraint leaves the user free to perform the task but provides opposing haptic feedback only when a deviation from the reference occurs, effectively acting as a guide rail.

2.1.2 Forbidden Region Virtual Fixture (FRVF)

In contrast to the assistive nature of GVFs, Forbidden Region Virtual Fixture—also known as "restrictive virtual fixtures" or "regional constraints"—are designed to limit motion. Their primary purpose is not to guide a user along a path, but to enhance safety by actively preventing the user from entering predefined unsafe or undesired regions [12].

Functionally, an FRVF acts as a "virtual wall". While GVFs often constrain motion *to* a lower-dimensional manifold (e.g., a curve), FRVFs constrain motion *outside* of a defined geometric entity. Consequently, the constraint itself is typically a volume in 3D space, and the robot is permitted to move anywhere within the workspace except inside this restricted volume.

This approach is critical in safety-critical applications:

- **Surgical Robotics:** An FRVF can be defined from pre-operative anatomical models (e.g., CT or MRI scans) to create a "no-go zone" around sensitive structures like major arteries or nerves. The robot resists any attempt by the surgeon to move the tool into this protected region [13], [14].

- **Industrial Co-manipulation:** FRVFs are employed to prevent the robot from colliding with the human operator or sensitive equipment in a shared workspace [15].

2.2 Interaction Modes and Control Architectures

As introduced in Chapter 1, Physical Human-Robot Interaction describes systems in which a human and a robot interact physically, exchanging forces in a shared workspace [16]. This interaction is generally classified into two main modes, as illustrated in Figure 2.1.

The first mode is **Teleoperation**. In this paradigm, the operator (master) and the robot (slave) are physically separated. The operator imposes a motion on an input device, which is replicated by the robot in a remote environment. Physical interaction occurs through haptic feedback: forces encountered by the robot are transmitted and rendered to the operator, creating a sense of remote "presence" [17], [18].

The second mode is **Co-manipulation**. This represents the limiting case of pHRI where the distance between the operator and the robot is zero. The user is in direct physical contact with the robot, typically by grasping its end-effector to perform a task jointly [19]. In this scenario, the external forces $\boldsymbol{f}_{\text{ext}}$ acting on the robot directly include the force $\boldsymbol{f}_h$ exerted by the human.

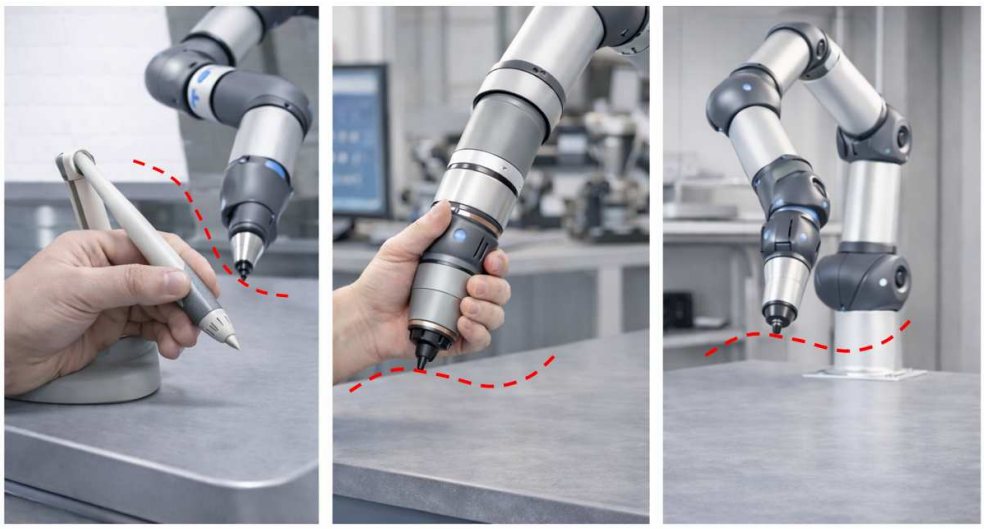

Figure 2.1: Use of VFs in the three main application fields: (a) Teleoperation, (b) Co-manipulation (pHRI), and (c) Autonomous operations.

2.3 Constraint Acquisition and Dimension

The establishment of a VF from its inception can be systematically divided into three different phases, as illustrated in Figure 2.2. This procedure follows a logical progression—moving from left to right—starting from the acquisition of raw geometrical data, moving to the mathematical definition (formulation), and concluding with the physical implementation resulting in the haptic feedback generation.

Before a virtual fixture can be formulated and implemented, its geometric properties must be defined. This process involves two fundamental choices: the acquisition method (i.e., how the constraint data is obtained) and the dimension of the constraint.

2.3.1 Constraint Acquisition

Constraint acquisition refers to the method used to obtain the raw data defining the fixture's geometry. The literature categorizes these methods into three main families [1], [3].

Analytic This approach defines constraints through explicit mathematical expressions. It is computationally efficient and predictable, making it ideal for tasks with clearly defined geometries, such as following a straight line or avoiding spher-

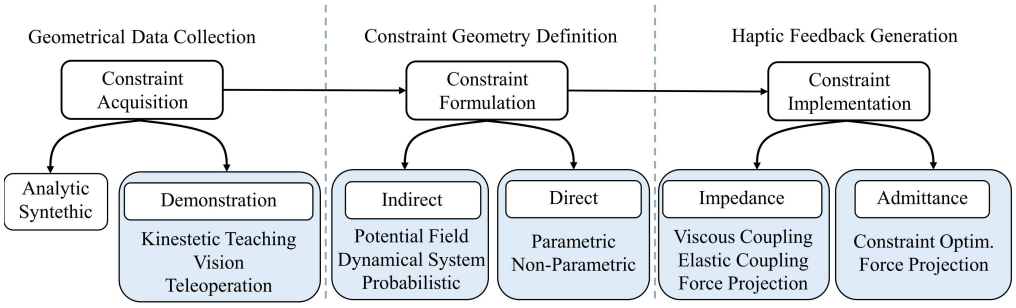

Figure 2.2: The three phases of the virtual fixture establishment: Acquisition, Formulation, and Implementation (adapted from [1]).

ical obstacles [20]. However, its primary disadvantage is limited flexibility, as it is ill-suited for representing complex, irregular shapes or adapting to unstructured environments.

Synthetic This method defines fixtures using pre-computed datasets, such as 3D scans, CAD models, or point clouds. The key advantage is the ability to represent arbitrarily complex geometries, such as organ surfaces or patient-specific anatomy [21]. This is valuable for creating accurate forbidden regions in surgery [13]. The trade-off lies in higher memory consumption and the computational cost required to process discrete data in real-time [22].

Demonstration Also known as Learning by Demonstration, this category involves an expert user "teaching" the constraint to the robot [23]. This human-centric approach is central to this thesis due to its intuitiveness. Depending on the interaction interface, this approach can be subdivided into:

- **Kinesthetic Teaching (KT):** The operator directly grasps and physically guides the robot's end-effector or structure to demonstrate the desired motion. The robot, typically under gravity compensation, records its own poses to learn the path. This method allows the user to intuitively feel the robot's actual physical workspace and kinematic limits, making it widely used in rehabilitation and industrial co-manipulation [24], [25].
- **Vision:** A non-contact method where cameras or depth sensors track a target to define geometry. It enables real-time acquisition in dynamic environments [26], [27].
- **Teleoperation:** While conceptually analogous to KT as a form of human demonstration, the foundational literature on Learning by Demonstration

[28] formally differentiates teleoperation due to its master-slave architecture. The expert performs the task via a physically decoupled master input device (e.g., a haptic console), and the constraint is recorded from the remote slave robot's motion [29], [30]. Unlike KT, this physical decoupling allows for motion scaling and completely hides the inertia of the slave robot from the user, making it the standard approach for acquiring demonstrations in MIS where direct manipulation of the robotic arms is unfeasible.

2.3.2 Constraint Dimension

Position Constraints The most common constraints apply to the robot's 3D position:

- **0D (Point):** Used as an attractive GVF to guide the user to a specific target [31].
- **1D (Curve):** A curve $\varphi(s)$, extensively used in path-following tasks for rehabilitation and dissection [32].
- **2D (Surface):** Used to guide a tool across a surface without penetrating it [33].
- **3D (Volume):** The default for FRVFs, or as a "virtual channel" GVF [8].

Orientation Constraints In addition to position, VFs can also constrain the rotational degrees of freedom (DoF). In some basic MIS applications, orientation constraints are partially implicit due to the Remote Center of Motion (RCM), which limits the tool shaft's rotation around the insertion point [34], [35]. However, modern robot-assisted laparoscopy heavily relies on wristed instruments, which introduce additional intra-corporeal rotational DoFs that are entirely independent of the RCM. Furthermore, specific surgical tasks—such as bone surface abrasion using orthopedic robots (e.g., the Stryker MAKO system)—require the end-effector (the milling machine) to maintain a precise orientation relative to the target anatomy to ensure safe and effective cutting. In these advanced scenarios, the RCM is insufficient, and explicit orientation VFs become strictly necessary.

When orientation constraints are explicitly implemented, the central challenge becomes the mathematical representation of the orientation misalignment $\boldsymbol{e}_o \in \mathbb{R}^3$. The literature highlights diverse approaches to define this error:

However, when orientation constraints are explicitly implemented, the central challenge becomes the mathematical representation of the orientation misalignment $\boldsymbol{e}_o \in \mathbb{R}^3$. The literature highlights diverse approaches to define this error:

- **Unit Quaternions:** This method is widely adopted for its robustness against singularities. The misalignment $\boldsymbol{e}_o$ is typically obtained by extracting the vector part from the quaternion product:

$$\boldsymbol{e}_o = \text{vec}(\boldsymbol{\Delta}_q), \quad \text{where} \quad \boldsymbol{\Delta}_q = \boldsymbol{q}_d \otimes \boldsymbol{q}, \tag{2.1}$$

  where $\boldsymbol{q}_d$ and $\boldsymbol{q}$ represent the desired and actual orientations [36], [37].

- **Rotation Matrices:** The misalignment is initially represented by the matrix error $\boldsymbol{E}_O = \boldsymbol{R}_d^T \boldsymbol{R}$. To obtain the vector $\boldsymbol{e}_o$, two main strategies are used:

  1. The *Matrix Logarithm*, where $\boldsymbol{E}_{o_w} = \log(\boldsymbol{R}_d^T \boldsymbol{R})$ is mapped to $\mathbb{R}^3$ via the 'vee' operator ($\boldsymbol{e}_o = \text{vee}(\boldsymbol{E}_{o_w})$) [38].
  2. A *Linear Approximation* for small displacements, defined as the skew-symmetric part $\tilde{\boldsymbol{E}}_{O_w} = \frac{1}{2}(\boldsymbol{R}_d^T \boldsymbol{R} - \boldsymbol{R}^T \boldsymbol{R}_d)$ [24].

- **Axis/Angle:** The error is derived from the equivalent rotation angle θ about a unit axis $\hat{\boldsymbol{u}}$, resulting in the Euler vector $\boldsymbol{e}_o = \theta \hat{\boldsymbol{u}}$ [39], [40].

- **Vector Product:** Often used for aligning a tool axis $\hat{\boldsymbol{z}}$ with a target axis $\hat{\boldsymbol{z}}_0$, the error is derived from the misalignment angle $\zeta = \arccos(\hat{\boldsymbol{z}}^T \cdot \hat{\boldsymbol{z}}_0)$, enforcing conditions such as $\zeta < \zeta_{max}$ [41].

- **Euler Angles:** The error is expressed as the difference in a 3-element vector (e.g., Roll-Pitch-Yaw or XYZ conventions). While this representation famously suffers from gimbal lock singularities [42], [43], it remains present in the literature due to its unparalleled physical intuitiveness. Specifically, Euler angles allow for the trivial decoupling of individual rotational DoFs. For instance, in surgical drilling or screwing tasks, it is often necessary to strictly constrain the pitch and yaw of the tool while leaving the roll axis completely free. This independent, axis-specific modulation is straightforward to implement using Euler angles, whereas it requires complex mathematical decoupling when using unit quaternions or rotation matrices. Consequently, Euler angles are still employed in specific applications where the workspace is bounded and guaranteed to remain far from singular configurations.

2.4 Constraint Formulation

The term constraint formulation refers to the manner in which the reference geometry is defined, thereby specifying the spatial regions in which the robot is allowed or forbidden to move. The formulation can be broadly categorized into **Direct** (parametric or non-parametric) and **Indirect** (based on induction mechanisms like potential fields).

2.4.1 Indirect Formulation

In an indirect formulation, the constraint geometry is implicitly defined by a field or a set of dynamics.

Potential Field (PF) Originating from the seminal work of Khatib [44], this method defines the constraint geometry implicitly through a scalar potential function $\phi(\boldsymbol{x})$ defined over the robot's workspace, or in a suitable subspace of it [45], [46]. In this context, the state vector $\boldsymbol{x}$ denotes the configuration in the considered task space, which typically refers to the Cartesian position but may effectively include orientation coordinates depending on the task requirements.

As illustrated in Figure 2.3, the environment is mapped such that obstacles are modeled as high-potential "hills" (repulsive regions), while targets or desired paths are modeled as low-potential "valleys" (attractive regions) [47]. Depending on the chosen control implementation strategy (impedance or admittance), two main formulations can be distinguished:

$$\boldsymbol{f}_{VF} = \pm\nabla\phi(\boldsymbol{x}), \tag{2.2a}$$

$$\boldsymbol{x}_{VF} = \arg\min_{\boldsymbol{x}}(\phi(\boldsymbol{x})). \tag{2.2b}$$

The formulation in (2.2a) is adopted whenever an *impedance* implementation is used. Here, ∇ is the gradient of the potential field, and the sign $\pm$ determines whether the generated force $\boldsymbol{f}_{VF}$ acts as a repulsive (minus) or attractive (plus) field to constrain the user's motion. Conversely, the formulation in (2.2b) is adopted for *admittance* implementations. In this case, the desired reference path $\boldsymbol{x}_{VF}$ is generated by navigating through the regions of the workspace associated with the minima of the potential field $\phi(\boldsymbol{x})$.

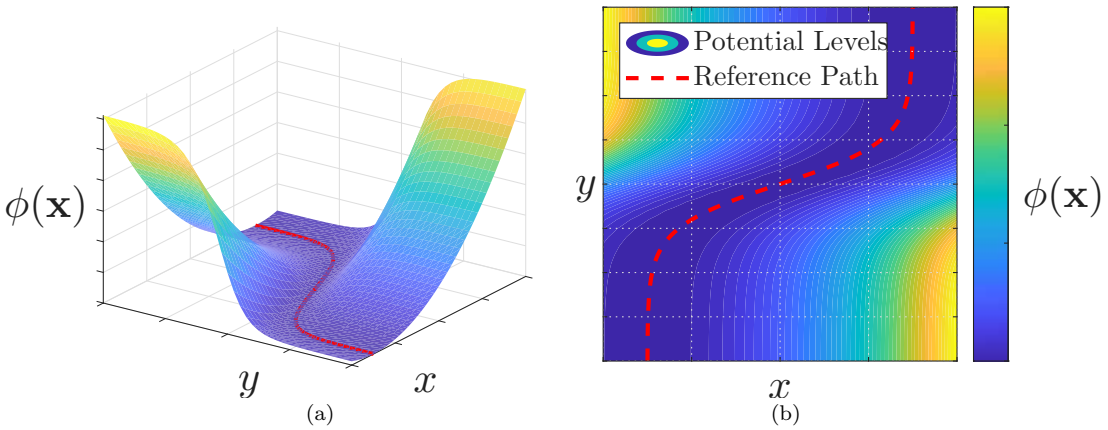

Figure 2.3: Example of potential field $\phi(\boldsymbol{x})$ (a) and the corresponding level curves (b) for a two-dimensional task.

Dynamical System (DS) In this framework, the constraint guiding the user is encoded through non-linear dynamics [48], [49], typically formulated as:

$$\dot{\boldsymbol{\zeta}}_{VF} = \boldsymbol{f}_{ds}(\boldsymbol{\zeta}_{VF}, \boldsymbol{u}), \tag{2.3}$$

where the definition of the state vector $\boldsymbol{\zeta}_{VF}$ depends on the system order: it corresponds to the position $\boldsymbol{x}_{VF}$ in a first-order system, or to the full state vector $[\,\boldsymbol{x}_{VF}^T, \dot{\boldsymbol{x}}_{VF}^T\,]^T$ in a second-order system. The input signal $\boldsymbol{u}$ allows incorporating external factors, most notably the force applied by the user during the interaction.

A prominent class within this category is represented by Dynamic Movement Primitives [50], [51]. DMPs model the task as a stable linear attractor (e.g., a mass-spring-damper system) augmented with a non-linear forcing term learned from demonstration. This approach guarantees smooth, convergent trajectories and has been widely extended to virtual fixture frameworks in various domains, including rehabilitation [6], [52], human–robot handovers [53], [54], and manufacturing tasks [55].

Probabilistic and Learning Approaches These methods infer the constraint geometry directly from data, exploiting multiple demonstrations to build a probability distribution $p(\boldsymbol{x})$ defined over the robot's task space or a suitable subspace [56], [57]. This allows capturing both the task structure and its inherent variability.

In close analogy to the potential field formulations presented in (2.2), probabilistic virtual fixtures can be expressed through dual formulations depending on

the control causality:

$$\boldsymbol{f}_{VF} = \pm\nabla p(\boldsymbol{x}), \qquad \boldsymbol{x}_{VF} = \arg\max_{\boldsymbol{x}}(p(\boldsymbol{x})). \tag{2.4}$$

The left-hand formulation corresponds to the probabilistic analogue of the *impedance*-based potential field, where the gradient of the distribution induces a virtual force field. Here, the sign determines the interaction nature: a positive gradient generates an attractive field guiding the user toward high-probability regions, whereas a negative gradient creates a repulsive effect. The right-hand formulation mirrors the *admittance*-based approach, where the desired reference $\boldsymbol{x}_{VF}$ is obtained by extracting the most probable path, i.e., navigating through the maxima of the distribution $p(\boldsymbol{x})$ [58], [59].

While the most widespread probabilistic implementations rely on Gaussian Mixture Model (GMM)s, this category conceptually extends to Learning approaches, such as Reinforcement Learning (RL). In RL contexts, the probability distribution function $p(\cdot)$ is replaced by a reward function $r(\cdot)$ to shape the robot's compliance and guidance behavior.

2.4.2 Direct Formulation

In a direct formulation, the constraint geometry is explicitly defined by a mathematical relationship involving the robot's configuration. Based on the presence of auxiliary variables, this category is divided into parametric and non-parametric approaches.

To illustrate, consider a planar task where the end-effector is constrained to a circular path of radius R centered at (x_c, z_c) in the xz-plane. In a parametric formulation, the constraint introduces an auxiliary angle s to define the allowed coordinates:

$$\mathbf{h}_p(\mathbf{q}, s) = \begin{bmatrix} x - (x_c + R\cos s) \\ z - (z_c + R\sin s) \end{bmatrix} = \mathbf{0}. \tag{2.5}$$

This approach is particularly powerful for defining complex curves. In this thesis, *Parametric B-Splines* are adopted due to their compactness and C^2 continuity [60]. Crucially, this formulation allows for arc-length parameterization, which is essential to ensure smoothness in admittance control and to handle task singularities [32].

Non-Parametric Formulation Conversely, a constraint is *direct-non parametric* if it is defined by a function $h_{np}(\mathbf{q}) = 0$ that relies *exclusively* on the

configuration variables, without any external parameter [61]:

$$h_{np}(\mathbf{q}) = 0. \tag{2.6}$$

Applying this to the previous example of the circular path, the geometry is defined implicitly:

$$h_{np}(\mathbf{q}) = (x - x_c)^2 + (y - y_c)^2 - r^2 = 0. \tag{2.7}$$

While analytically elegant for simple geometric primitives, in complex unstructured environments this formulation typically relies on discrete data such as point clouds or meshes. Although flexible for representing arbitrary shapes [13], real-time interaction in this domain is often computationally demanding, requiring expensive algorithms to compute the distance to the nearest constraint point [22].

2.5 Constraint Compliance

This aspect determines the "feel" of the fixture. As shown in Figure 2.4, different combinations of constraint dimensions and stiffness levels may yield similar behaviors.

Hard Constraints These define an impenetrable boundary. They are essential for FRVFs in safety-critical tasks [4], preventing tool penetration into sensitive volumes (Fig. 2.4(c)) or strictly confining motion to a "hard" channel (Fig. 2.4(a)). It is important to clearly distinguish the implementation of hard VFs from the related field of collision detection and haptic rendering, which is extensively studied in telepresence and virtual reality environments. While advanced haptic rendering focuses on efficiently computing exact contact points and simulating realistic reaction forces between highly complex, high-resolution 3D polygonal meshes (e.g., a robotic tool interacting with arbitrary environmental obstacles), VFs generally rely on mathematically concise analytical or parametric boundaries. Their primary objective is not the high-fidelity physical simulation of environmental contacts, but rather the proactive and robust shaping of the user's control input to enforce safe, ergonomic, and stable task execution.

Soft Constraints Soft constraints (Fig. 2.4(b)) allow deviations from the reference, applying a restoring force proportional to the error (e.g., a virtual spring).

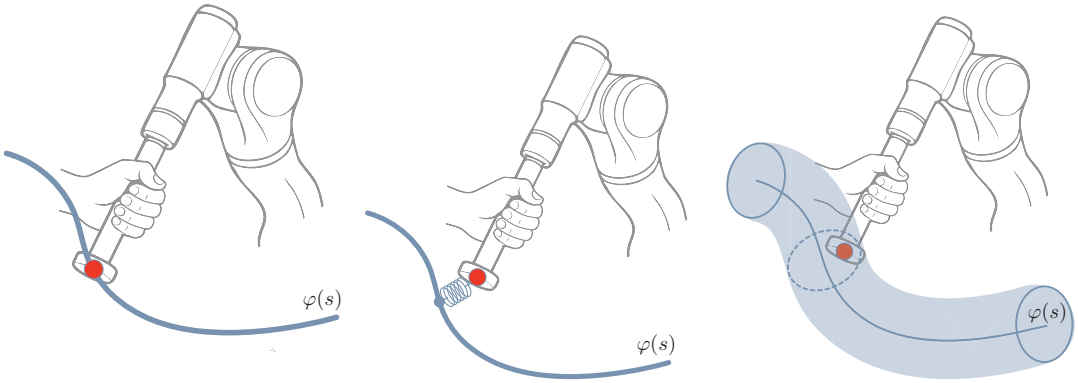

(a) (b) (c)

Figure 2.4: Examples of positional constraints. (a) Hard type constraint geometry of dimension curve, (b) Soft type constraint geometry of dimension curve, (c) Hard type constraint geometry of dimension volume.

This is typical for guidance, enabling assist-as-needed (AAN) paradigms where the user is gently guided but not rigidly locked to a path [62].

2.6 Constraint Implementation

The implementation defines the control law that renders the formulated constraint. As illustrated in Figure 2.5, two main paradigms exist with opposite causalities.

2.6.1 Impedance-based Implementations

Following the causality *motion commands force*, the VF generates a force $\boldsymbol{f}_{VF}$ based on kinematic error [17]. This Cartesian restoring force is then mapped into the joint space via the Jacobian transpose ($\boldsymbol{J}^T(\boldsymbol{q})$) to compute the reference joint torques, which are subsequently tracked by the robot's low-level Torque Controller.

- **Viscous Coupling:** Generates a damping force $\boldsymbol{f}_{VF} = \boldsymbol{f}_v(\dot{x})$ to resist motion in restricted directions.
- **Elastic Coupling:** Uses a virtual spring-damper $\boldsymbol{f}_{VF} = \boldsymbol{f}_{el}(\tilde{\boldsymbol{x}}) + \boldsymbol{f}_v(\dot{\tilde{\boldsymbol{x}}})$. It is the most common method for creating both soft guidance and repulsive fields [63].
- **Force Projection/Filtering:** Calculates the exact force required to cancel user input violating a constraint. This is often formalized using Lagrange multipliers $\boldsymbol{\lambda}$ and $\boldsymbol{\mu}$ associated with bilateral and unilateral constraints [43]:

$$\boldsymbol{f}_{VF} = \boldsymbol{A}(\boldsymbol{q})^\top \boldsymbol{\lambda} + \boldsymbol{C}(\boldsymbol{q})^\top \boldsymbol{\mu}, \tag{2.8}$$

  where $\boldsymbol{A}(\boldsymbol{q})$ and $\boldsymbol{C}(\boldsymbol{q})$ describe the geometric constraints. This force can be applied directly (hard constraint) or incorporated into an admittance model dynamics.

2.6.2 Admittance-based Implementations

Following the causality *force commands motion*, the VF modifies the motion reference based on input forces. The resulting Cartesian reference variables (typically position $\boldsymbol{x}_{\text{VF}}$ and velocity $\dot{\boldsymbol{x}}_{\text{VF}}$) are subsequently mapped into the joint space using Inverse Kinematics (IK) algorithms, providing the reference setpoints $(q_d, \dot{q}_d)$ for the robot's low-level Position/Velocity Controller.

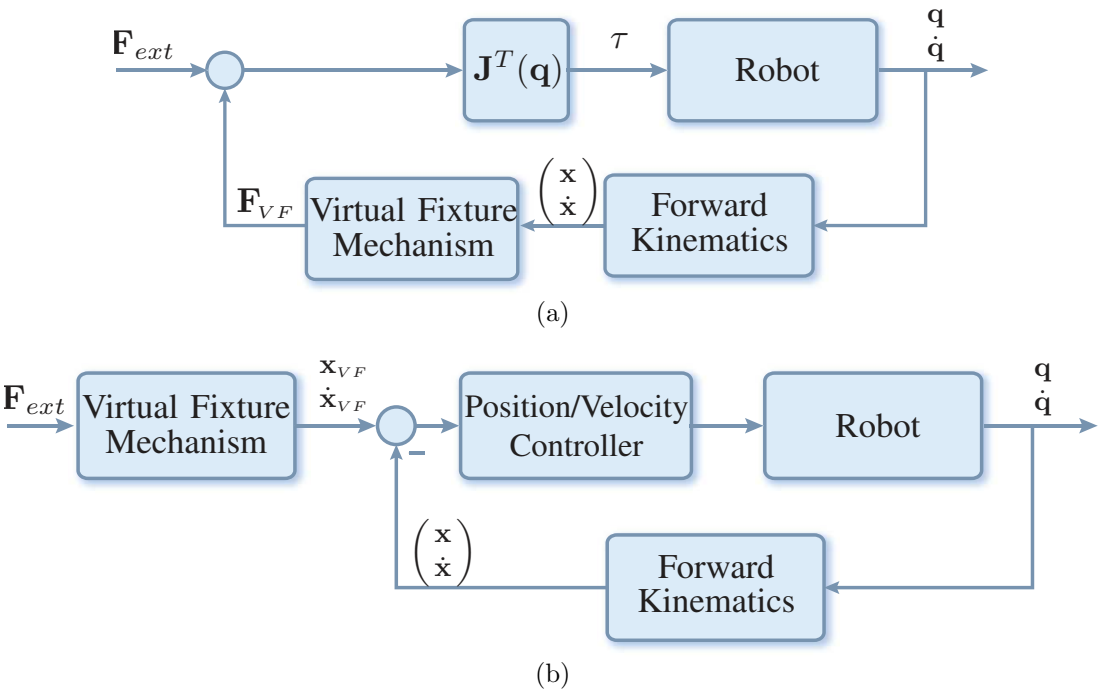

Figure 2.5: Block-diagram representation of virtual fixtures with opposite causalities: impedance type (a) and admittance type (b).

Constrained Optimization The kinematic reference $\boldsymbol{\zeta}_{\text{VF}}$ is obtained by solving an optimization problem to find the admissible motion closest to the user's intent (reference $\boldsymbol{\zeta}_{\text{ref}}$) while respecting constraints:

$$\boldsymbol{\zeta}_{\text{VF}} = \arg\min_{\boldsymbol{\zeta}} H(\boldsymbol{\zeta}_{\text{ref}}, \boldsymbol{\zeta}) \quad \text{s.t.} \quad \boldsymbol{\zeta} \in \mathcal{S}_{\boldsymbol{\zeta}}. \tag{2.9}$$

Here, $H(\cdot,\cdot)$ represents a cost function penalizing the deviation from the user's intended motion, and $\mathcal{S}_{\boldsymbol{\zeta}}$ denotes the feasible set of all admissible kinematic states defined by the VF geometry (e.g., the collision-free space for a forbidden region, or the bounded corridor for a guidance channel). This approach is powerful for enforcing complex constraints (e.g., from anatomical meshes) [21].

Force Projection / Filtering The reference velocity $\dot{\boldsymbol{x}}_{VF}$ is obtained from the external force $\boldsymbol{f}_{ext}$ through a direction-dependent mapping. A widely used linear relationship is [64]:

$$\dot{\boldsymbol{x}}_{VF} = c\left([\mathbf{D}] + \mathbf{W}\,\langle\mathbf{D}\rangle\right)\boldsymbol{f}_{ext}, \tag{2.10}$$

where $[\mathbf{D}]$ projects onto preferred directions (tangential), $\langle\mathbf{D}\rangle$ projects onto forbidden directions (orthogonal), and $\mathbf{W}$ is a weighting matrix that scales down the

response in restricted directions. It is crucial to note that this direct projection method is highly efficient for geometric primitives or analytically defined parametric curves, where the tangent and normal vectors required to populate the projection matrices can be explicitly computed in real-time. However, applying this exact formulation to arbitrary, highly complex geometries (such as high-resolution anatomical meshes) is not trivial. In such unstructured environments, the continuous evaluation of the local contact normal $\langle \mathbf{D} \rangle$ requires the integration of sophisticated collision detection and haptic rendering algorithms—such as distance fields queries or God-Object heuristics developed for advanced telepresence [65], [66]—to computationally bridge the gap between arbitrary polygonal meshes and the directional admittance mapping.

Dynamic Proxy The external force drives a virtual "proxy" mass constrained to the geometry. This can be combined with the filtering approach to define the proxy's dynamics:

$$\mathbf{M}\ddot{\boldsymbol{x}}_{VF} + \mathbf{B}\dot{\boldsymbol{x}}_{VF} = \mathbf{C}\left([\mathbf{D}] + \mathbf{W}\left\langle \mathbf{D} \right\rangle\right)\boldsymbol{f}_{ext}. \tag{2.11}$$

This formulation allows for fine control of the robot's dynamic behavior, which is particularly effective in HRI for shaping user actions [37]. Crucially, this dynamic proxy paradigm constitutes the foundational control core of the present thesis. As will be detailed in the subsequent chapters (specifically from Chapter 4 onwards), the control architectures developed in this work employ an admittance-based virtual mass constrained to an arc-length parameterized path. This specific choice allows the system to seamlessly decouple the geometric guidance from the temporal execution speed, ensuring stable and intuitive co-manipulation in both rehabilitative and surgical scenarios.

2.7 Case Studies: Virtual Fixtures in Rehabilitation and Surgery

The theoretical framework presented in this chapter finds concrete application in the two domains addressed by this thesis: upper-limb rehabilitation and robot-assisted surgery. This focus is not arbitrary but reflects the dominant trends in recent research. As illustrated in Figure 2.6, approximately 50% of the contributions in the field of virtual fixtures over the last decade are concentrated in the medical domain, encompassing surgery, rehabilitation, and training [1].

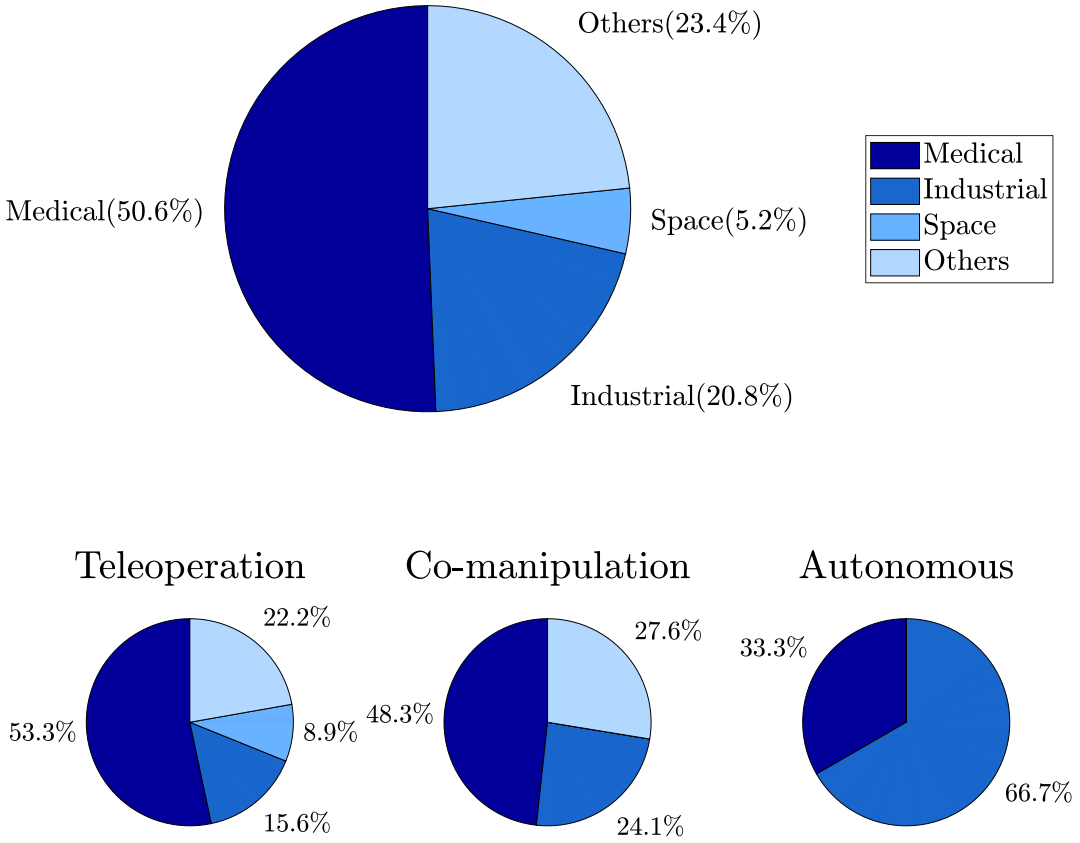

Figure 2.6: Percentage distribution of VFs applications (adapted from [1]). The medical field represents the majority of research efforts, particularly within Teleoperation and Co-manipulation domains.

Furthermore, the breakdown by interaction mode (Figure 2.6, bottom) reveals that medical applications are the primary driver for advancements in both Teleoperation and Co-manipulation. Figure 2.7 further contextualizes this by summarizing the technical trends: while Teleoperation often relies on soft, impedance-based methods for guidance, Co-manipulation increasingly favors admittance-based transparency to promote safe and ergonomic collaboration. This preference for admittance control in physical co-manipulation stems from its ability to mask the actual mechanical dynamics of the manipulator. In a pure impedance scheme, the human operator physically interacts with the robot's inherent mass and joint friction, which can be fatiguing, especially with industrial-grade collaborative robots. Conversely, an admittance scheme senses the user's force $\boldsymbol{f}_{ext}$

Figure 2.7: Summary of research trends in robotic VFs (2014–2025) categorized by acquisition, formulation, and implementation methods. Dark blue histograms represent impedance-implemented VFs, while light blue histograms represent admittance-implemented VFs (adapted from [1]).

and feeds it into a virtual dynamic model (e.g., the dynamic proxy). The robot is then position-controlled to track this ideal model. By setting low virtual mass and damping parameters in the software, the controller actively assists the motion, making even a heavy robot feel completely "transparent" and weightless to the user.

The case studies developed in this thesis are strategically positioned at the intersection of these highly relevant domains, introducing an innovative hybrid approach that bridges the gap between rigid guidance and adaptive human-robot interaction.

2.7.1 Rehabilitative Robotics

In the context of upper-limb rehabilitation (detailed in Chapter 6), the primary clinical goal is to provide assist-as-needed (AAN) therapy [67]. To achieve this, the proposed system diverges from standard uniform controllers by employing a novel *Hybrid Impedance-Admittance Control* architecture. This specific choice is motivated by the need to spatially decouple the task progression from the spatial confinement:

- **Type:** GVF designed as an anisotropic "virtual channel".
- **Acquisition:** KT is used to capture expert therapist motions. These demonstrations are subsequently re-parameterized via arc-length (SSA) to

completely decouple the geometric path from the original temporal variability [32].

- **Implementation:** A spatially decoupled Hybrid Control is adopted. The task progression (motion *along* the reference path) is governed by an **Admittance** model: the user's applied tangential forces dictate the execution speed, allowing the patient to organically set the pace of the exercise. Conversely, the spatial confinement (deviations *orthogonal* to the path) is managed by an **Impedance** controller featuring a non-linear compliance. This hybrid design leaves a "soft" center—allowing small tracking errors essential to stimulate patient motor learning—while providing rigid, reactive haptic feedback at the channel boundaries to strictly enforce safety.

2.7.2 Surgical Robotics

In the surgical domain (Chapter 7), the focus is on precision during R&D tasks. This reflects the teleoperation trend where haptic feedback is critical for accuracy:

- **Type:** GVF constraining motion to a specific line or plane relevant to the procedure.
- **Implementation:** Adaptive Impedance with Dynamic Proxy. The constraint stiffness is anisotropic [8] and, crucially, adaptive based on the surgeon's EMG signals [68]. This addresses the static rigidity limitation common in literature, allowing seamless transitions between stiff guidance for precision and free motion for gross positioning.

Chapter 3

Methodological Foundations for Intuitive Task Definition

This chapter details the methodological foundations for intuitive task definition adopted in this thesis. It introduces the core concepts of Learning by Demonstration (LbD) and presents the Spatial Sampling Algorithm (SSA) as a novel solution for robust trajectory alignment.

Since all the control architectures and experimental applications presented in the subsequent chapters rely on a specific geometric encoding of the task, this chapter provides the rigorous derivation of the spatial parameterization. Specifically, it demonstrates how the SSA outperforms traditional temporal alignment methods (such as Dynamic Time Warping (DTW)) and how it serves as the necessary prerequisite for defining stable virtual constraints in admittance control.

3.1 The Alignment Problem in Learning by Demonstration

Learning by Demonstration aims to transfer skills to robots by leveraging multiple demonstrations of the same task [69]. A fundamental step in LbD is extracting a consistent "skill" (often a mean trajectory and a stiffness profile) from a set of noisy human demonstrations [58], [70].

However, human demonstrations are inherently inconsistent in the temporal domain. Even when performing the exact same geometric path, a user will introduce local speed variations and pauses.

- **Temporal Distortion:** Simply averaging trajectories based on time timestamps (t) leads to geometric distortion, as points that are temporally coincident may be spatially distant [71].

- **Traditional Solution (DTW):** The standard approach in literature is Dynamic Time Warping (DTW), which warps the time axis to minimize the distance between signals [72], [73]. While effective for signal classification, DTW has limitations in robotics: it requires selecting a "reference" trajectory (which biases the result) and does not fully decouple the geometric path from the temporal evolution [74], [75].

3.2 The Spatial Sampling Algorithm (SSA)

To address these limitations, this thesis proposes the Spatial Sampling Algorithm (SSA). This algorithm is not merely a filtering technique but a re-parameterization method that transforms time-dependent trajectories $\boldsymbol{y}(t)$ into regular, arc-length parameterized curves $\hat{\boldsymbol{y}}(s)$. This encoding forms the basis for all virtual constraints defined in this work [32], [71].

3.2.1 Algorithm Derivation

The SSA operates by resampling the trajectory based on Euclidean distance rather than time intervals. The procedure is mathematically defined as follows:

1. **Continuous Interpolation:** Given a discrete sequence of recorded points $\boldsymbol{y}_{T,i} = \boldsymbol{y}(iT)$, we first construct a linearly interpolating continuous function $\boldsymbol{y}_L(t)$.

2. **Spatial Constraint:** We generate a new sequence of points $\hat{\boldsymbol{y}}_k$ such that the Euclidean distance between consecutive samples is strictly constant and equal to a 3design parameter δ:

$$||\hat{\boldsymbol{y}}_k - \hat{\boldsymbol{y}}_{k-1}|| = \delta, \quad \forall k = 1, \ldots, m \tag{3.1}$$

3. **Arc-Length Mapping:** This process implicitly defines a mapping from time to arc-length. The spatial samples correspond to specific time instants t_k such that $\hat{\boldsymbol{y}}_k = \boldsymbol{y}_L(t_k)$. The arc-length parameter is then defined discretely as $s_k = k\delta$ [71].

3.2.2 Geometric Properties

The crucial property derived from this algorithm is the regularization of the curve's tangent. Once the SSA has filtered and resampled the raw data to gen-

erate the discrete, arc-length parameterized sequence $\hat{\boldsymbol{y}}_k$, an analytic continuous representation is required for the control implementation. Specifically, by interpolating these spatially equidistant points via smoothing B-Splines over the parameter s, we obtain a continuous, twice-differentiable ($\mathcal{C}^2$) curve $\boldsymbol{\varphi}(s)$. Thanks to the spatial regularization provided by the SSA pre-processing, the derivative of this analytic function with respect to s is approximately unitary [32]:

$$\left.\frac{d\boldsymbol{\varphi}(s)}{ds}\right|_{s=s_k} \approx \frac{||\hat{\boldsymbol{y}}_{k+1} - \hat{\boldsymbol{y}}_k||}{||s_{k+1} - s_k||} = \frac{\delta}{\delta} = 1 \tag{3.2}$$

This property, $\|\boldsymbol{\varphi}'(s)\| \approx 1$, is the cornerstone of the control stability in the proposed framework, as it ensures the virtual constraint is well-defined regardless of the demonstration speed.

3.3 Comparative Validation of Trajectory Alignment

To validate the SSA as a superior encoding method for skill extraction, we compared it against standard state-of-the-art approaches. The objective was to compute the barycenter (the "skill") from a dataset of multiple noisy demonstrations.

3.3.1 Comparison Setup

Three alignment and encoding pipelines were tested on the same dataset of human-demonstrated trajectories [71]:

1. **TIME/GMR:** Raw trajectories aligned by time indices, fed directly into Gaussian Mixture Regression (GMR) [58].
2. **DTW/GMR:** Trajectories aligned using Dynamic Time Warping before GMR processing (State of the Art) [75], [76].
3. **SSA/GMR (Proposed):** Trajectories spatially sampled via SSA before GMR processing.

3.3.2 Results and Discussion

The quality of the extracted skill was evaluated using the Hausdorff distance (d_H) and DTW distance (d_{DTW}) as metrics of geometric consistency.

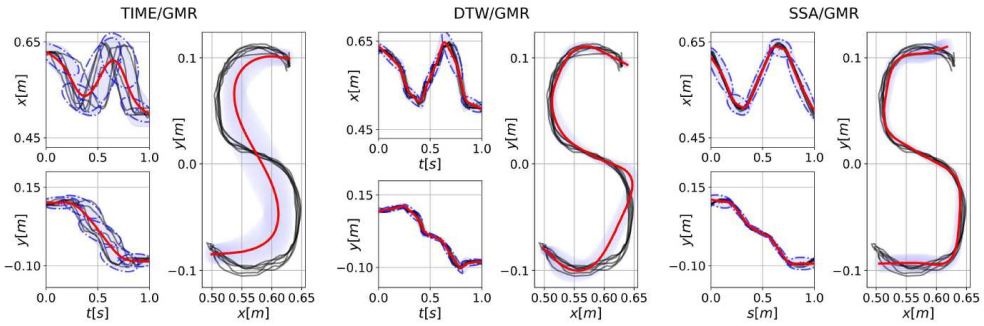

Figure 3.1: Comparison of barycenter computation using Time/GMR, DTW/GMR, and SSA/GMR.

- **Variance Reduction:** As shown in the experimental analysis (refer to Fig. 3.1), Time/GMR results in high variance due to temporal misalignments. The proposed SSA/GMR approach significantly reduces this variance, producing a tighter "tube" around the desired path compared to both Time and DTW methods.

- **Reference Independence:** A major flaw of DTW is its dependence on a reference trajectory for alignment, which can distort the resulting barycenter shape [74]. The SSA, being an intrinsic re-parameterization, does not require a reference, yielding a more natural and faithful representation of the demonstrated geometry.

- **Quantitative Performance:** The SSA/GMR method outperformed the others in both metrics. Specifically, it achieved the lowest approximation error (e.g., $d_{DTW} \approx 0.8 \pm 0.12$ for SSA vs 2.4 ± 0.22 for DTW), confirming its ability to filter out temporal noise while preserving the geometric intent [71].

- **Limitations and Design Trade-offs:** Despite its geometric superiority, the proposed pipeline introduces specific trade-offs, particularly regarding the choice of B-Splines for continuous approximation. While smoothing B-Splines excel at guaranteeing $\mathcal{C}^2$ continuity (crucial for control stability), they inherently struggle with high-frequency spatial features, such as sharp corners or abrupt directional changes. If the smoothing parameter (λ) or the error tolerance is not carefully tuned, the algorithm may over-smooth these critical geometric details, treating intentional sharp turns as human tremor. Consequently, while this representation is highly effective for the fluid motions typical of upper-limb rehabilitation and macroscopic

surgical paths, alternative regression techniques might be required for tasks demanding pixel-perfect retention of sharp geometrical discontinuities.

3.4 Foundation for Virtual Constraint Definition

The primary reason for adopting the SSA in this thesis is not merely for data analysis, but to enable a robust *human-in-the-loop* control architecture. All subsequent experimental chapters utilize the SSA-encoded trajectory $\varphi(s)$ to define the virtual constraints.

3.4.1 Solving the Stagnation Phenomenon

In kinesthetic teaching, users often pause or hesitate. If the virtual constraint is parameterized by a time-based variable $p(t)$, these pauses create "dead zones" where the derivative $\frac{d\varphi}{dp} \to 0$. This leads to the "Stagnation Phenomenon", where the robot becomes unresponsive to user forces because the mapping from force to motion vanishes [77].

By using the SSA, we decouple the execution flow from the demonstration time. Since $\varphi'(s) \approx 1$ (Eq. 3.2), the tangent vector is always non-zero. This guarantees that the system never stagnates, even if the original demonstration contained stops [71].

3.4.2 Dynamic Proxy Formulation

The SSA encoding allows us to define the dynamics of the interaction using a virtual proxy governed by Lagrange's equations on the arc-length coordinate s. The fundamental control law used throughout this thesis is [78]:

$$m\ddot{s} + b\dot{s} = f_{||} \tag{3.3}$$

where:

- m and b are the virtual mass and damping of the proxy.
- $f_{||} = \varphi'(s)^T \cdot \hat{\boldsymbol{f}}_{\boldsymbol{h}}$ is the projection of the user's applied force measured at the end effector $\hat{\boldsymbol{f}}_{\boldsymbol{h}}$ onto the path tangent.

This formulation implies that the user's force directly controls the *progression* along the task (s), while the robot's controller ensures the *precision* of the path

$\varphi(s)$. This architecture, enabled strictly by the properties of the SSA, allows for intuitive guidance where the user decides the speed and the robot guarantees the geometry [77], [78].

3.4.3 Extension to Orientational Trajectories and Constraints in $SE(3)$

While the derivation of the SSA and the proxy dynamics presented above focuses on translational paths in $\mathbb{R}^3$, realistic physical human-robot interaction often requires full 6-DoF guidance in $SE(3)$. The proposed methodological framework natively supports the extension to orientational virtual fixtures without losing the benefits of the spatial re-parameterization. During the LbD phase, alongside the Cartesian positions $\boldsymbol{y}_i$, the user's demonstrations provide a sequence of end-effector orientations. To avoid representation singularities (e.g., gimbal lock), these are encoded as unit quaternions $\mathbf{q}_i = \{\eta_i, \boldsymbol{\epsilon}_i\}$. Crucially, the arc-length parameter s extracted from the translational path via the SSA acts as the master phase variable for the entire task. The desired orientation profile is thus parameterized as a function of this spatial coordinate, yielding $\mathbf{q}_d(s)$. The continuous rotational trajectory is generated by applying Spherical Linear Interpolation (Slerp) between the spatially sampled key-poses. At runtime, the dynamic proxy formulation (5.1) computes the progression $s(t)$ based on the user's translational forces. This $s(t)$ simultaneously defines the reference position $\varphi(s(t))$ and the reference orientation $\mathbf{q}_d(s(t))$. To enforce the orientational constraint, an impedance-based restoring torque $\boldsymbol{\tau}_{ve}$ is computed. Let $\mathbf{q} = \{\eta, \boldsymbol{\epsilon}\}$ be the actual end-effector orientation. The orientation error is calculated via the quaternion product $\mathbf{q}_{err} = \mathbf{q}_d^{-1}(s) \otimes \mathbf{q} = \{\eta_{err}, \boldsymbol{\epsilon}_{err}\}$. The virtual fixture then applies a restoring torque proportional to the vector part of this error, $\boldsymbol{\epsilon}_{err}$:

$$\boldsymbol{\tau}_{ve} = -\mathbf{K}_o \boldsymbol{\epsilon}_{err} - \mathbf{D}_o \boldsymbol{\omega}_{err} \tag{3.4}$$

where $\mathbf{K}_o$ and $\mathbf{D}_o$ are symmetric positive-definite matrices representing the rotational stiffness and damping, and $\boldsymbol{\omega}_{err}$ is the angular velocity error. This mathematically rigorous extension ensures that the system can guide the user through complex rotational maneuvers while preserving the stagnation-free and geometrically consistent properties of the SSA framework.

Chapter 4

Control Framework for Safe Human-Robot Interaction

This chapter details the unified control framework developed to ensure safe and effective Physical Human-Robot Interaction (pHRI) across the different domains addressed in this thesis. As introduced in the case studies of Chapter 2.7, the experimental applications in upper-limb rehabilitation [67] and robot-assisted surgery [79] share a common requirement: the need for a control architecture that allows the user to dictate the task progression while the robot ensures geometric precision and safety.

The primary contribution of this chapter is to provide the rigorous theoretical validation of this framework. Relying on the theory of dissipative systems, we provide a formal proof of the system's passivity and asymptotic stability, demonstrating that the coupled human-robot system remains stable regarding both task space and internal null-space dynamics.

4.1 Theoretical Framework of Dissipativity and Passivity

The stability analysis presented in this thesis is grounded in the theory of dissipative systems, as detailed in [80].

A state-space system Σ is defined as *dissipative* with respect to a given *supply rate* $s(u, y)$ if there exists a storage function $S : X \to \boldsymbol{R}^+$, such that for all initial conditions $\boldsymbol{x}(t_0) = \boldsymbol{x}_0$ and all admissible input functions $u(\cdot)$, the following dissipation inequality is satisfied for $t_1 \geq t_0$:

$$S(\boldsymbol{x}(t_1)) \leq S(\boldsymbol{x}(t_0)) + \int_{t_0}^{t_1} s(u(t), y(t))\, dt \tag{4.1}$$

This inequality expresses the physical concept that the stored energy $S(\boldsymbol{x}(t_1))$ in a system at a future time t_1 is at most equal to the stored energy at the present time t_0, plus the total energy externally supplied during the time interval $[t_0, t_1]$. No "internal creation of energy" is possible; only internal dissipation of energy is allowed.

4.1.1 Necessary Conditions for the Storage Function

To define a suitable storage function S for studying passivity, the following main conditions are necessary:

- **Non-Negativity (Stored Energy Condition):** The storage function $S(\boldsymbol{x})$ must be non-negative: $S : X \to \boldsymbol{R}^+$, where $\boldsymbol{R}^+ = [0, \infty)$.
- **Exception:** If S is not necessarily non-negative ($S : X \to \boldsymbol{R}$), the system is called *cyclo-dissipative*.

4.1.2 Passivity as a Specific Case of Dissipativity

Passivity is a specific case of dissipativity, defined with respect to a particular supply rate:

- **Supply Rate for Passivity:** $s(u, y) = u^T y$.

In this context, $u^T y$ typically represents the instantaneous externally supplied power. A system is passive if it is dissipative with respect to this supply rate, meaning the storage function $S \geq 0$ satisfies the integral inequality:

$$\int_{t_0}^{t_1} u(t)^T y(t)\, dt \geq S(\boldsymbol{x}(t_1)) - S(\boldsymbol{x}(t_0)) \tag{4.2}$$

In differential form, assuming that the storage function S is continuously differentiable (C^1), this translates into the inequality:

$$\frac{d}{dt} S \leq u^T y \tag{4.3}$$

4.2 Hybrid Interaction Control Architecture

Building on these theoretical foundations, the proposed architecture decouples the management of task progression from task accuracy. The overall system dynamics is modeled as the interconnection of three subsystems: the human operator, the virtual proxy dynamics, and the controlled robot.

4.2.1 Admittance-Based Task Progression

The generation of the reference motion relies on the Dynamic Proxy approach. As derived in the previous chapter using the SSA, the evolution of the virtual mass along the path is governed by:

$$m\ddot{s} + b\dot{s} = f_{||} \tag{4.4}$$

where $f_{||}$ is the projection of the user's force along the path tangent. The scalar variables $s, \dot{s}, \ddot{s}$ are used to compute the full kinematic state of the reference frame in the Cartesian space via the chain rule:

$$\boldsymbol{x_d(t)} = \varphi(s(t)) \tag{4.5}$$

$$\dot{\boldsymbol{x}}_{\boldsymbol{d}}\boldsymbol{(t)} = \varphi'(s)\dot{s}(t) \tag{4.6}$$

$$\ddot{\boldsymbol{x}}_{\boldsymbol{d}}\boldsymbol{(t)} = \varphi''(s)\dot{s}^2(t) + \varphi'(s)\ddot{s}(t) \tag{4.7}$$

4.2.2 Impedance-Based Accuracy Enforcement

The selection of an impedance-based control strategy for the inner loop is motivated by the fundamental requirements of physical safety and interaction stability.

As established in the seminal work by Hogan [17], the physical interaction between a manipulator and a dynamic environment (in this case, the human operator) cannot be safely managed by regulating position or force in isolation. Instead, the controller must regulate the dynamic relationship between the two, known as mechanical impedance. Unlike traditional high-gain position control, which renders the robot stiff and potentially dangerous in case of unexpected collisions, impedance control allows the robot to behave as a mass-spring-damper system. This compliant behavior ensures that contact forces remain bounded even in the presence of trajectory tracking errors caused by the user's intervention or involuntary movements [81].

This approach has become the standard for safe pHRI in torque-controlled manipulators [82], as it guarantees that the robot yields to external forces rather than fighting them. Specifically, this layer ensures that the robot complies with the geometric constraints defined by the VF while maintaining a compliant behavior.

The closed-loop dynamics of the robot is described by:

$$\boldsymbol{M}_A(\boldsymbol{q})\ddot{\tilde{\boldsymbol{x}}} + \boldsymbol{K}_D\dot{\tilde{\boldsymbol{x}}} + \boldsymbol{f}_{el} = \boldsymbol{f}_h \tag{4.8}$$

where $\tilde{\boldsymbol{x}} = \boldsymbol{x} - \boldsymbol{x}_d$ is the error, $\boldsymbol{M}_A$ is the inertia matrix, $\boldsymbol{K}_D$ is the damping, and $\boldsymbol{f}_{el}$ is the elastic force derived from a potential $U_{el}(\tilde{\boldsymbol{x}})$.

4.3 Passivity and Stability Analysis

Safety is the paramount requirement for pHRI in medical contexts. To rigorously guarantee that the system remains stable when coupled with a human operator, we apply the framework of dissipative systems introduced in Section 4.1. The analysis proceeds by defining a storage function for the controlled system and proving its passivity with respect to the interaction port defined by the input force $\boldsymbol{f}_h$ and the output velocity $\mathtt{v}$.

4.3.1 Energy Storage Function

We define a candidate storage function $S_r(\boldsymbol{\xi})$ representing the total "virtual energy" of the system. The state vector is defined as $\boldsymbol{\xi} = [\dot{s}, \tilde{\boldsymbol{x}}, \dot{\tilde{\boldsymbol{x}}}]^T$. The function is composed of the kinetic energy of the proxy (Eq. 4.4), the kinetic energy of the error weighted by the robot's inertia, and the potential energy of the virtual constraints:

$$S_r(\boldsymbol{\xi}) = \underbrace{\frac{1}{2} m \dot{s}^2}_{Kinetic\ (Proxy)} + \underbrace{\frac{1}{2} \dot{\tilde{\boldsymbol{x}}}^T \boldsymbol{M}_A(\boldsymbol{q}) \dot{\tilde{\boldsymbol{x}}}}_{Inertia\ Weighted\ Error} + \underbrace{U_{el}(\tilde{\boldsymbol{x}})}_{Potential\ (Elastic)} \tag{4.9}$$

Assuming $m > 0$, $\boldsymbol{M}_A(\boldsymbol{q})$ positive definite, and $U_{el}(\tilde{\boldsymbol{x}}) \geq 0$, this function is strictly non-negative ($S_r \geq 0$).

4.3.2 Proof of Robot Passivity

To prove the passivity of the system, we analyze the time derivative of the storage function defined in Eq. 4.9. The total derivative is the sum of the derivatives of its three components:

$$\dot{S}_r = \dot{S}_{proxy} + \dot{S}_{elastic} + \dot{S}_{inertia} \tag{4.10}$$

We compute each term explicitly to demonstrate how the interaction forces and dissipative terms combine.

1. Derivative of Proxy Kinetic Energy Differentiating the first term and substituting the proxy dynamics from Eq. 4.4 ($m\ddot{s} = f_{||} - b\dot{s}$):

$$\dot{S}_{proxy} = \frac{d}{dt}\left(\frac{1}{2}m\dot{s}^2\right) = m\dot{s}\ddot{s} = \dot{s}(f_{||} - b\dot{s}) = \dot{s}f_{||} - b\dot{s}^2 \tag{4.11}$$

Recalling that $f_{||}$ is the projection of the user force $\boldsymbol{f}_h$ onto the path tangent ($\boldsymbol{\varphi}'(s)$), and that the reference velocity is $\dot{\boldsymbol{x}}_d = \boldsymbol{\varphi}'(s)\dot{s}$, we can rewrite the power input term as:

$$\dot{s}f_{||} = \dot{s}(\boldsymbol{\varphi}'(s)^T\boldsymbol{f}_h) = (\dot{s}\boldsymbol{\varphi}'(s))^T\boldsymbol{f}_h = \dot{\boldsymbol{x}}_d^T\boldsymbol{f}_h \tag{4.12}$$

Thus, the derivative of the proxy energy becomes:

$$\dot{S}_{proxy} = \dot{\boldsymbol{x}}_d^T\boldsymbol{f}_h - b\dot{s}^2 \tag{4.13}$$

2. Derivative of Elastic Potential Energy The time derivative of the potential energy depends on the gradient of the potential function U_{el}:

$$\dot{S}_{elastic} = \frac{d}{dt}U_{el}(\tilde{\boldsymbol{x}}) = \left(\frac{\partial U_{el}}{\partial \tilde{\boldsymbol{x}}}\right)\dot{\tilde{\boldsymbol{x}}} \tag{4.14}$$

By definition, the elastic force is derived from this potential as $\boldsymbol{f}_{el}(\tilde{\boldsymbol{x}}) = \nabla U_{el}(\tilde{\boldsymbol{x}})^T$. Therefore:

$$\dot{S}_{elastic} = \boldsymbol{f}_{el}(\tilde{\boldsymbol{x}})^T\dot{\tilde{\boldsymbol{x}}} = \dot{\tilde{\boldsymbol{x}}}^T\boldsymbol{f}_{el}(\tilde{\boldsymbol{x}}) \tag{4.15}$$

3. Derivative of Inertia-Weighted Error Energy Differentiating the quadratic term involving the state-dependent inertia matrix $\boldsymbol{M}_A(\boldsymbol{q})$ requires the use of the product rule:

$$\dot{S}_{inertia} = \frac{d}{dt}\left(\frac{1}{2}\dot{\tilde{\boldsymbol{x}}}^T\boldsymbol{M}_A\dot{\tilde{\boldsymbol{x}}}\right) = \dot{\tilde{\boldsymbol{x}}}^T\boldsymbol{M}_A\ddot{\tilde{\boldsymbol{x}}} + \frac{1}{2}\dot{\tilde{\boldsymbol{x}}}^T\dot{\boldsymbol{M}}_A\dot{\tilde{\boldsymbol{x}}} \tag{4.16}$$

From the closed-loop robot dynamics (Eq. 4.8), we isolate the inertial term $\boldsymbol{M}_A\ddot{\tilde{\boldsymbol{x}}}$. Note that we explicitly consider the Coriolis/Centrifugal term $\boldsymbol{C}_A\dot{\tilde{\boldsymbol{x}}}$ which is inherent to the operational space dynamics:

$$\boldsymbol{M}_A\ddot{\tilde{\boldsymbol{x}}} = \boldsymbol{f}_h - \boldsymbol{K}_D\dot{\tilde{\boldsymbol{x}}} - \boldsymbol{f}_{el}(\tilde{\boldsymbol{x}}) - \boldsymbol{C}_A\dot{\tilde{\boldsymbol{x}}}$$

Substituting this into the derivative:

$$\dot{S}_{inertia} = \dot{\tilde{\boldsymbol{x}}}^T \left(\boldsymbol{f}_h - \boldsymbol{K}_D \dot{\tilde{\boldsymbol{x}}} - \boldsymbol{f}_{el} - \boldsymbol{C}_A \dot{\tilde{\boldsymbol{x}}} \right) + \frac{1}{2} \dot{\tilde{\boldsymbol{x}}}^T \dot{\boldsymbol{M}}_A \dot{\tilde{\boldsymbol{x}}} \tag{4.17}$$

$$= \dot{\tilde{\boldsymbol{x}}}^T \boldsymbol{f}_h - \dot{\tilde{\boldsymbol{x}}}^T \boldsymbol{K}_D \dot{\tilde{\boldsymbol{x}}} - \dot{\tilde{\boldsymbol{x}}}^T \boldsymbol{f}_{el} + \underbrace{\frac{1}{2} \dot{\tilde{\boldsymbol{x}}}^T (\dot{\boldsymbol{M}}_A - 2\boldsymbol{C}_A) \dot{\tilde{\boldsymbol{x}}}}_{=0} \tag{4.18}$$

The last term vanishes due to the fundamental skew-symmetric property of robotic systems, i.e., $\boldsymbol{x}^T (\dot{\boldsymbol{M}}_A - 2\boldsymbol{C}_A) \boldsymbol{x} = 0$. Thus:

$$\dot{S}_{inertia} = \dot{\tilde{\boldsymbol{x}}}^T \boldsymbol{f}_h - \dot{\tilde{\boldsymbol{x}}}^T \boldsymbol{K}_D \dot{\tilde{\boldsymbol{x}}} - \dot{\tilde{\boldsymbol{x}}}^T \boldsymbol{f}_{el} \tag{4.19}$$

Total Power Balance Summing the three contributions from Eqs. 4.13, 4.15, and 4.19:

$$\dot{S}_r = (\dot{\boldsymbol{x}}_d^T \boldsymbol{f}_h - b\dot{s}^2) + (\dot{\tilde{\boldsymbol{x}}}^T \boldsymbol{f}_{el}) + (\dot{\tilde{\boldsymbol{x}}}^T \boldsymbol{f}_h - \dot{\tilde{\boldsymbol{x}}}^T \boldsymbol{K}_D \dot{\tilde{\boldsymbol{x}}} - \dot{\tilde{\boldsymbol{x}}}^T \boldsymbol{f}_{el}) \tag{4.20}$$

The terms involving the elastic force $\boldsymbol{f}_{el}$ cancel out exactly. Grouping the remaining terms by the input force $\boldsymbol{f}_h$:

$$\dot{S}_r = (\dot{\boldsymbol{x}}_d + \dot{\tilde{\boldsymbol{x}}})^T \boldsymbol{f}_h - b\dot{s}^2 - \dot{\tilde{\boldsymbol{x}}}^T \boldsymbol{K}_D \dot{\tilde{\boldsymbol{x}}} \tag{4.21}$$

Recalling that the actual robot velocity is $\dot{\mathbf{x}} = \dot{\boldsymbol{x}}_d + \dot{\tilde{\boldsymbol{x}}}$, we arrive at the final power balance equation:

$$\dot{S}_r = \dot{\boldsymbol{x}}^T \boldsymbol{f}_h \underbrace{- b\dot{s}^2 - \dot{\tilde{\boldsymbol{x}}}^T \boldsymbol{K}_D \dot{\tilde{\boldsymbol{x}}}}_{\leq 0} \tag{4.22}$$

Since the damping parameters b and $\boldsymbol{K}_D$ are positive definite, the term in the brackets represents strictly non-positive dissipated power. Consequently, the inequality $\dot{S}_r \leq \dot{\boldsymbol{x}}^T \boldsymbol{f}_h$ holds. This formally proves that the controlled robot is a *passive* system: it does not generate internal energy but only dissipates the energy injected by the user $\boldsymbol{f}_h$.

4.4 Passivity and Stability of the Interconnected Human-Robot System

We now analyze the passivity and stability of the overall system formed by the physical interconnection of the human operator Σ_h and the controlled robot system Σ_r. The analysis relies on the principle that the interconnection of passive

systems is itself passive, as detailed in [80].

4.4.1 Framework for Interconnection of Dissipative Systems

According to the theory of dissipative systems (Chapter 3, Section 3.3 of [80]), we can analyze the passivity of a large-scale system by considering its components.

Let us consider k systems Σ_i, each being dissipative with respect to a supply rate $s_i(u_i, y_i)$ and having a storage function $S_i(\boldsymbol{x_i})$. If these systems are interconnected via an interconnection structure I (which may include external ports $\langle u^e, y^e \rangle$), a fundamental result (Proposition 3.3.1 in [80]) states:

If the interconnection is such that the sum of the internal supply rates is less than or equal to the power supplied through the external ports, i.e.,

$$\sum_{i=1}^{k} s_i(u_i, y_i) \leq s^e(u^e, y^e) \tag{4.23}$$

then the interconnected system Σ_I is dissipative with respect to the external supply rate s^e. Furthermore, the total storage function for the interconnected system is the sum of the individual storage functions: $S(\boldsymbol{x}_1, \ldots, \boldsymbol{x}_k) = \sum_{i=1}^{k} S_i(\boldsymbol{x}_i)$

A crucial case for stability analysis (Eq. 3.54 in [80]) occurs when there are no external ports ($s^e = 0$) and the interconnection is **power-conserving**, meaning the sum of internal supply rates is zero or negative:

$$\sum_{i=1}^{k} s_i(u_i, y_i) \leq 0 \tag{4.24}$$

In this case, the interconnected system is passive with respect to the zero supply rate, and its total stored energy S is non-increasing ($\dot{S} \leq 0$), which forms the basis for Lyapunov stability analysis.

4.4.2 Passivity of the Interconnected System

We apply this framework to the human-robot system.

1. **Subsystem 1: Human (Σ_h).** We assume the human operator behaves passively at the interaction port. Let $\boldsymbol{x}_h$ be the internal state of the human. The interaction port involves the velocity $\dot{\boldsymbol{x}}$ and the force applied *by the robot on the human*, which is $-\boldsymbol{f}_h$. We assume there exists a storage function

$S_h(\boldsymbol{x}_h) \geq 0$ such that:

$$\dot{S}_h \leq \dot{\boldsymbol{x}}^T(-\boldsymbol{f}_h) \tag{4.25}$$

This represents passivity with respect to the port $\langle \dot{\boldsymbol{x}}, -\boldsymbol{f}_h \rangle$.

2. **Subsystem 2: Controlled Robot (Σ_r).** As proven in Section 4.3, this system is passive with respect to the port $\langle \dot{\boldsymbol{x}}, \boldsymbol{f}_h \rangle$, with storage function $S_r(\boldsymbol{\xi}) \geq 0$ satisfying $\dot{S}_r \leq \dot{\boldsymbol{x}}^T \boldsymbol{f}_h$.

3. **Interconnection.** The physical interaction imposes $\dot{\boldsymbol{x}}_h = \dot{\boldsymbol{x}}_r = \dot{\boldsymbol{x}}$ and $F_{\text{on H}} + F_{\text{on R}} = (-\boldsymbol{f}_h) + \boldsymbol{f}_h = 0$. This is a power-conserving interconnection where the sum of supply rates at the interaction port is zero: $s_h + s_r = \dot{\boldsymbol{x}}^T(-\boldsymbol{f}_h) + \dot{\boldsymbol{x}}^T \boldsymbol{f}_h = 0$.

4. **Conclusion.** Since the interconnection is power-conserving ($s_h + s_r = 0 \leq 0$) and has no external ports, the interconnected system is passive with respect to the zero supply rate. The total storage function is the sum of the individual storage functions:

$$S_{total}(\boldsymbol{x}_h, \boldsymbol{\xi}) = S_h(\boldsymbol{x}_h) + S_r(\boldsymbol{\xi}) \geq 0 \tag{4.26}$$

The derivative of the total storage function satisfies:

$$\dot{S}_{total} = \dot{S}_h + \dot{S}_r \leq [\dot{\boldsymbol{x}}^T(-\boldsymbol{f}_h)] + [\dot{\boldsymbol{x}}^T \boldsymbol{f}_h - b\dot{s}^2 - \dot{\tilde{\boldsymbol{x}}}^T K_D \dot{\tilde{\boldsymbol{x}}}] \tag{4.27}$$

$$\dot{S}_{total} \leq -b\dot{s}^2 - \dot{\tilde{\boldsymbol{x}}}^T K_D \dot{\tilde{\boldsymbol{x}}} \leq 0 \tag{4.28}$$

This confirms the passivity of the overall interconnected system.

4.4.3 Stability via Direct Lyapunov Method

We now use $V = S_{total}$ as a candidate Lyapunov function to prove stability.

- **Condition 1: Positive Definiteness.** We analyze $V(\boldsymbol{x_{total}}) = S_h(\boldsymbol{x}_h) + S_r(\boldsymbol{\xi})$ near the equilibrium $\boldsymbol{x}^*_{\boldsymbol{total}} = (\boldsymbol{x}^*_h, \boldsymbol{\xi}^*)$.
  - $S_r(\boldsymbol{\xi})$ has a **strict local minimum** at $\boldsymbol{\xi}^* = (0, 0, 0)$, as S_r is the sum of non-negative kinetic and potential terms which are zero only at $\boldsymbol{\xi}^*$ (assuming $m > 0, M_A > 0, U_{el}$ positive definite).
  - $S_h(\boldsymbol{x}_h)$ is **assumed** to have a **strict local minimum** at $\boldsymbol{x}^*_h$.

  - Since $V = S_{total}$ is the sum of two functions that are non-negative and both have strict local minima at their respective components of $\boldsymbol{x}^*_{\boldsymbol{total}}$, V itself has a **strict local minimum** at $\boldsymbol{x}^*_{\boldsymbol{total}}$.
  - Therefore, $V(\boldsymbol{x}_{\boldsymbol{total}})$ is **locally positive definite** around $\boldsymbol{x}^*_{\boldsymbol{total}}$.

- **Condition 2: Negative Semidefinite Derivative.**
  - From (4.27), we have $\dot{V} = \dot{S}_{total} \leq 0$.
  - The derivative $\dot{V}$ is **negative semidefinite** (or non-positive).

- **Conclusion (Lyapunov Stability):** Both conditions of the Lyapunov Stability Theorem are met. Proposition 4.3.1(iii) in [80] specifically applies this logic to interconnected passive systems, stating that if the storage functions have strict local minima at the equilibrium, the equilibrium is stable.

  Therefore, the equilibrium $\boldsymbol{x}^*_{\boldsymbol{total}}$ of the interconnected human-robot system is stable in the sense of Lyapunov.

4.4.4 Equilibrium Set and Boundedness of s Analysis

The stability analysis in Section 4.4.3 uses the storage function $S_{total} = S_h(\boldsymbol{x}_h) + S_r(\boldsymbol{\xi})$, whit the state $\boldsymbol{\xi}$ previously defined. A critical observation is that this storage function is not positive definite with respect to the full state of the system, as it lacks dependency on the path coordinate s.

The system is not designed to converge to a single, unique equilibrium point (e.g., $s = 0$), but rather to a *continuum of equilibria*.

The Equilibrium Set

For the autonomous (unforced) system where $\boldsymbol{f}_h = 0$, the system dynamics become:

$$\boldsymbol{M}_A(\boldsymbol{q})\ddot{\tilde{\boldsymbol{x}}} + \boldsymbol{K}_D\dot{\tilde{\boldsymbol{x}}} + \boldsymbol{f}_{el}(\tilde{\boldsymbol{x}}) = 0 \tag{4.29}$$

$$m\ddot{s} + b\dot{s} = 0 \tag{4.30}$$

The set of all equilibrium points is found by setting all velocities and accelerations to zero. This yields:

- From the s dynamics: $\dot{s} = 0, \ddot{s} = 0$.

- From the $\tilde{x}$ dynamics: $\dot{\tilde{\boldsymbol{x}}} = 0, \ddot{\tilde{\boldsymbol{x}}} = 0 \implies \boldsymbol{f}_{el}(\tilde{\boldsymbol{x}}) = 0$.

Since $\boldsymbol{f}_{el}(\tilde{\boldsymbol{x}})$ is derived from a positive definite potential $U_{el}(\tilde{\boldsymbol{x}})$, $\boldsymbol{f}_{el}(\tilde{\boldsymbol{x}}) = 0$ if and only if $\tilde{\boldsymbol{x}} = 0$.

Therefore, the **equilibrium set** $\mathcal{E}$ is defined as:

$$\mathcal{E} = \{(s, \boldsymbol{\xi}) \mid \boldsymbol{\xi} = 0, s \in [0, L_{path}]\} \tag{4.31}$$

Geometrically, this set $\mathcal{E}$ is an *equilibrium manifold*. This manifold corresponds to the geometric task-space path $\varphi(s)$ itself, embedded within the system's full state space. It represents any configuration where the robot is at rest ($\dot{s} = 0, \dot{\tilde{\boldsymbol{x}}} = 0$) and perfectly on the path ($\tilde{\boldsymbol{x}} = 0$), regardless of the position s along the path. Geometrically, this set $\mathcal{E}$ is an *equilibrium manifold*. This manifold corresponds to the geometric task-space path $\boldsymbol{\varphi}(s)$ itself, embedded within the system's full state space. It represents any configuration where the robot is at rest ($\dot{s} = 0, \dot{\tilde{\boldsymbol{x}}} = 0$) and perfectly on the path ($\tilde{\boldsymbol{x}} = 0$), regardless of the position s along the path. This perfectly encapsulates the fundamental requirement for passive guidance in general pHRI applications: the collaborative robot must act as a stable, stationary guide that remains safely at rest along the prescribed path the moment the human operator ceases to apply intentional interaction forces.

Boundedness of s

A concern arising from $\dot{S}_{total} \leq 0$ (negative semidefinite) is that the state s might "drift" or "move on and on" towards infinity. We now formally prove that the displacement of s is finite.

Consider the autonomous dynamics for s with $f_{||} = 0$:

$$m\ddot{s} + b\dot{s} = 0 \tag{4.32}$$

This is a first-order linear differential equation for the velocity $v_s = \dot{s}$. As shown by Laplace transform analysis, the solution for an initial velocity $v_s(0) = \dot{s}(0)$ is a simple exponential decay:

$$\dot{s}(t) = \dot{s}(0)e^{-\frac{b}{m}t} = \dot{s}(0)e^{-t/\tau} \tag{4.33}$$

where $\tau = m/b$ is the time constant of the virtual mass dynamics.

While it is true that $\dot{s}(t)$ only asymptotically reaches zero in infinite time, the

total displacement Δs is the integral of this velocity, which is finite:

$$\Delta s = \int_0^\infty \dot{s}(t)\, dt = \int_0^\infty \dot{s}(0) e^{-t/\tau}\, dt \tag{4.34}$$

Solving the definite integral:

$$\Delta s = \dot{s}(0) \left[-\tau e^{-t/\tau}\right]_0^\infty = \dot{s}(0) \left(0 - (-\tau e^0)\right) = \dot{s}(0)\tau \tag{4.35}$$

Substituting $\tau = m/b$:

$$\Delta s = \frac{m\dot{s}(0)}{b} \tag{4.36}$$

This proves that the total displacement of the virtual mass is finite and bounded. The state s asymptotically converges to a finite value $s_{final} = s(0) + \Delta s$. Consequently, the desired Cartesian pose $\boldsymbol{x_d}(s) = \varphi(s)$, being a continuous function of s, also converges to a finite, stable pose.

4.5 Redundancy and Null Space Stability

The stability analysis in Section 4.4.3 proves the convergence of the task-space state $\boldsymbol{\xi}$. However, this analysis alone is insufficient to guarantee the stability of the *entire* system state. Since the robot is kinematically redundant ($n = 7 > m = 6$), the task-space velocity convergence ($\dot{\boldsymbol{x}} = \boldsymbol{J(q)}\dot{\boldsymbol{q}} \to 0$) does not imply that the joint velocities converge ($\dot{q} \to 0$). Energy could potentially "build up" in the null space, leading to internal robot motions even while the end-effector remains stable. It is therefore necessary to formally demonstrate the stability of the internal, or null space, dynamics to ensure the full system state converges to a stable equilibrium.

To formally prove the stability of the full system, including the internal null space dynamics, we adopt the hierarchical framework of **Successive Convergence**, as presented in [82].

We define a two-level task hierarchy:

- **Level 1 (Primary Task):** The Cartesian impedance control.
- **Level 2 (Secondary Task):** A joint-space controller to prevent joint limit violations.

Hierarchical Control Law

We augment the control law to include a secondary, projected torque command. The total control torque $\boldsymbol{\tau}_{tot}$ is defined as:

$$\boldsymbol{\tau}_{tot} = \boldsymbol{\tau}_1 + \boldsymbol{\tau}_2 + \boldsymbol{g}(\boldsymbol{q}) \tag{4.37}$$

where $\boldsymbol{g}(\boldsymbol{q})$ compensates for gravity, $\boldsymbol{\tau}_1$ is the primary task torque, and $\boldsymbol{\tau}_2$ is the secondary null space torque.

1. **Primary Task Torque $\boldsymbol{\tau}_1$:** This is the torque required to implement the Cartesian impedance, which we can write as $\boldsymbol{\tau}_1 = \boldsymbol{J}(\boldsymbol{q})^T \boldsymbol{f_{imp}}$, where $\boldsymbol{f_{imp}}$ is the commanded Cartesian impedance force.

2. **Secondary Task Torque $\boldsymbol{\tau}_2$:** This torque must only act in the null space of the primary task. To ensure dynamic decoupling [82], we first define the (6×6) *operational space inertia matrix* $\boldsymbol{\Lambda}(\boldsymbol{q})$:

   $$\boldsymbol{\Lambda}(\boldsymbol{q}) = \left(\boldsymbol{J}(\boldsymbol{q})\boldsymbol{M}(\boldsymbol{q})^{-1}\boldsymbol{J}^T(\boldsymbol{q})\right)^{-1} \tag{4.38}$$

   Using this, the (7×6) **dynamically consistent pseudoinverse $\bar{\boldsymbol{J}}(\boldsymbol{q})$** is defined as:

   $$\bar{\boldsymbol{J}}(\boldsymbol{q}) = \boldsymbol{M}(\boldsymbol{q})^{-1}\boldsymbol{J}(\boldsymbol{q})^T\boldsymbol{\Lambda}(\boldsymbol{q}) \tag{4.39}$$

   The (7×7) *dynamically consistent null space projector* is then:

   $$\boldsymbol{N}(\boldsymbol{q}) = \boldsymbol{I} - \boldsymbol{J}(\boldsymbol{q})^T\bar{\boldsymbol{J}}(\boldsymbol{q})^T \tag{4.40}$$

   The secondary torque $\boldsymbol{\tau}_2$ is defined by projecting the null space command $\boldsymbol{\tau}_{null}$ using $\boldsymbol{N}(\boldsymbol{q})^T$:

   $$\boldsymbol{\tau}_2 = \boldsymbol{N}(\boldsymbol{q})\boldsymbol{\tau}_{null} \quad \text{where} \quad \boldsymbol{\tau}_{null} = (-\nabla V_2(\boldsymbol{q}) - \boldsymbol{D_2}\dot{\boldsymbol{q}}) \tag{4.41}$$

   The components of $\boldsymbol{\tau}_{null}$ are defined as:

   - $V_2(\boldsymbol{q})$ is an artificial potential function (e.g., $V_2(\boldsymbol{q}) = \frac{k}{2}\sum_i(\boldsymbol{q}_i - \boldsymbol{q}_{mid,i})^2$) that penalizes proximity to joint limits.
   - D_2 is a positive definite damping matrix ($\boldsymbol{D_2} > 0$) that dissipates energy in the null space.

This formulation ensures that $\boldsymbol{\tau}_2$ generates joint accelerations that are orthogonal to the primary task space, guaranteeing dynamic decoupling [82].

Proof of Stability via Successive Convergence

We apply the Conditional Stability theorem by analyzing the storage functions for each level sequentially, under the autonomous condition ($\boldsymbol{f}_h = 0$).

Step 1: Stability of the Primary Task (Level 1) We use the storage function $S_1 = S_r(\boldsymbol{\xi})$ defined in Eq. (4.9). As proven in Eq. (4.22), its time derivative (with $\boldsymbol{f}_h = 0$) is:

$$\dot{S}_1 = -b\dot{s}^2 - \dot{\tilde{\boldsymbol{x}}}^T \boldsymbol{K}_D \dot{\tilde{\boldsymbol{x}}} \leq 0 \tag{4.42}$$

By LaSalle's Invariance Principle, all system trajectories converge to the largest invariant set $\mathcal{A}_1$ where $\dot{S}_1 = 0$.

$$\mathcal{A}_1 = \{(q, \dot{q}) \mid \dot{s} = 0, \tilde{\boldsymbol{x}} = 0, \dot{\tilde{\boldsymbol{x}}} = 0\} \tag{4.43}$$

This set $\mathcal{A}_1$ is the equilibrium set for the primary task. It implies that the Cartesian error converges to zero ($\tilde{\boldsymbol{x}} \to 0$) and the end-effector velocity converges to zero. However, $\mathcal{A}_1$ only implies $\boldsymbol{J}(\boldsymbol{q})\dot{\boldsymbol{q}} = 0$. Due to redundancy, this does not guarantee $\dot{\boldsymbol{q}} = 0$.

Step 2: Stability of the Secondary Task (Conditioned on $\mathcal{A}_1$) We now analyze the internal dynamics restricted to the invariant set $\mathcal{A}_1$. We define a storage function S_2 for the secondary task, representing the total internal energy of the robot plus the artificial potential for joint limits:

$$S_2(\boldsymbol{q}, \dot{\boldsymbol{q}}) = \frac{1}{2}\dot{\boldsymbol{q}}^T \boldsymbol{M}(\boldsymbol{q})\dot{\boldsymbol{q}} + V_2(\boldsymbol{q}) \tag{4.44}$$

We compute the time derivative of S_2 along the system trajectories, conditioned on being in $\mathcal{A}_1$. The power balance of the manipulator is:

$$\dot{S}_2 = \frac{d}{dt}\left(\frac{1}{2}\dot{\boldsymbol{q}}^T \boldsymbol{M}(\boldsymbol{q})\dot{\boldsymbol{q}}\right) + \frac{d}{dt}(V_2(\boldsymbol{q})) = \dot{\boldsymbol{q}}^T(\boldsymbol{M}(\boldsymbol{q})\ddot{\boldsymbol{q}} + \boldsymbol{C}\dot{\boldsymbol{q}}) + (\nabla V_2)^T\dot{\boldsymbol{q}} \tag{4.45}$$

From the robot dynamics, we substitute $\boldsymbol{M}(\boldsymbol{q})\ddot{\boldsymbol{q}} + \boldsymbol{C}\dot{\boldsymbol{q}} = \boldsymbol{\tau}_{tot} - \boldsymbol{g}(\boldsymbol{q})$:

$$\dot{S}_2 = \dot{\boldsymbol{q}}^T(\boldsymbol{\tau}_{tot} - \boldsymbol{g}(\boldsymbol{q})) + (\nabla V_2)^T\dot{\boldsymbol{q}} \tag{4.46}$$

Now, substitute the control law $\boldsymbol{\tau}_{tot} = \boldsymbol{\tau}_1 + \boldsymbol{\tau}_2 + \boldsymbol{g}(\boldsymbol{q})$ from Eq. (4.37):

$$\dot{S}_2 = \dot{\boldsymbol{q}}^T(\boldsymbol{\tau}_1 + \boldsymbol{\tau}_2 + \boldsymbol{g}(\boldsymbol{q}) - \boldsymbol{g}(\boldsymbol{q})) + (\nabla V_2)^T\dot{\boldsymbol{q}} \tag{4.47}$$

$$\dot{S}_2 = \dot{\boldsymbol{q}}^T\boldsymbol{\tau}_1 + \dot{\boldsymbol{q}}^T\boldsymbol{\tau}_2 + \dot{\boldsymbol{q}}^T\nabla V_2 \tag{4.48}$$

We now evaluate this expression **conditioned on** $\mathcal{A}_1$:

- **Task 1:** In $\mathcal{A}_1$, we have $\boldsymbol{J}(\boldsymbol{q})\dot{\boldsymbol{q}} = 0$. The work of the primary task $\boldsymbol{\tau}_1 = \boldsymbol{J}(\boldsymbol{q})^T\boldsymbol{f}_{\boldsymbol{cart}}$ is zero:

$$\dot{\boldsymbol{q}}^T\boldsymbol{\tau}_1 = \dot{\boldsymbol{q}}^T J^T\boldsymbol{f}_{\boldsymbol{cart}} = (J\dot{\boldsymbol{q}})^T\boldsymbol{f}_{\boldsymbol{cart}} = (0)^T\boldsymbol{f}_{\boldsymbol{cart}} = 0$$

- **Task 2 (Work):** In $\mathcal{A}_1$, the joint velocity lies entirely in the null space ($\boldsymbol{J}\dot{\boldsymbol{q}} = 0$). We analyze the work done by the projected torque $\boldsymbol{\tau}_2 = \boldsymbol{N}(\boldsymbol{q})\boldsymbol{\tau}_{null}$. Using the property of the dynamically consistent projector where the transpose $\boldsymbol{N}(\boldsymbol{q})^T = (\boldsymbol{I} - \bar{\boldsymbol{J}}\boldsymbol{J})$ acts as a projector for velocities:

$$\begin{aligned}
\dot{\boldsymbol{q}}^T\boldsymbol{\tau}_2 &= \dot{\boldsymbol{q}}^T(\boldsymbol{N}(\boldsymbol{q})\boldsymbol{\tau}_{null}) \\
&= (\boldsymbol{N}(\boldsymbol{q})^T\dot{\boldsymbol{q}})^T\boldsymbol{\tau}_{null} \\
&= \left((\boldsymbol{I} - \bar{\boldsymbol{J}}\boldsymbol{J})\dot{\boldsymbol{q}}\right)^T\boldsymbol{\tau}_{null} \\
&= (\dot{\boldsymbol{q}} - \bar{\boldsymbol{J}}(\underbrace{\boldsymbol{J}\dot{\boldsymbol{q}}}_{=0}))^T\boldsymbol{\tau}_{null} \\
&= \dot{\boldsymbol{q}}^T\boldsymbol{\tau}_{null}
\end{aligned}$$

  Since we are conditioned on $\mathcal{A}_1$ ($\boldsymbol{J}\dot{\boldsymbol{q}} = 0$), the projection does not alter the work done by the secondary task on the internal motion.

The derivative $\dot{S}_2$ restricted to $\mathcal{A}_1$ simplifies to:

$$\dot{S}_2|_{\mathcal{A}_1} = \dot{\boldsymbol{q}}^T\boldsymbol{\tau}_{null} + \dot{\boldsymbol{q}}^T\nabla V_2 \tag{4.49}$$

Substitute the definition of $\boldsymbol{\tau}_{null} = -\nabla V_2 - \boldsymbol{D}_2\dot{\boldsymbol{q}}$:

$$\dot{S}_2|_{\mathcal{A}_1} = \dot{\boldsymbol{q}}^T(-\nabla V_2 - \boldsymbol{D}_2\dot{\boldsymbol{q}}) + \dot{\boldsymbol{q}}^T\nabla V_2 \tag{4.50}$$

The conservative potential terms cancel out:

$$\dot{S}_2|_{\mathcal{A}_1} = \underbrace{(-\dot{\boldsymbol{q}}^T\nabla V_2 + \dot{\boldsymbol{q}}^T\nabla V_2)}_{=0} - \dot{\boldsymbol{q}}^T\boldsymbol{D}_2\dot{\boldsymbol{q}} \tag{4.51}$$

This leaves only the dissipative term:

$$\dot{S}_2|_{\mathcal{A}_1} = -\dot{\boldsymbol{q}}^T \boldsymbol{D}_2 \dot{\boldsymbol{q}} \leq 0 \tag{4.52}$$

4.6 Conclusion and Theoretical Implications

In this chapter, presented the theoretical derivation and validation of the control framework supporting the applications of this thesis. By decoupling the task progression (Admittance) from the accuracy enforcement (Impedance), and by handling redundancy through null-space projection, we have defined a flexible architecture suitable for both rehabilitation and surgery.

The primary contribution of this chapter lies in the rigorous proof of stability for the interconnected human-robot system. Through the application of Lyapunov theory and the framework of dissipative systems, we have demonstrated that:

1. The robot behaves as a strictly passive system, dissipating energy injected by the user.

2. The coupled system is asymptotically stable, converging to the desired equilibrium manifold even in the presence of redundancy.

3. The internal null-space motions are strictly bounded and dissipative, preventing any hazardous energy build-up.

It is important to remark that this theoretical analysis considers *ideal operating conditions*. It assumes continuous-time dynamics, perfect knowledge of the dynamic model parameters (e.g., $\boldsymbol{M}(\boldsymbol{q}), \boldsymbol{g}(\boldsymbol{q})$), and the absence of discretization effects or communication delays. While real-world implementations inevitably introduce uncertainties and non-idealities, establishing stability in the nominal case is the fundamental prerequisite for safety.

This theoretical guarantee provides the certification that the control law is *structurally sound*. It ensures that the interaction mechanics are intrinsically stable: the system cannot generate energy to destabilize the interaction, but can only react passively to the human intent. This mathematical assurance effectively "unlocks" the possibility of performing physical Human-Robot Interaction, providing the necessary safety layer upon which the experimental applications described in the following chapters are built.

Chapter 5

Analysis of Stability, Sensitivity, and Transparency in Variable Admittance Control for pHRI

5.1 Introduction

The analysis presented in the previous chapter established a rigorous theoretical foundation for safe human-robot interaction, proving the asymptotic stability and passivity of the coupled system under ideal operating conditions. However, as anticipated in the conclusions of Chapter 4.6, the transition from theoretical derivation to real-world implementation inevitably exposes the control loop to physical limitations and parasitic effects—such as the phase lag introduced by the digital controller's sampling rate, communication bus latencies, joint elasticity, and actuator saturation—that were neglected in the nominal Lyapunov analysis.

While the theoretical guarantees of the ideal model provide the necessary certification of structural soundness, ensuring robust performance in experimental scenarios requires a deeper investigation into these non-idealities. In this context, the increasing focus on Physical Human-Robot Interaction (pHRI) and collaborative robotics has significantly expanded the range of potential applications, enabling assisted industrial manipulation, collaborative assembly, rehabilitation, and medical interventions. To achieve reliable interaction and ensure human safety under these realistic constraints, control strategies capable of ensuring robot compliance have been extensively developed [17]. Among these, admittance control [83] has proven particularly appealing in numerous practical scenarios due to its ability to shape the robot's dynamic behavior.

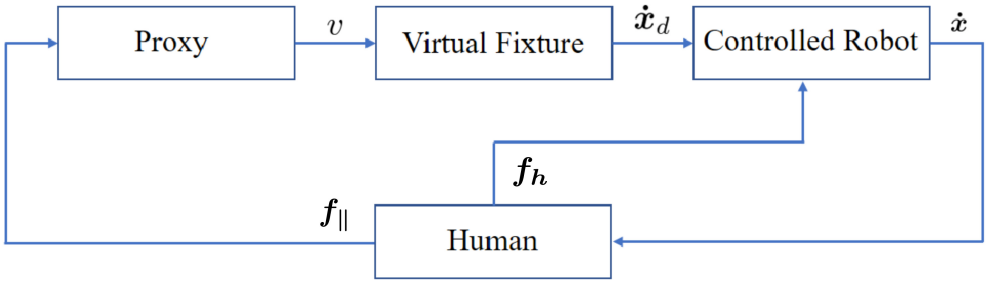

Figure 5.1: Schematic representation of the proxy-based pHRI framework enhanced by virtual fixtures [87].

5.1.1 Proxy-based Virtual Fixtures in pHRI

In this chapter, we specifically consider the hybrid impedance control for pHRI enhanced by Virtual Fixture (VF) [2]. These fixtures constrain the user's motion along a specific path [24], thereby reducing both cognitive and physical efforts during task execution. Specifically, a proxy-based virtual fixture definition is adopted.

In this framework, the human operator interacts with the proxy dynamics, which typically follows that of a mass-damper system constrained along a desired curve $\boldsymbol{\varphi}(\cdot)$. The motion of the proxy is generated by simulating its *forward dynamics*: the interaction forces applied by the user dictate the proxy's acceleration, which is integrated to obtain the desired reference velocity and position. These kinematic reference signals are subsequently fed to the robot's low-level controller, which physically tracks them by computing the required joint torques via a Cartesian *inverse dynamics* control law [84]. This paradigm is widely exploited to guide users in activities ranging from rehabilitation to precision tool operation [53], [67], [85], [86]. A schematic representation of this control framework is provided in Fig. 5.1.

5.1.2 Stability Challenges and Literature Gaps

Despite its advantages and rigorous theoretical stability proofs, the implementation of admittance control presents critical challenges regarding system stability [88]. In real-world applications, instability phenomena often manifest as deviations from the proxy position and high-frequency vibrations of the robot end-effector, compromising both safety and performance [89]. These issues are typically caused by improper tuning of the admittance parameters (m and b) and system delays due to control discretization and human reaction times [90].

An analysis of the state of the art reveals significant gaps in how these stability

issues are addressed:

- **Neglected Non-idealities:** Stability analyses generally rely on linear control theory [91], [92] or passivity concepts that consider ideal models. Parasitic effects such as joint elasticity, system delays, and—crucially—actuator saturation are rarely considered together, despite being intrinsic to physical robotic systems [93].
- **Lack of Consensus on Parameter Adaptation:** To prevent instability, various adaptation strategies have been proposed, focusing on adapting the mass only [91], the damping only [94], [95], or both simultaneously [96], [97]. However, there is no unified consensus in the literature on which of these approaches is most effective for ensuring stability in pHRI.
- **Virtual Fixtures Context:** While extensive research exists for unconstrained co-manipulation, the specific stability implications of pHRI enhanced by virtual fixtures have not been thoroughly explored.

5.1.3 Chapter Contributions

To address these gaps, this chapter extends the analysis of pHRI, specifically focusing on the use of proxy-based VFs. Based on the work presented in [87], a detailed analysis is conducted that explicitly includes system non-idealities, such as joint elasticity, time delays, and actuator saturation [98], [99]. The nonlinearity associated with actuator saturation is found to play a crucial role in explaining the undesired oscillatory behavior (limit cycles) observed in experimental tests.

Consequently, the contributions of this chapter are threefold:

1. A rigorous **stability analysis** using the Describing Function method and Nyquist plots to handle static nonlinearities and delays.
2. A **sensitivity analysis** to identify how different admittance parameters affect the stability of the overall system, resolving the ambiguity found in the literature regarding the most effective adaptation variable.
3. A novel **adaptation technique** for the proxy parameters, designed to maximize transparency [67], [86] while moving along the desired path, validated through both simulations and experimental results.

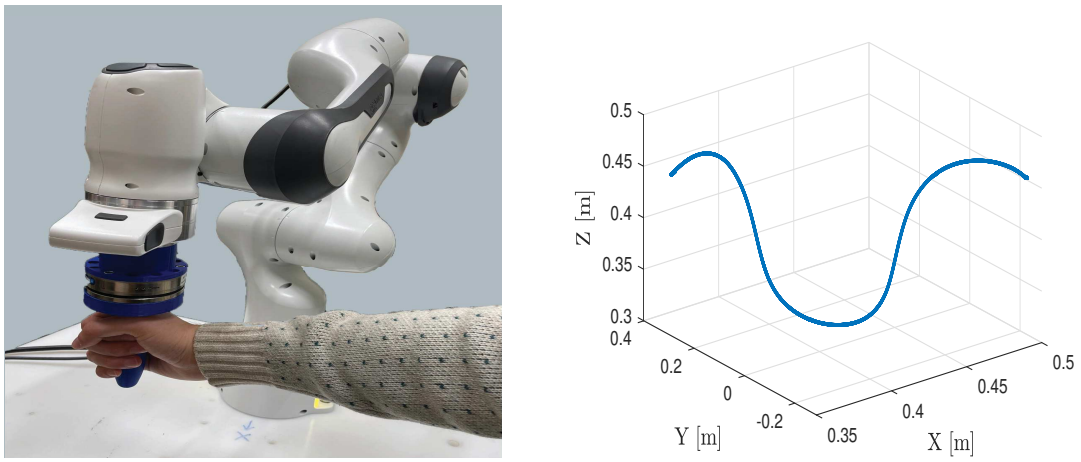

(a) (b)

Figure 5.2: Experimental robotic setup (a) and reference path used in the experimental tests (b).

5.2 Modeling of the pHRI System with Virtual Fixtures

The robotic setup considered in this work is based on the 7-DoF Franka Emika Panda collaborative robot equipped with an Axia80-M20 force-torque sensor on its terminal flange, as shown in Fig. 5.2(a). The user's limb is connected to the end-effector through a simple handle; however, different types of constraints can be designed depending on the application.

The user's motion is restricted along a generic path $\varphi(l)$, where l is the arc length, as shown in Fig. 5.2(b). This is achieved using a virtual mass called the *proxy* moving along the curve under the influence of the tangential component $f_{\parallel}$ of the user force.

5.2.1 Proxy and Human Dynamics

The interaction is mediated by the proxy, whose dynamics is defined as a mass-damper system:

$$m\dot{v} + bv = f_{\parallel} \tag{5.1}$$

where $v = \dot{l}$ is the velocity along the curve, m and b are the virtual mass and damping respectively, and $f_{\parallel} = \frac{d\varphi(l)}{dl}^T \boldsymbol{f}_h$ is the tangential component of the force applied by the human [83]. It is worth noting that the dynamics in (5.1) are deliberately expressed in terms of the velocity v rather than the path parameter. This choice avoids any potential ambiguity, as the symbol s—commonly used to

denote the arc-length parameter in differential geometry—is strictly reserved in the following analysis to represent the complex variable in the Laplace domain.

The transfer function of the proxy is therefore:

$$G_p(s) = \frac{V(s)}{F_{\|}(s)} = \frac{1}{ms + b} \tag{5.2}$$

The human operator is modeled as a spring-damper system, assuming the inertial component of the arm is negligible compared to the robot dynamics in the context of stability. In a linearized analysis around an operating point, the human dynamics can be expressed as:

$$G_h(s) = \frac{F_h(s)}{\dot{X}(s)} = \frac{b_h s + K_h}{s} \tag{5.3}$$

where b_h and K_h represent the damping and stiffness of the human arm, respectively [92], [100].

5.2.2 Controlled Robot Model

To define the reference for the robot controller, the virtual fixture shape is modeled through the relation between the proxy velocity along the curve and the velocity required to the robot:

$$\dot{\boldsymbol{x}}_d(t) = \frac{d\varphi(l)}{dl} v(t). \tag{5.4}$$

The position $\varphi(l(t))$ along the guiding virtual fixture is used as the reference position for the robot, under a Cartesian inverse dynamics control law:

$$\boldsymbol{\tau} = \boldsymbol{M}(\boldsymbol{q})\boldsymbol{y} + \boldsymbol{C}(\boldsymbol{q}, \dot{\boldsymbol{q}})\dot{\boldsymbol{q}} + \boldsymbol{g}(\boldsymbol{q}) \tag{5.5}$$

with the auxiliary input:

$$\boldsymbol{y} = \boldsymbol{J}^{-1}(\boldsymbol{q}) \left(\ddot{\boldsymbol{x}}_d - \dot{\boldsymbol{J}}(\boldsymbol{q})\dot{\boldsymbol{q}} + \boldsymbol{K'}_D \dot{\tilde{\boldsymbol{x}}} + \boldsymbol{K'}_P \tilde{\boldsymbol{x}} \right) \tag{5.6}$$

where $\tilde{\boldsymbol{x}} = \boldsymbol{x} - \boldsymbol{x}_d$ represents the Cartesian error with respect to the desired pose $\boldsymbol{x}_d(t) = \varphi(l(t))$. The elastic force $\boldsymbol{f_{el}} = \boldsymbol{K'}_P \tilde{\boldsymbol{x}}$ is generally defined by considering different expressions along the longitudinal and orthogonal directions to the curve to ensure precise tracking of the virtual mass position while allowing flexibility in deviations [53], [86].

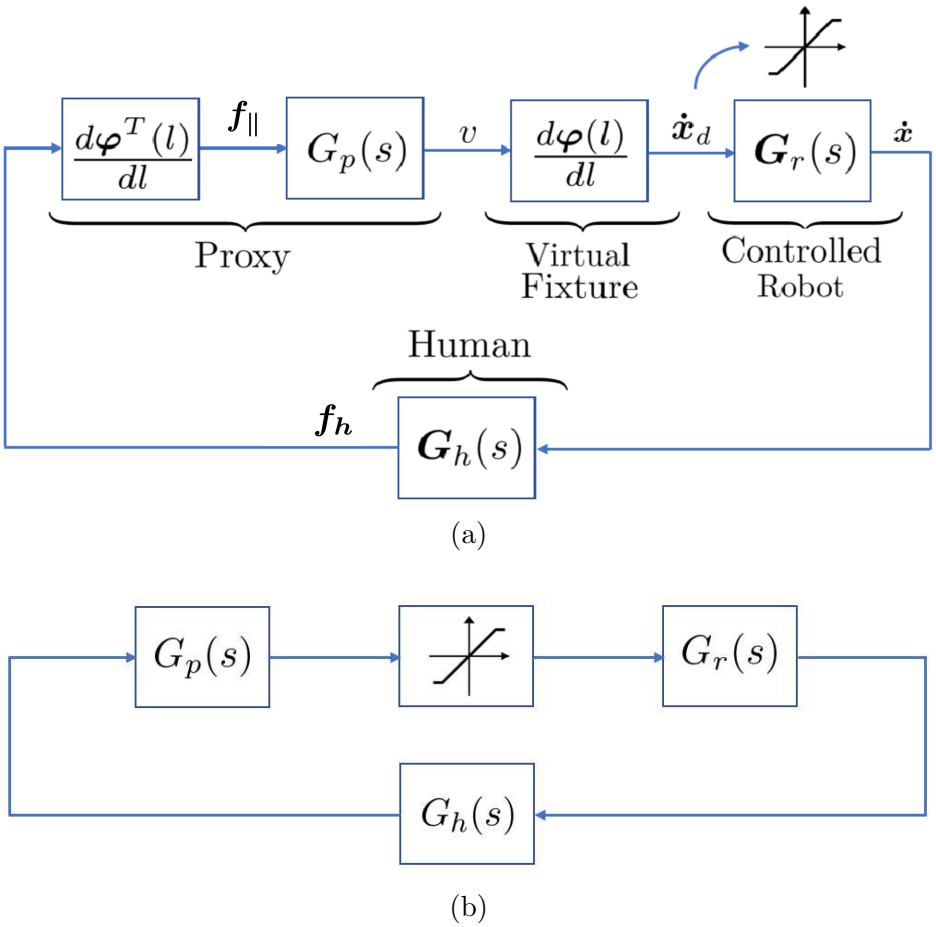

Figure 5.3: (a) Linearized block scheme of the proxy-based pHRI framework enhanced by virtual fixture of Fig. 5.1. (b) Simplified scalar representation used for stability analysis.

Since the focus of this work concerns stability under perturbed conditions (e.g., non-idealities), a linear analysis based on the Nyquist plot has been adopted. To this end, a linearized model of the controlled robot and the virtual fixture is derived. The resulting scheme is depicted in Fig. 5.3(a).

With the objective of studying the influence of the proxy parameters on the loop stability, the overall model is further reduced to the scalar case shown in Fig. 5.3(b). Here, $G_r(s)$ and $G_h(s)$ denote the dynamics of the robot and the human projected onto the path constraint. A saturation function is inserted into the loop to highlight the velocity limits of the actuation system (see Fig. 5.4).

The transfer function $G_r(s)$ is obtained by considering a one-DOF robot with an elastic joint, endowed with an inverse dynamics position controller. According to [98], the transfer function between the input torque τ_m and position x_m of the

link actuator is:

$$G_m(s) = \frac{X_m(s)}{T_m(s)} = \frac{J_{lr}s^2 + D_{el}s + K_{el}}{s[a_1 s^3 + a_2 s^2 + a_3 s + d]}, \tag{5.7}$$

where $a_1 = J_{lr}J_m$, $a_2 = J_{lr}D_m + J_t D_{el}$, $a_3 = J_t K_{el} + D_m D_{el}$ and $a_4 = D_m K_{el}$. $J_t = J_{lr} + J_m$ is the total inertia, J_{lr} is the link inertia reduced by n^2, and J_m is the motor inertia. Parameters D_m and D_{el} are the damping coefficients of the motor and the elastic transmission, respectively, and K_{el} is the transmission stiffness.

Assuming the position sensor to be located on the actuator, as typically done in industrial robots, the inverse dynamics control [84] $\boldsymbol{\tau}_m = \boldsymbol{J}_t(\ddot{\boldsymbol{x}}_d + \boldsymbol{K}_D\dot{\tilde{\boldsymbol{x}}} + \boldsymbol{K}_P\tilde{\boldsymbol{x}})$, where $\tilde{\boldsymbol{x}} = \boldsymbol{x}_d - \boldsymbol{x}_m$, can be applied to model (5.7), leading to the following transfer function $G_c(s)$ between the actuator speed $\dot{\boldsymbol{x}}_m$ and the reference speed $\dot{\boldsymbol{x}}_d$:

$$G_c(s) = \frac{\dot{X}_m(s)}{\dot{X}_d(s)} = \frac{b'_1 s^4 + b'_2 s^3 + b'_3 s^2 + b'_4 s + b'_5}{a'_1 s^4 + a'_2 s^3 + a'_3 s^2 + a'_4 s + a'_5}, \tag{5.8}$$

where the coefficients of $G_c(s)$ are defined in the appendix. The actuator and robot velocities, $\dot{\boldsymbol{x}}_m$ and $\dot{\boldsymbol{x}}$, are related by:

$$G_{mr}(s) = \frac{\dot{X}(s)}{\dot{X}_m(s)} = \frac{D_{el}s + K_{el}}{n(J_{lr}s^2 + D_{el}s + K_{el})}. \tag{5.9}$$

Finally, from (5.8) and (5.9), the transfer function $G_r(s)$ of the controlled robot can be derived:

$$G_r(s) = \frac{\dot{X}(s)}{\dot{X}_d(s)} = G_c(s)G_{mr}(s). \tag{5.10}$$

5.3 Stability Analysis of the pHRI Framework

Using (5.2), (5.3), (5.8) and (5.9), the loop gain function $G_l(s) = G_h(s)G_p(s)G_r(s)$ of the scheme of Fig. 5.3(b) can be found:

$$G_l(s) = \frac{\beta_1 s^6 + \beta_2 s^5 + \beta_3 s^4 + \beta_4 s^3 + \beta_5 s^2 + \beta_6 s + \beta_7}{s(\alpha_1 s^7 + \alpha_2 s^6 + \alpha_3 s^5 + \alpha_4 s^4 + \alpha_5 s^3 + \alpha_6 s^2 + \alpha_7 s + \alpha_8)},$$

where the coefficients of $G_l(s)$ are defined in the appendix.

The qualitative Nyquist diagram of function $G_l(s)$ is reported in Fig. 5.5(a), showing that the system is always asymptotically stable by using the Nyquist criterion, as no intersection with the negative real semiaxis occurs. However,

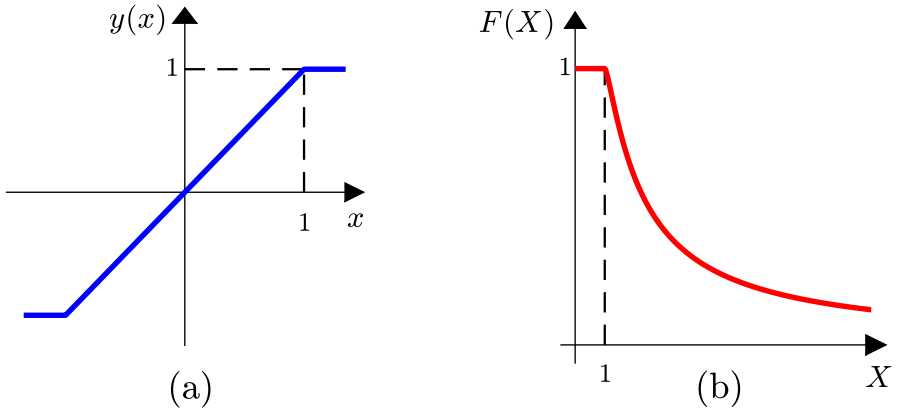

Figure 5.4: Representation of the saturation nonlinearity (a) and of the corresponding describing function (b).

a more realistic representation of the loop gain function includes two critical nonidealities:

1. The **system delays** (t_0), such as the discretization delay and the delay due to the finite bandwidth of the position control [90].

2. The **velocity saturation** of the actuators shown in the loop of Fig. 5.3(b) [99].

Letting t_0 represent the overall delay affecting the system, the resulting loop gain function $G_{l0}(s)$ is given by:

$$G_{l0}(s) = G_l(s)\, e^{-t_0\, s}. \tag{5.11}$$

Because of the delay t_0, the qualitative Nyquist plot of the loop gain function $G_l(s)$ shown in Fig. 5.5(a) deforms as shown in Fig. 5.5(b).

5.3.1 Describing Function Method

To analyze the effect of saturation (nonlinearity) in the presence of delay, the Describing Function method is used. The characteristic of the saturation nonlinearity $y(x)$ is shown in Fig. 5.4(a). When the saturation is subject to a sinusoidal excitation $x = X \sin(\omega t)$, its response is given by its describing function $F(X) = \frac{Y_1(X)}{X}\, e^{j\varphi_1(X)}$ [99] (shown in Fig. 5.4(b)), where $Y_1(X)$ and $\varphi_1(X)$ are the amplitude and the phase shift of the approximated sinusoidal signal.

According to extended Nyquist stability theory, a persistent oscillation (limit

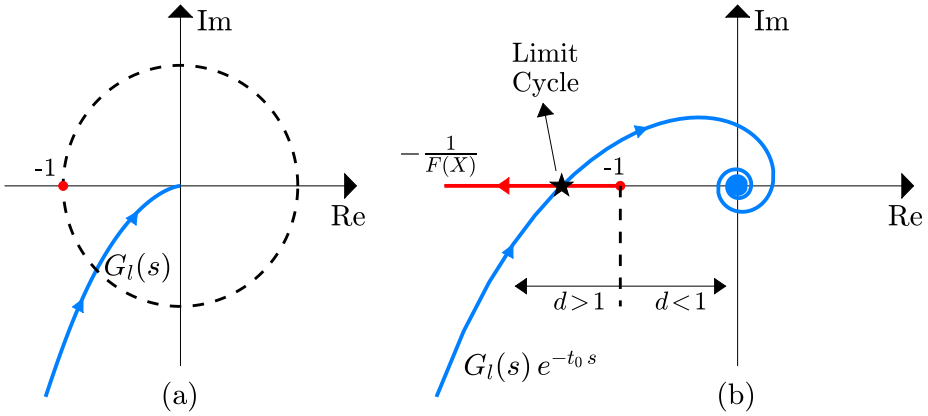

Figure 5.5: Qualitative Nyquist plot of the loop gain function $G_l(s)$, which includes the human, the proxy and the controlled robot, without considering the delay t_0 affecting the system (a) and considering it (b).

cycle) occurs if there is a solution to the self-sustaining equation:

$$F(X)G_{l0}(s) = -1 \quad \Rightarrow \quad G_{l0}(s) = -\frac{1}{F(X)} \tag{5.12}$$

Graphically, this corresponds to the intersection between the Nyquist plot of $G_{l0}(s)$ and the locus of points $-1/F(X)$ (which lies on the negative real axis) [99].

Fig. 5.5(b) shows that the combined effect of the delay t_0 and a sufficiently large modulus of the loop gain function $G_{l0}(s)$ likely causes the existence of a limit cycle in the pHRI framework. The intersection of the Nyquist plot of $G_{l0}(s)$ with the negative real semi-axis occurs at point $1/M_a$, indicated by the star in Fig. 5.5(b), where M_a is the gain margin of the system expressed in a linear scale. Therefore, the following distance d can be defined, quantifying the distance from the critical point -1 in Fig. 5.5(b):

$$d = \frac{1}{M_a}, \quad \begin{cases} d>1 \;\rightarrow\; \text{limit cycle}, \\ d<1 \;\rightarrow\; \text{no limit cycle}. \end{cases} \tag{5.13}$$

From (5.13), it follows that a persistent oscillation occurs if $d > 1$, namely if there is an intersection between the inverse $-1/F(X)$ of the describing function $F(X)$ and the Nyquist plot of $G_{l0}(s)$. This theoretically explains the vibrations observed experimentally when admittance parameters (m, b) are too low.

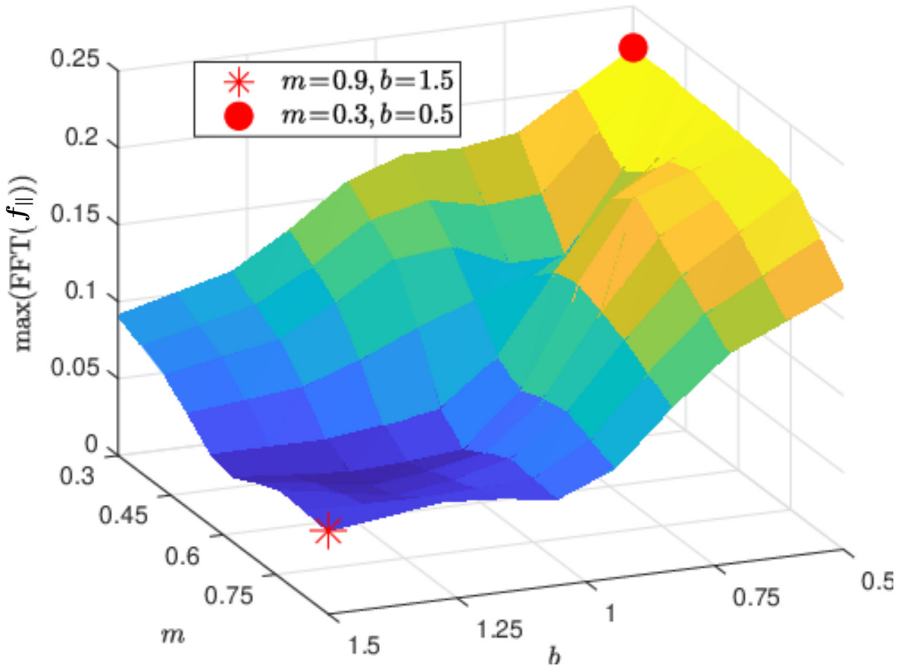

Figure 5.6: Spectral analysis of the tangential human force $f_{\parallel}$. The peak value $P_k = \max(\text{FFT}(f_{\parallel}))$ of the high frequency components of $\text{FFT}(f_{\parallel})$ is shown as a function of the proxy parameters m and b.

5.3.2 Experimental Verification

The existence of a persistent oscillation when m and b are sufficiently low has been verified experimentally through the proposed setup described in Sec. 5.2. The trajectory of Fig. 5.2(b) has been executed for $m \in [0.3, 0.9]$ kg and $b \in [0.5, 1.5]$ Ns/m. For each execution, the tangential component $f_{\parallel}$ of the human force has been acquired. This component is analyzed because of its influence in the proxy dynamics (5.1), directly affecting the evolution of the robot position.

Considering that the human arm bandwidth in voluntary motions is typically below 2 Hz [91], a Fast-Fourier Transform (FFT) has been applied to all acquisitions of $f_{\parallel}$ beyond that frequency treshold. The peak value of the high frequency (i.e. > 2 Hz) spectral components of $f_{\parallel}$ is reported in Fig. 5.6, showing that the oscillations intensity decreases as m and, mainly, b increase.

Furthermore, Fig. 5.7 shows the amplitude spectra and time behavior of $f_{\parallel}$ in two distinct cases. In the case with low parameters ($m = 0.3, b = 0.5$), the presence of a limit cycle $f_{\parallel}(t) = X_{cl} \sin(2\pi f_{cl} t)$ is clearly visible, at a frequency $f_{cl} \simeq 30$ Hz. The proposed analysis using the describing function method allows to provide a clear justification on why the proxy-based pHRI framework is affected by oscillatory behaviors.

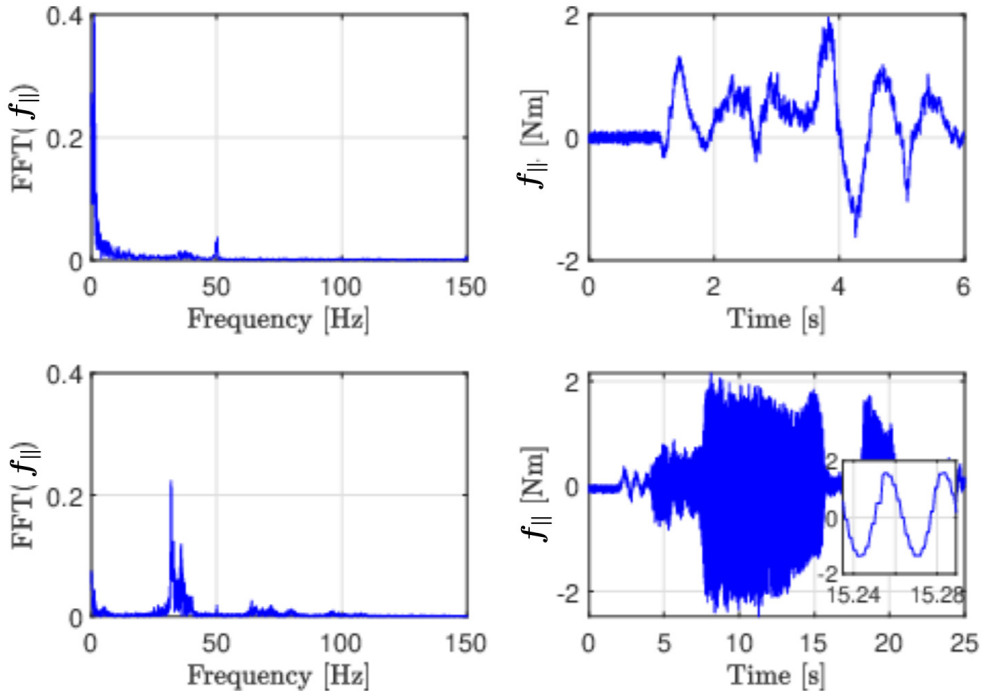

Figure 5.7: Amplitude spectrum (left) and time-plot (right) of the tangential human force $f_\parallel$. Top row: $m = 0.9$ and $b = 1.5$ (no oscillation). Bottom row: $m = 0.3$ and $b = 0.5$ (oscillation occurring). (e): Zoom-in of subplot (d).

5.4 Sensitivity Analysis to Admittance Parameters Variation

Consider the Nyquist diagram of the loop gain function $G_{l0}(s)$ in (5.11) shown in Fig. 5.8. This represents the boundary condition for the presence of a limit cycle. It is widely known [91] that larger values of the human stiffness K_h and/or smaller values of the admittance parameters m, b cause instability of the pHRI framework. This is consistent with the structure of $G_{l0}(s)$, suggesting that larger values of K_h increase the modulus of the loop gain, while larger values of m and b reduce it. While we have no direct control on K_h, the admittance parameters m and b can be adapted to prevent undesired oscillatory phenomena.

However, the literature review shows no unified consensus on the best adaptation approach. Therefore, we propose a sensitivity analysis to determine which of the three most commonly used approaches (adapting m, adapting b, or both) has the strongest impact on stability.

The sensitivity functions S_b^d, S_m^d, S_r^d of the distance d with respect to variations of the admittance parameters m, b, and of the distance $r = \sqrt{m^2 + b^2}$ (constant

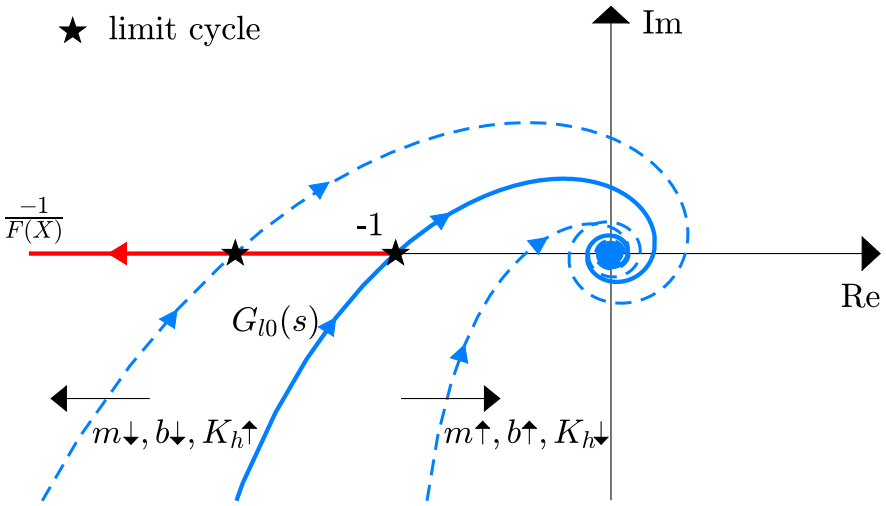

Figure 5.8: Loop gain function: qualitative Nyquist plot as a function of the admittance parameters and human stiffness.

Table 5.1: Sensitivity analysis: robotic system parameters.

J_l=0.66 km m^2, K_{el}=100 Nm/rad, D_{el}=0.01 Nm s/rad, n=50,
J_m=0.10 km m^2, D_m=0.11 Nm s/rad, K_h=150 N/m, b_h=0.68 N s/m

ratio m/b) are defined as follows [101]:

$$S_b^d = \frac{\Delta d/d_0}{\Delta b/b_0}, \quad S_m^d = \frac{\Delta d/d_0}{\Delta m/m_0}, \quad S_r^d = \frac{\Delta d/d_0}{\Delta r/r_0}, \tag{5.14}$$

where Δd is the variation from the nominal value d_0. The three sensitivity functions are shown in Fig. 5.9. As expected, positive parameter variations lead to a stable behavior. Interestingly, the maximum variation of Δd occurs when b is modified.

From an experimental point of view, the existence of a limit cycle can be detected through the peak value P_k of the high frequency spectral components of FFT($f_\parallel$). The experimental sensitivity functions $S_b^{P_k}$, $S_m^{P_k}$, $S_r^{P_k}$ are defined analogously:

$$S_b^{P_k} = \frac{\Delta P_k/P_{k0}}{\Delta b/b_0}, \quad S_m^{P_k} = \frac{\Delta P_k/P_{k0}}{\Delta m/m_0}, \quad S_r^{P_k} = \frac{\Delta P_k/P_{k0}}{\Delta r/r_0}. \tag{5.15}$$

Assuming typical parameters from Table 5.1 and nominal admittance values $m_0 = 0.6$ kg and $b_0 = 1$ Ns/m, the results are compared.

Fig. 5.10(a) shows that $S_b^{P_k}$ is the highest sensitivity, in agreement with the

Remark: The sensitivity analysis of the distance d in (5.13) with respect to the admittance parameters indicates the effectiveness of these parameters in preventing the system from exhibiting a limit cycle.

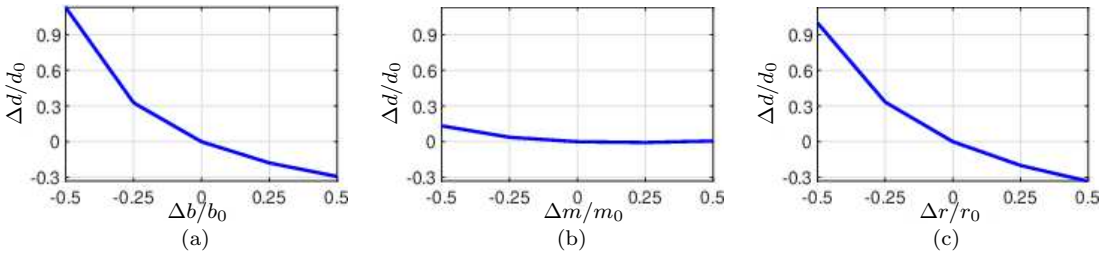

Figure 5.9: Sensitivity analysis as described in Remark: sensitivity functions S_b^d (a), S_m^d (b) and S_r^d (c) in (5.14).

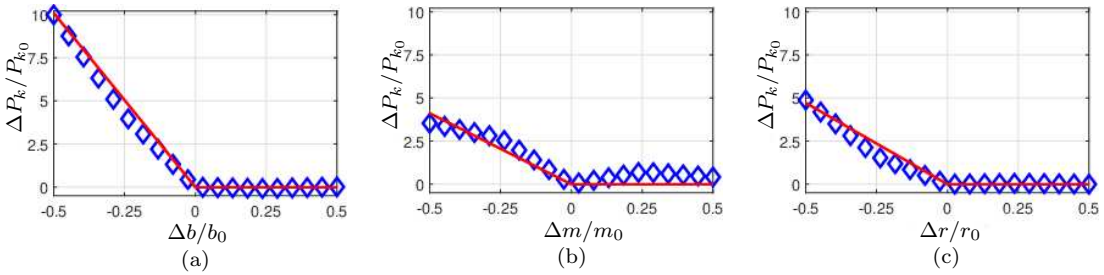

Figure 5.10: Experimental sensitivity analysis: sensitivity functions $S_b^{P_k}$ (a), $S_m^{P_k}$ (b) and $S_r^{P_k}$ (c) in (5.15).

theoretical sensitivity S_b^d in Fig. 5.9(a). This confirms that the damping parameter b is the one mainly influencing the pHRI stability. Conversely, m is the least influencing parameter (Fig. 5.10(b)). Finally, increasing both parameters simultaneously provides intermediate performance.

5.5 Parameter Adaptation for Transparency

Based on the sensitivity analysis presented in the previous section, an adaptation strategy for the admittance parameters is proposed. The goal is to maximize transparency in pHRI while ensuring stability under all conditions. In human-robot collaborative tasks, the user effort is strongly influenced by the admittance parameters [102], which effectively shape the perceived interaction dynamics.

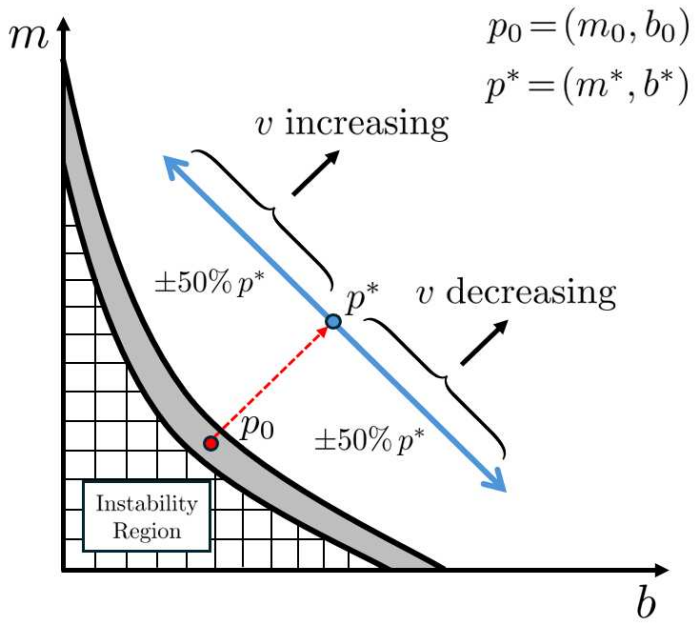

Figure 5.11: Adaptation strategy for the admittance parameters to maximize transparency within the stability region. The red area indicates the instability region, while the blue arrow shows the proposed parameter variation logic.

5.5.1 Transparency vs. Stability Trade-off

Transparency in pHRI refers to the system's ability to minimize the user's perception of resistive forces during movement, caused, e.g., by real or virtual inertia and friction. In physical control applications, such as robotic rehabilitation, teleoperation, or robot-assisted surgery, a transparent robot allows the user to perform smooth and natural movements without perceiving artificial constraints other than the virtual fixture. In the surgical domain, achieving high transparency is particularly critical for two reasons: first, to significantly reduce the physical effort and fatigue of the surgeon during prolonged procedures; and second, to maintain the natural haptic perception of the tool-tissue interaction, ensuring that the robot's inherent bulkiness does not mask delicate physiological feedback.

Transparency can be quantitatively evaluated by measuring the average force exerted by the user while performing a task:

$$\bar{f}_{\parallel} = \text{avg}(|f_{\parallel}|), \tag{5.16}$$

where a lower applied force $\bar{f}_{\parallel}$ indicates greater system transparency (i.e., minimal resistance imposed by the robot).

Generally, maintaining low values for the parameters m and b reduces the required user effort. However, as shown in Sec. 5.4, this condition is highly

detrimental to system stability. Conversely, increasing these parameters improves stability but degrades transparency, increasing the physical effort required from the user.

5.5.2 Proposed Adaptation Strategy

To resolve this conflict, a variable adaptation law is proposed as a function of the proxy velocity v. Letting v_0 be the nominal velocity for the task (e.g., the maximum expected velocity), the admittance parameters are varied according to the following logic, visualized in Fig. 5.11:

$$\begin{aligned} m(v) &= m_{min} + (m_{max} - m_{min})\frac{\text{sat}(|v|)}{v_0}, \\ b(v) &= b_{max} + (b_{min} - b_{max})\frac{\text{sat}(|v|)}{v_0}, \end{aligned} \tag{5.17}$$

where $\text{sat}(\cdot)$ is a saturation function limiting the output to the range $[0, v_0]$. This mechanism linearly changes the physical parameters from (m_{min}, b_{max}) to (m_{max}, b_{min}) as the velocity $|v|$ increases.

The rationale behind this strategy is based on physical considerations regarding the proxy dynamics (5.1):

- **At low velocities (acceleration phase):** The inertial term $m\dot{v}$ dominates. Therefore, m is kept at its minimum value m_{min} to reduce the effort required to accelerate the proxy. Simultaneously, b is kept at its maximum b_{max} to ensure static stability [17].
- **At high velocities (cruising phase):** The acceleration is negligible, and the user effort is dominated by the viscous friction term bv. Therefore, b is reduced to b_{min} to favor fluid movement. Simultaneously, m is increased to m_{max} to maintain a sufficient stability margin against oscillations [103].

This approach allows for a lower level of human force while guaranteeing stability without requiring complex feedback actions based on oscillation detection.

5.5.3 Optimization and Experimental Validation

To guarantee strong stability properties, the central operating point around which the parameters vary must be selected within the stable region (blue area in Fig. 5.11), moving away from the nominal limit point $p^0 = (m_0, b_0)$. However,

this shift typically increases user effort. To ensure that the proposed adaptation strategy restores the transparency levels of the nominal case, the following optimization problem is defined:

Optimization Problem 1. *Let $\bar{f}_{\|_v}$ be the user effort when the admittance parameters are varied as in Fig. 5.11 around a generic point p. The objective is to find the optimal value p^* of point $p = (m, b)$, around which the admittance parameters can be varied using (5.17), such that:*

$$\min_p J(p), \qquad \text{where} \qquad J(p) = |\bar{f}_{\|_v} - \bar{f}^0_{\|}|$$

subject to the constraints:

$$m_{min} = 0.5\, m, \quad m_{max} = 1.5\, m, \quad b_{min} = 0.5\, b, \quad b_{max} = 1.5\, b.$$

Based on this optimization logic, the central operating point $p^* = (m_*, b_*)$ has been selected to be more conservative than the nominal limit point p^0. Specifically, we chose $p^* = 1.5\, p^0$. The ranges are then defined as:

$$m_{min} = 0.5\, m_*, \quad m_{max} = 1.5\, m_*, \quad b_{min} = 0.5\, b_*, \quad b_{max} = 1.5\, b_*.$$

The effectiveness of this strategy was evaluated by comparing the user effort required in three cases:

1. **Nominal Case (p^0):** Parameters fixed at the edge of instability ($m_0 = 0.6$ kg, $b_0 = 1$ Ns/m). This represents the theoretical minimum effort $\bar{f}^0_{\|}$ achievable with fixed parameters before instability.

2. **Conservative Case (p^*):** Parameters fixed at a safe operating point ($p^* = 1.5p^0$).

3. **Adaptive Case (p^*_v):** Parameters varying according to (5.17) around the safe point p^*.

The simulation results reported in Table 5.2 show that $\bar{f}^*_{\|_v} \simeq \bar{f}^0_{\|}$. This means the adaptive strategy allows the user to experience the same low effort as the "edge-of-instability" case (p^0), but operating within a fully safe region (centered at p^*). Conversely, keeping the parameters fixed at the safe point p^* would result in a significantly higher effort (0.53 N vs 0.35 N).

Table 5.2: Simulative results of the admittance parameters optimization for maximizing transparency.

	Nominal (p^0)	**Conservative** (p^*)	**Adaptive** (p_v^*)
	(m_0, b_0)	$1.5\,p^0$ (fixed)	$1.5\,p^0$ (varying)
$\bar{f}_{\parallel}$ [N]	**0.35**	0.53	**0.34**

Table 5.3: Experimental results of the transparency optimization applied to the real setup.

	Nominal (p^0)	**Conservative** (p^*)	**Adaptive** (p_v^*)
	(m_0, b_0)	$1.5\,p^0$ (fixed)	$1.5\,p^0$ (varying)
$\bar{f}_{\parallel}$ [N]	**0.28**	0.38	**0.28**

These findings were validated experimentally using the setup described in Sec. 5.2. The results, summarized in Table 5.3, confirm the simulation trend.

In the experimental case, fixing the parameters at the safe point p^* increased the user effort by approximately 26% compared to the nominal case. However, by activating the proposed adaptive logic (5.17), the user effort returned to the nominal level ($\bar{f}^*_{\parallel_v} = 0.28$ N), demonstrating that it is possible to combine the safety of conservative parameters with the transparency of aggressive tuning.

5.6 Discussion

This chapter has addressed the stability, sensitivity, and transparency analyses in pHRI using variable admittance control. A distinguishing feature of this study, compared to the majority of related works focusing on free co-manipulation, is the specific consideration of pHRI enhanced by Virtual Fixture (VF).

The conducted stability analysis explicitly included nonlinear effects, such as system delays and actuator saturation. This approach provided a deep understanding of the nature of undesired oscillations, highlighting that the coupling between delay and saturation is the primary cause of the unstable behaviors observed in experimental settings.

While the proposed scalar analysis provides a clear understanding of the fundamental instability mechanisms, it is important to acknowledge the limitations

introduced by reducing the 7-DoF redundant robot to a simplified 1-DoF scalar model. In a multi-DoF redundant manipulator, Cartesian motions are inherently subject to configuration-dependent inertia and cross-axis dynamic coupling. The 1-DoF assumption considers the dynamics projected strictly along the tangential path, neglecting the off-diagonal terms of the Cartesian inertia matrix. In reality, interaction forces can induce coupled accelerations in orthogonal directions. Furthermore, the robot's kinematic redundancy allows for internal null-space motions that dynamically alter the effective inertia perceived at the end-effector. These configuration-dependent variations and inertial couplings could introduce unmodeled high-frequency dynamics or dynamically shift the stability margins identified in the scalar Nyquist analysis, potentially requiring more conservative tuning of the admittance parameters in specific regions of the workspace.

Furthermore, addressing the lack of consensus in the literature regarding the most effective parameter adaptation technique, a sensitivity analysis was performed. This analysis allowed for the discrimination of the admittance parameter with the greatest influence on pHRI stability, with simulative results fully confirmed by experimental validation.

Finally, to optimize the trade-off between stability and transparency, an optimization problem equipped with a novel admittance parameter adaptation technique was proposed. The objective was to maximize transparency—minimizing user effort—while maintaining stability. The effectiveness of this approach was verified through both simulation and experimental results, demonstrating a significant improvement in the interaction experience.

Chapter 6

Optimizing Design and Control Methods for Upper-Limb Rehabilitation using Collaborative Robots

6.1 Introduction

In recent years, the integration of robotic devices into post-operative rehabilitation protocols has gained significant traction, driven by the need to provide high-intensity, repetitive training while alleviating the physical burden on therapists [104]. These robotic systems are generally categorized into two main families: exoskeletons and end-effector devices.

Exoskeletons, such as ARMIN [105], Rupert [106], and NESM [107], are grounded on the user's anthropometric structure. They offer the advantage of controlling each joint of the limb independently, ensuring high repeatability of the movement. However, their widespread adoption is often hindered by their mechanical complexity, the difficulty in aligning the robot's joints with the human's physiological axes, and limited adaptability to different patient sizes or exercise routines.

Conversely, end-effector devices—exemplified by systems like MIT-MANUS [108], GENTLE/S [109], REHAROB [110], and others [111], [112]—interact with the patient only at the distal part of the limb (e.g., the hand or wrist). While they offer less direct control over proximal joints, they provide significant advantages in terms of simplicity, cost-effectiveness, and flexibility. In occupational therapy contexts, these manipulators can guide the patient's limb along predetermined paths, effectively replicating Activities of Daily Living (ADL) [113], [114]. Fur-

thermore, they allow for the definition of free-space exercises and the adjustment of the effort level required, enabling the therapy to adapt to the patient's recovery progress [115].

6.1.1 The Role of Collaborative Robots

This chapter focuses on a specific subset of end-effector solutions based on commercial cobot. The use of general-purpose cobot, such as the Franka Emika Panda used in this work, offers a streamlined path to clinical implementation compared to custom-built hardware. cobot are inherently designed for safe pHRI and are optimized from an engineering perspective [116]. However, integrating commercial collaborative robots (cobots) into rehabilitation poses specific challenges. Their kinematic architecture is designed for industrial or service tasks rather than biomechanical compatibility, and their payload capacity is often limited compared to the forces exerted during spastic movements or weight-bearing exercises. Consequently, a systematic design methodology is required to optimize the robot's pose relative to the rehabilitation task to maximize performance [117].

6.1.2 Control Challenges: Guidance and Adaptability

Beyond the mechanical setup, the core challenge lies in the control architecture. The interaction must be safe, intuitive, and capable of modulating assistance—ranging from passive motion (robot does all the work) to active participation (patient drives the motion). Standard industrial control modes are ill-suited for this dynamic responsiveness. To address this, impedance and admittance control strategies have become the standard for shaping the dynamic behavior of the robot [17], [83], [118].

A key concept in this domain is the VF [3], [4]. A Virtual Fixture (VF) constrains the user's motion along a desired path (Guidance Virtual Fixture (GVF)) or prevents entry into forbidden regions (Forbidden Region Virtual Fixture (FRVF)). In rehabilitation, GVFs are particularly valuable as they allow the patient to move along a therapeutic trajectory without enforcing a strict timing law, unlike traditional trajectory tracking [119]. This approach resolves the limitations of time-dependent trajectory planning, which forces the patient to follow a specific speed profile regardless of their functional ability [51].

Implementing GVFs often involves finding the closest point on the path to the end-effector position [24], [120], [121], a process that can be computationally expensive and prone to singularities [122]. An alternative, which is adopted in

this work, relies on a proxy-based approach [123], where a virtual mass interacts with the user and pulls the robot along the path.

6.1.3 Task Definition via Learning by Demonstration

To make the system accessible to therapists without programming skills, the definition of the rehabilitation task must be intuitive. This is achieved through *Learning by Demonstration (LbD)* [6], [124]. The therapist physically guides the robot to perform the exercise, and the system records and encodes the trajectory. While Dynamic Movement Primitives (DMPs) are a popular choice for encoding such motions [50], this work employs constrained smoothing B-splines [68], [125], which offer a balance between approximation accuracy and trajectory smoothness suitable for geometric path following. Specifically, the B-spline optimization is constrained by a strict tolerance parameter that upper-bounds the maximum geometric deviation from the filtered demonstration. As evaluated in the earlier methodological analysis reported in Chapter 3, this approach guarantees an approximation accuracy in the sub-millimeter to low-millimeter range (e.g., RMSE < 1 mm), strictly preserving the user's geometric intent while ensuring the $\mathcal{C}^2$ continuity mathematically required for stable haptic interaction, a fundamental prerequisite for high-precision extensions, such as robot-assisted surgery.

6.1.4 Contributions of this Chapter

Building upon the preliminary concepts introduced in [78], [117], this chapter presents a comprehensive framework for cobot-assisted upper-limb rehabilitation. The specific contributions are:

1. **Optimization-Based Design Methodology:** A procedure to identify the optimal relative pose between the robot and the rehabilitation trajectory. Unlike standard manipulability indices [126], this method utilizes a specific *payload index* (P_z) to maximize the robot's capacity to support vertical loads (e.g., the weight of the patient's arm) [127].

2. **Novel Control Architecture:** An Hybrid Impedance Control (HIC) scheme that spatially decouples the interaction dynamics to combine the benefits of both admittance and impedance paradigms:

    - *Tangential Admittance:* The task progression along the path is governed by the dynamics of a virtual proxy constrained to the curve.

This admittance-based interaction allows the user to dictate the execution speed via force application, effectively decoupling geometric constraints from the temporal law [70].

- *Orthogonal Impedance:* The confinement within the safe region is achieved via an impedance-based approach. A non-linear elastic force field is superimposed onto the robot's natural dynamics to generate haptic feedback that penalizes deviations from the path, providing tunable "soft" or "hard" constraints [112], [128].
- *Singularity-Free Guidance:* The resulting proxy-based mechanism ensures computationally efficient and singularity-free guidance, as the reference is generated by the physical evolution of the virtual mass rather than geometric projection.

3. **Adaptive Interaction Modes:** The system can seamlessly switch between:
   - *Passive Mode:* The robot supports the limb and guides the motion.
   - *Active Mode:* The robot provides resistance or transparency [7], [129].
   - *Assist-as-needed (AAN):* Virtual forces can be injected to help the patient only when necessary [130], [131].

Crucially, rigorous stability proofs for the coupled human-robot system are provided, addressing a gap often present in related literature where stability is assumed but not formally demonstrated. The following sections will detail the workspace optimization algorithm, the derivation of the control laws, and the experimental validation of the system in both technical benchmarks and simulated ADL tasks.

6.2 Related Works and Paper Contributions

The design of the proposed control architecture has been guided by an in-depth analysis of the literature, aiming to identify the functional and technical features that contribute to an effective and flexible rehabilitation system.

From a functional perspective, rehabilitation tools are categorized according to the level of assistance they provide [114], ranging from passive to active devices. This classification depends on whether the devices only offer resistive forces or can actively apply forces to the patient. It is important to note that, in general,

the terms "active" and "passive" refer to the behavior of the patient. Robotic devices enable the adjustment of the resistance experienced by the user during rehabilitation exercises and can incorporate an assist-as-needed (AAN) mechanism to help the patient complete the exercises [7], [112].

In the context of rehabilitative robots, *passive therapy* can be easily implemented because there is no need for feedback by the patient, whose limb is simply moved along predefined trajectories without the patient having to exert any effort. Accordingly, from a control perspective, this application involves simple trajectory tracking of a time-dependent trajectory, possibly with different stiffness gains along the free and constrained directions [119].

On the contrary, *active therapy* requires the robot end-effector to constrain the motion of the user's limb along specific directions while leaving movement free in other directions. In any case, it is the patient, possibly aided by the system, who must apply the force necessary to move the limb. In this scenario, the control must implement a so-called *GVF*, which does not depend on time but only on the geometric characteristics of the constraints [3], [4].

6.2.1 Approaches to Virtual Fixtures Implementation

Basically, guiding VFs can be implemented in two complementary ways:

1. The user interacts with the robot, which is subject to a force/velocity field that tends to maintain it on the desired path.

2. The user interacts with a virtual point, called *proxy*, that is constrained to move on the desired path, and then the robot, possibly connected through a virtual spring, tracks this point.

Both approaches have their pros and cons. Consider the scheme of Fig. 6.1, where a generic guiding VF is defined by the parametric curve $\boldsymbol{\varphi}(s)$.

According to the former technique, described e.g. in [24], [120], [121], it is necessary to compute at each time-stamp the value of parameter s that minimizes the distance between the curve $\boldsymbol{\varphi}(s)$ and the end-effector position $\boldsymbol{x}(t)$:

$$s^\star = \arg \min_{s \in [0,l]} \|\boldsymbol{x}(t) - \boldsymbol{\varphi}(s)\|. \tag{6.1}$$

The solution of (6.1) based on iterative methods can be computationally expensive, thus limiting the maximum sampling rate of the digital control implementing the VF, with repercussions on the stability of the system itself [18]. Furthermore,

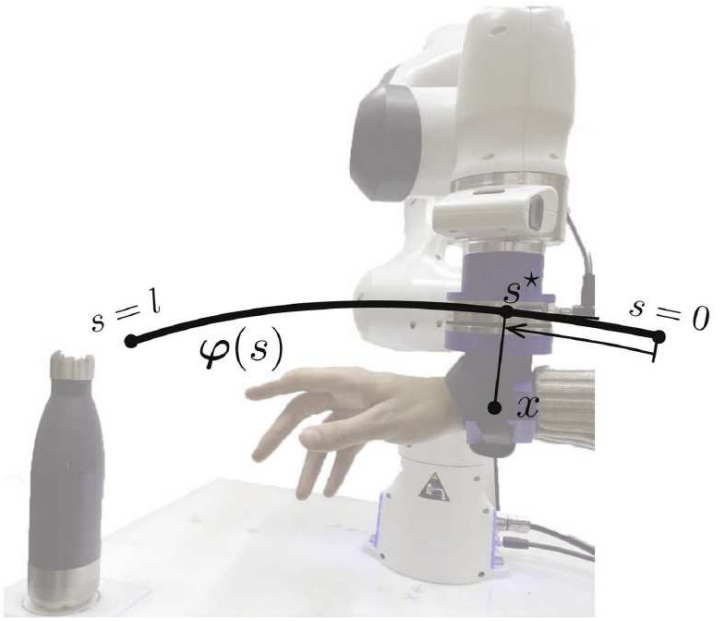

Figure 6.1: Guiding virtual fixture on a generic curve $\boldsymbol{\varphi}(s)$ parametrized by its arc-length, defining a rehabilitation task.

the search for the nearest point on the path may yield more than one solution [24]. For this reason, the approaches based on this type of solution are affected by *singularities* in the motion representation, that may require the imposition of geometric constraints on the reference curve, such as its curvature [122].

The latter method (proxy-based) is more efficient from a computational point of view and is not subject to singularity conditions due to the specific parameterization of the curve $\boldsymbol{\varphi}(s)$. However, it introduces into the system a new dynamics that may cause instability and unwanted effects, such as additional elasticities.

6.2.2 Comparison with State of the Art

Table 6.1 classifies some notable research works focused on the control of end-effector type rehabilitation robots according to key features identified in the literature analysis.

Many of the proposed control architectures possess most of the desirable characteristics that such a system must have, but not all of them. The goal of the proposed research is to integrate all these features into a single framework. The resulting solution is a Hybrid Impedance Control, which is a sort of an extension of a common Admittance Guidance Virtual Fixture, that transforms the system into a passive mechanical tool, which can be easily programmed by therapists through a Learning by Demonstration (LbD) approach. Additionally, our archi-

Table 6.1: Main features of the control architectures for end-effector type rehabilitation robots.

Ref.	**Interaction Modes**		**Curve Definition**		**Constraint Definition**		**Stability**	**Singularity**
	Active	Passive	Analytic	LbD	Soft	Hard	**Proved**	**Free**
[7]	✓	✓	✓		✓		✓	
[132]		✓	✓	✓	✓		✓	
[112]	✓		✓		✓			
[122]	✓	✓	✓		✓			
[6]		✓	✓			✓		✓
[131]		✓	✓		✓		✓	
[129]	✓	✓	✓	✓	✓			
Our	✓	✓	✓	✓	✓	✓	✓	✓

tecture facilitates *adaptive force application*, enabling the robot to assist or resist the patient as needed during the exercise.

Interestingly, due to the particular expression of the elastic function embedded in the admittance model, it is possible to separately define the restoring force level and the maximum deviation from the reference curve, effectively combining soft and hard constraints.

6.3 Robot-Trajectory Relative Pose Optimization

A systematic methodology for designing cobot-assisted rehabilitation solutions is proposed. Based on the physiotherapist's clinical recommendations, the layout of rehabilitation exercises can be optimized by selecting the appropriate cobot and end-effector, and subsequently optimizing the placement of motion trajectories within the robot's workspace.

Shifting the perspective from traditional design approaches, we aim to determine the robot pose that maximizes a specific design criterion for a given exercise type. In our previous work [117], the optimization of the robot pose was based on the classical *manipulability index*:

$$m(\boldsymbol{q}) = \sqrt{\det\big(\boldsymbol{J}(\boldsymbol{q})\boldsymbol{J}^T(\boldsymbol{q})\big)} \tag{6.2}$$

where $\boldsymbol{J}(\boldsymbol{q})$ denotes the Jacobian Matrix of the manipulator. Based on the index $m(\boldsymbol{q})$, the cobot workspace is divided into regions that guarantee a minimum manipulability value, identifying zones where the robot can exert forces in all Cartesian directions without inducing excessive joint torques.

However, for rehabilitation applications using commercial cobots, the primary limitation is often the payload capacity. In the early stages of rehabilitation, patients may lack the strength to support their own arm, meaning the robot must bear a significant portion of the weight. Consequently, the dominant force component acting on the cobot's end-effector is vertical (gravity). Therefore, a payload-specific index is preferred over the general manipulability index.

6.3.1 The Payload Index (P_z)

The proposed index evaluates the maximum net force the robot can exert along the vertical z-axis of the task space. Consider the Euler-Lagrange model of a robot manipulator interacting with a human:

$$\boldsymbol{M}(\boldsymbol{q})\ddot{\boldsymbol{q}} + \boldsymbol{C}(\boldsymbol{q}, \dot{\boldsymbol{q}})\dot{\boldsymbol{q}} + \boldsymbol{g}(\boldsymbol{q}) = \boldsymbol{\tau} + \boldsymbol{J}^T(\boldsymbol{q})\boldsymbol{f}_h \tag{6.3}$$

where $\boldsymbol{q} \in \mathbb{R}^n$ is the joint variable vector, $\boldsymbol{M}(\boldsymbol{q})$ is the inertia matrix, $\mathbf{C}(\boldsymbol{q}, \dot{\boldsymbol{q}})\dot{\boldsymbol{q}}$ represents Coriolis and centrifugal torques, $\mathbf{g}(\boldsymbol{q})$ is the gravitational torque vector, $\boldsymbol{\tau}$ is the actuator torque vector, and $\boldsymbol{\tau}_h = \boldsymbol{J}^T(\boldsymbol{q})\boldsymbol{f}_h$ are the joint torques resulting from the external wrench $\boldsymbol{f}_h$ applied by the patient.

In static conditions ($\ddot{\boldsymbol{q}} = \dot{\boldsymbol{q}} = 0$), assuming the force generated by the interaction is purely vertical ($\boldsymbol{f}_h = [0,\ 0,\ -f_z,\ 0,\ 0,\ 0]^T$), the actuator torques required for static balancing are:

$$\tau_i = \boldsymbol{J}_{3,i}(q) f_z + \boldsymbol{g}_i(q), \qquad i = 1, \ldots, n \tag{6.4}$$

where $\boldsymbol{J}_{3,i}(q)$ is the element $(3, i)$ of the Jacobian, and $\boldsymbol{g}_i(q)$ is the i-th component of the gravity vector. By imposing the actuation limits $|\tau_i| \leq \tau_{lim,i}$, the maximum sustainable vertical force f_z is derived as:

$$f_{z,\max} = \min_i \left\{ \frac{\tau_{lim,i} - |\boldsymbol{g}_i(q)|}{|\boldsymbol{J}_{3,i}(q)|} \right\}. \tag{6.5}$$

The force $F_{z,\max}$ defines the scalar *payload index* $P_z(\boldsymbol{x})$, which maps the robot's workspace capability. By discretizing the 3D workspace into points $\boldsymbol{x}_i$, and fixing the end-effector orientation $\bar{\boldsymbol{\gamma}}$, we can generate a map of the maximum sustainable vertical force:

$$P_z(\boldsymbol{x}_i): \quad \boldsymbol{p}_i = \begin{bmatrix} \boldsymbol{x}_i \\ \bar{\boldsymbol{\gamma}} \end{bmatrix} \quad \longrightarrow \quad \boldsymbol{q}_i \quad \longrightarrow \quad f_{z,\max_i}.$$

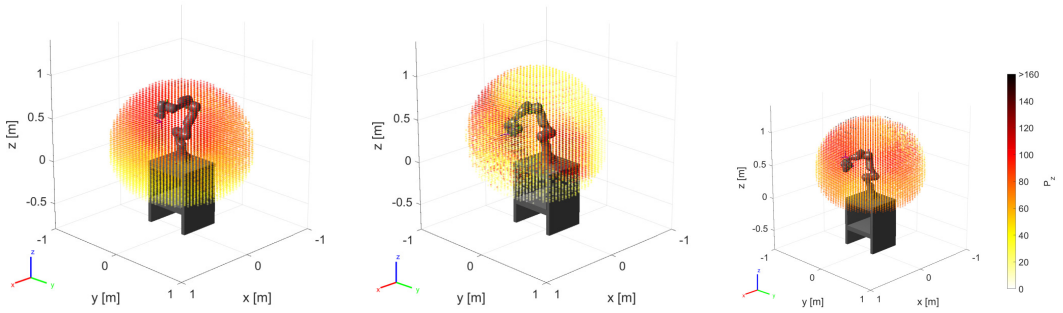

(a) (b) (c)

Figure 6.2: Workspace maps based on the index $P_z(\boldsymbol{x}_i)$ with fixed orientations: (a) Flange Down, (b) Flange Horizontal, and (c) Flange Up.

Figure 6.2 visualizes these payload maps for three different flange orientations: Down (a), Horizontal (b), and Up (c). The color scale highlights the significant variation in payload capability across the workspace, emphasizing the importance of optimal positioning.

While the current analysis evaluates the workspace for a standard floor-mounted configuration, it is worth noting that the index P_z is equally sensitive to the robot's base mounting orientation. As a theoretical extension, altering the gravity vector relative to the robot's base (e.g., via wall or tilted mounting) would fundamentally shift the payload distribution. Specifically, if the base is oriented such that the axes of the main pitch joints align with the gravity vector, the static gravitational torques $\mathbf{g}_i(\mathbf{q})$ acting on those specific joints are effectively nullified. According to Equation (6.5), setting $|\mathbf{g}_i(\mathbf{q})| = 0$ leaves the entire actuation margin $\tau_{lim,i}$ available to counteract the external wrench, thereby maximizing the sustainable vertical force $f_{z,\max}$. Exploring base-mounting optimizations based on this kinematic property represents a highly promising direction for tailoring custom rehabilitative robotic cells.

6.3.2 Optimization Procedure

The workspace optimization involves determining the optimal placement of the rehabilitation trajectory relative to the cobot's base frame. A trajectory is discretized into an ordered set of points $\boldsymbol{\varphi}_k$ $(k = 1, \ldots, n)$. For a given candidate position j of the trajectory in the workspace, a score π_j is assigned based on the minimum payload capacity along the path:

$$\pi_j = \min_k P_z(\boldsymbol{\varphi}_k). \tag{6.6}$$

The algorithm iteratively explores various locations by translating the trajectory in the xy-plane and rotating it around its geometric center. The optimal configuration is identified as the one that maximizes the minimum guaranteed payload:

$$\pi_{\text{opt}} = \max_j \{\pi_j\}. \tag{6.7}$$

Once the optimal layout is defined and the cobot is installed, the system is ready for clinical use. To ensure user-friendliness and customization, the specific exercises are then refined or redefined by the therapist using the LbD methodology described in the previous section, ensuring that the motion remains within the optimized high-payload region of the workspace.

6.4 Control Architecture for Human-Robot Interaction

A novel control architecture that mixes admittance control and guidance virtual fixtures is developed to constrain the motion of the cobot's end-effector along a 3D path specified by the therapist, without imposing a specific time law. In this way, it is the patient connected to the robot's end-effector who imposes the movement along the curve by applying forces with the rehabilitated limb.

As mentioned in the introduction, the basic idea relies on a virtual proxy [4], [123] affected by the force exchanged with the user. However, the proposed implementation introduces several novelties to adapt this concept specifically for rehabilitation, leveraging the methodological framework established in Chapter 3.

Let us assume that the reference path, denoted as $\boldsymbol{x_d}$, has been settled by the therapist using a Learning by Demonstration (LbD) procedure, and is defined by a parametric function:

$$\boldsymbol{x_d} = \boldsymbol{\varphi}(u). \tag{6.8}$$

Function $\boldsymbol{\varphi}(\cdot)$ represents any curve with a proper degree of continuity (at least $\mathcal{C}^1$). In the experiments, we consider cubic B-spline functions obtained by interpolating the points registered during the demonstration.

In standard kinesthetic teaching, the independent variable u is typically time ($u = t$). However, as discussed in Sec. 3.1, this dependency introduces distortions when the execution speed varies. Since the proposed rehabilitation application aims to enforce a prescribed geometric path without specifying execution speed,

an *arc-length parameterization* is adopted. This is achieved by processing the demonstrated trajectory with the Spatial Sampling Algorithm (SSA) detailed in Sec. 3.2, which ensures that the curve is parameterized by the curvilinear coordinate s rather than time. Mathematically, this corresponds to composing $\boldsymbol{\varphi}(u)$ with the function $u(s)$, obtained by inverting the arc-length integral. With a slight abuse of notation, we denote the resulting spatially-parameterized curve as $\boldsymbol{\varphi}(s)$.

A crucial property derived from the SSA (see Eq. 3.2 in Chapter 3) is that the tangent vector has unitary magnitude:

$$\|\boldsymbol{\varphi}'(s)\| = \left\| \frac{d\boldsymbol{\varphi}(s)}{ds} \right\| = 1. \tag{6.9}$$

This property is fundamental for the stability of the admittance control, as it ensures that the mapping from user force to motion along the curve is consistent and never vanishes (avoiding the stagnation phenomenon described in Sec. 3.4).

As shown in Fig. 6.3(a), a point-wise mass m is constrained to follow $\boldsymbol{\varphi}(s)$ and moves subject to the force applied by the user. Simultaneously, the cobot tracks the position of this mass. Fig. 6.3(b) depicts the overall block scheme. The Guidance Virtual Fixture computes the forward dynamics of the virtual mass based on the measured force $\hat{\boldsymbol{f}}_h$, providing the instantaneous reference position:

$$\boldsymbol{x}_d(t) = \boldsymbol{\varphi}(s(t)). \tag{6.10}$$

Given $\boldsymbol{x}_d(t)$, its derivatives can be analytically computed as:

$$\dot{\boldsymbol{x}}_d(t) = \boldsymbol{\varphi}'(s)\dot{s}(t) \tag{6.11}$$

$$\ddot{\boldsymbol{x}}_d(t) = \boldsymbol{\varphi}''(s)\dot{s}^2(t) + \boldsymbol{\varphi}'(s)\ddot{s}(t) \tag{6.12}$$

where $\boldsymbol{\varphi}'(s)$ and $\boldsymbol{\varphi}''(s)$ are the first and second derivatives with respect to the arc length.

6.4.1 Dynamic Equation of the Virtual Mass

The general architecture of the control framework was introduced in Chapter 4, where its structural soundness and passivity were rigorously proven using Lyapunov theory. However, while Chapter 4 outlined the theoretical basis for safety, it treated the dynamics of the system in broad terms. In this section, we explicitly detail the mathematical derivation of the scalar equation of motion, moving from

the general concept to the specific implementation used for the rehabilitation task.

The dynamic model of the point mass m is derived using Lagrange equations. Assuming the mass is constrained to the path $\boldsymbol{\varphi}(s)$ and not affected by gravity, the Lagrangian corresponds solely to the kinetic energy:

$$\mathcal{L} = \mathcal{K} = \frac{1}{2} m \dot{\boldsymbol{x}}_d^T \dot{\boldsymbol{x}}_d = \frac{1}{2} m \dot{s}^2, \tag{6.13}$$

where the simplification exploits the property $\|\boldsymbol{\varphi}'(s)\| = 1$ of the arc-length parameterization derived via the SSA.

By applying the Euler-Lagrange operator to (6.13), we obtain the specific scalar dynamics governing the task progression:

$$m\ddot{s} + b\dot{s} = f_{\parallel} \tag{6.14}$$

where $b\dot{s}$ represents the viscous friction—a crucial term for the dissipativity properties demonstrated in Chapter 4—and $f_{\parallel}$ is the tangential component of the user force $\hat{\boldsymbol{f}}_h$:

$$f_{\parallel} = \boldsymbol{\varphi}'(s)^T \cdot \hat{\boldsymbol{f}}_h. \tag{6.15}$$

Other force components orthogonal to the path are compensated by the virtual constraints. Note that if $m \approx 0$, Eq. (6.14) reduces to the standard admittance relationship $v \propto f$.

6.4.2 Cartesian Impedance Control of the Robot

Consider the dynamic model of the robot manipulator interacting with a human, described by the Euler-Lagrange formulation:

$$\boldsymbol{M}(\boldsymbol{q})\ddot{\boldsymbol{q}} + \boldsymbol{C}(\boldsymbol{q}, \dot{\boldsymbol{q}})\dot{\boldsymbol{q}} + \boldsymbol{g}(\boldsymbol{q}) = \boldsymbol{\tau} + \boldsymbol{J}^T(\boldsymbol{q})\boldsymbol{f}_h \tag{6.16}$$

where $\boldsymbol{M}(\boldsymbol{q})$ is the joint-space inertia matrix, $\boldsymbol{C}(\boldsymbol{q}, \dot{\boldsymbol{q}})\dot{\boldsymbol{q}}$ represents Coriolis and centrifugal effects, $\boldsymbol{g}(\boldsymbol{q})$ is the gravity vector, $\boldsymbol{\tau}$ is the control torque, and $\boldsymbol{J}^T(\boldsymbol{q})\boldsymbol{f}_h$ is the torque generated by the external force $\boldsymbol{f}_h$ applied by the user.

To shape the dynamic behavior of the robot, a Cartesian inverse dynamics control law is adopted:

$$\boldsymbol{\tau} = \boldsymbol{M}(\boldsymbol{q})\boldsymbol{y} + \boldsymbol{C}(\boldsymbol{q}, \dot{\boldsymbol{q}})\dot{\boldsymbol{q}} + \boldsymbol{g}(\boldsymbol{q}) \tag{6.17}$$

where the auxiliary control input $\boldsymbol{y}$ is designed to linearize the system in the operational space and impose the desired impedance behavior:

$$\boldsymbol{y} = \boldsymbol{J}^{-1}(\boldsymbol{q}) \left(\ddot{\boldsymbol{x}}_d - \dot{\boldsymbol{J}}(\boldsymbol{q})\dot{\boldsymbol{q}} + \boldsymbol{K}'_D \dot{\tilde{\boldsymbol{x}}} + \boldsymbol{f}'_{el}(\tilde{\boldsymbol{x}}) \right). \tag{6.18}$$

Here, $\tilde{\boldsymbol{x}} = \boldsymbol{x} - \boldsymbol{x}_d$ represents the Cartesian tracking error with respect to the desired pose $\boldsymbol{x}_d$ (provided by the proxy). Substituting (6.17) and (6.18) into (6.16) leads to the closed-loop dynamics:

$$\ddot{\tilde{\boldsymbol{x}}} + \boldsymbol{K}'_D \dot{\tilde{\boldsymbol{x}}} + \boldsymbol{f}'_{el}(\tilde{\boldsymbol{x}}) = \boldsymbol{M}_A^{-1}(\boldsymbol{q}) \boldsymbol{f}_h. \tag{6.19}$$

To recover the physical interpretation of a mechanical impedance, the gain matrices are scaled by the Cartesian inertia matrix $\boldsymbol{M}_A(\boldsymbol{q}) = \boldsymbol{J}^{-T}(\boldsymbol{q})\boldsymbol{M}(\boldsymbol{q})\boldsymbol{J}^{-1}(\boldsymbol{q})$:

$$\boldsymbol{K}'_D = \boldsymbol{M}_A^{-1}(\boldsymbol{q}) \boldsymbol{K}_D \tag{6.20}$$

$$\boldsymbol{f}'_{el}(\tilde{\boldsymbol{x}}) = \boldsymbol{M}_A^{-1}(\boldsymbol{q}) \boldsymbol{f}_{el}(\tilde{\boldsymbol{x}}) \tag{6.21}$$

Consequently, the impedance model of the robot in the Cartesian space is derived as:

$$\boldsymbol{M}_A(\boldsymbol{q}) \ddot{\tilde{\boldsymbol{x}}} + \boldsymbol{K}_D \dot{\tilde{\boldsymbol{x}}} + \boldsymbol{f}_{el}(\tilde{\boldsymbol{x}}) = \boldsymbol{f}_h. \tag{6.22}$$

In this equation, $\boldsymbol{K}_D > 0$ is the desired damping matrix, and $\boldsymbol{f}_{el}(\tilde{\boldsymbol{x}})$ is a generic elastic force. This force is obtained by differentiating a scalar potential function $U_{el}(\tilde{\boldsymbol{x}}) \geq 0$, such that $U_{el}(\tilde{\boldsymbol{x}}) = 0 \iff \tilde{\boldsymbol{x}} = 0$:

$$\boldsymbol{f}_{el}(\tilde{\boldsymbol{x}}) = \left(\frac{\partial U_{el}(\tilde{\boldsymbol{x}})}{\partial \tilde{\boldsymbol{x}}} \right)^T. \tag{6.23}$$

As highlighted in [133], the dynamics in (6.22) represent a passive mapping from the external force $\boldsymbol{f}_h$ to the velocity error $\dot{\tilde{\boldsymbol{x}}}$, ensuring the stability of the system in feedback interconnection with a passive environment (the human operator).

Finally, it is worth noting that the inclusion of the feedforward acceleration term $\ddot{\boldsymbol{x}}_d(t)$ in the auxiliary input (6.18) is crucial. It justifies the adoption of the second-order dynamics for the proxy in (6.14); without this term, the required acceleration $\ddot{s}(t)$ could theoretically lead to infinite values for the control variable, compromising the realizability of the virtual fixture.

6.4.3 Stability Analysis

The safety of the proposed rehabilitation system relies on the rigorous theoretical validation established in Chapter 4. While that chapter provided the formal proofs of asymptotic stability and passivity for the general control framework—including the management of redundancy and null-space dynamics (Sec. 4.5)—this section focuses on verifying that the specific control laws instantiated for the rehabilitation task adhere to those dissipative properties.

As illustrated in Fig. 6.3(b), the overall control scheme is composed of three interconnected subsystems: the Patient, the Admittance Guidance VF, and the Controlled Robot. The analysis rests on the fundamental assumption, discussed in Sec. 4.4, that humans behave in a passive manner during voluntary interaction or when holding a posture [134], [135]. Accordingly, the human operator defines a passive mapping from velocity ($\dot{\boldsymbol{x}}$) to force ($-\boldsymbol{f}_h$). Therefore, to ensure the stability of the coupled system, we must verify that the map from the user's force $\boldsymbol{f}_h$ to the robot's velocity $\dot{\boldsymbol{x}}$ is passive for the specific dynamics derived in equations (6.14) and (6.22).

To this end, we define the state vector $\boldsymbol{\xi} = [\dot{s},\, \tilde{\boldsymbol{x}},\, \dot{\tilde{\boldsymbol{x}}}]^T$ and construct a storage function $S_r(\boldsymbol{\xi})$ representing the total "virtual energy" of the rehabilitation system. This function combines the kinetic energy of the proxy, the inertia-weighted tracking error, and the potential energy of the virtual constraints defined in Sec. 6.4:

$$S_r(\boldsymbol{\xi}) = \frac{1}{2} m \dot{s}^2 + \frac{1}{2} \dot{\tilde{\boldsymbol{x}}}^T \boldsymbol{M}_A(\boldsymbol{q}) \dot{\tilde{\boldsymbol{x}}} + U_{el}(\tilde{\boldsymbol{x}}). \tag{6.24}$$

As demonstrated in the general proof (Sec. 4.3), this function serves as a valid Lyapunov candidate.

Taking the time derivative of $S_r(\boldsymbol{\xi})$ and exploiting the skew-symmetric property of the robot dynamics ($\dot{\boldsymbol{M}}_A - 2\boldsymbol{C}_A$), we obtain the power balance equation. By substituting the reference velocity $\dot{\boldsymbol{x}}_d = \boldsymbol{\varphi}'(s)\dot{s}$ and the error dynamics, the derivative simplifies to:

$$\dot{S}_r(\boldsymbol{\xi}) = -b\dot{s}^2 - \dot{\tilde{\boldsymbol{x}}}^T \boldsymbol{K}_D \dot{\tilde{\boldsymbol{x}}} + \dot{\boldsymbol{x}}^T \boldsymbol{f}_h. \tag{6.25}$$

Since the virtual friction coefficient b and the damping matrix $\boldsymbol{K}_D$ are strictly positive definite ($b > 0$, $\boldsymbol{K}_D > 0$), the first two terms are strictly non-positive, representing the power dissipated by the controller to enforce the virtual fixture and dampen the motion. Consequently, the dissipation inequality holds:

$$\dot{S}_r(\boldsymbol{\xi}) \leq \dot{\boldsymbol{x}}^T \boldsymbol{f}_h. \tag{6.26}$$

This confirms that the specific implementation of the rehabilitation controller behaves as a *strictly passive* system with respect to the port $\langle \dot{\boldsymbol{x}}, \boldsymbol{f}_h \rangle$. According to the interconnection theory detailed in Sec. 4.4, the feedback interconnection of this passive robot with a passive human operator guarantees the asymptotic stability of the overall coupled system.

6.4.4 Quasi-static Behavior and Elastic Field Design

Once the stability of the robotic system connected to the user has been proven (as detailed in Sec. 6.4.3 and Chapter 4), it becomes of interest to consider the achievable performance in terms of position error and exchanged forces while the human is interacting with it. Assuming that the velocities and accelerations involved in a typical rehabilitation task are very small, we analyze the behavior of the controlled robot close to an equilibrium state ($\dot{\boldsymbol{x}} \approx 0, \ddot{\boldsymbol{x}} \approx 0$).

Considering that the user is exerting a constant force $\bar{\boldsymbol{f}}_h$, equations (6.14) and (6.22) imply that at equilibrium:

$$f_{\parallel} = \boldsymbol{\varphi}'(\bar{s})^T \cdot \bar{\boldsymbol{f}}_h = 0 \tag{6.27}$$

$$\boldsymbol{f}_{el}(\tilde{\boldsymbol{x}}) = \bar{\boldsymbol{f}}_h. \tag{6.28}$$

Equation (6.27) shows that the force applied by the user at equilibrium must be orthogonal to the tangent vector of the desired curve $\bar{\boldsymbol{x}}_d = \boldsymbol{\varphi}(\bar{s})$. Equation (6.28) indicates that this force must be counteracted by the elastic force acting on the robot, which is caused by the deviation $\tilde{\boldsymbol{x}}$ from $\bar{\boldsymbol{x}}_d$.

From an intuitive user perspective, the system's displacement $\tilde{\boldsymbol{x}}$ should ideally align with the force causing it, similar to a standard mechanical spring. To achieve this, we impose a specific structure on the elastic force function $\boldsymbol{f}_{el}(\tilde{\boldsymbol{x}})$:

$$\boldsymbol{f}_{el}(\tilde{\boldsymbol{x}}) = f_{el}(\|\tilde{\boldsymbol{x}}\|) \frac{\tilde{\boldsymbol{x}}}{\|\tilde{\boldsymbol{x}}\|} \tag{6.29}$$

where $f_{el}(\cdot) \geq 0$ is a scalar function such that $f_{el}(0) = 0$. In this way, the elastic force is always directed along $\tilde{\boldsymbol{x}}$, and its intensity is determined by $f_{el}(\cdot)$. However, the elastic connection plays different roles along the tangent and orthogonal directions to the curve. It needs to ensure minimal tracking error along the curve while still allowing patients to deviate from the planned path without encountering excessive forces. To achieve this, the elastic force is decomposed into two

complementary components:

$$\boldsymbol{f}_{el}(\tilde{\boldsymbol{x}}) = \boldsymbol{f}_{el,\parallel}(\tilde{\boldsymbol{x}}_{\parallel}) + \boldsymbol{f}_{el,\perp}(\tilde{\boldsymbol{x}}_{\perp}) \tag{6.30}$$

where:

$$\tilde{\boldsymbol{x}}_{\parallel} = \boldsymbol{\varphi}'(\bar{s})\boldsymbol{\varphi}'(\bar{s})^T\,\tilde{\boldsymbol{x}} \tag{6.31}$$

$$\tilde{\boldsymbol{x}}_{\perp} = \left(\boldsymbol{I}_3 - \boldsymbol{\varphi}'(\bar{s})\boldsymbol{\varphi}'(\bar{s})^T\right)\,\tilde{\boldsymbol{x}} \tag{6.32}$$

represent the tangent and orthogonal displacements to the curve at point $\boldsymbol{\varphi}(\bar{s})$, respectively. Functions $\boldsymbol{f}_{el,\parallel}(\cdot)$ and $\boldsymbol{f}_{el,\perp}(\cdot)$ maintain the structure described in (6.29). From (6.30) and (6.29), the potential function that defines $\boldsymbol{f}_{el}(\tilde{\boldsymbol{x}})$ according to (6.23) can be derived as:

$$U_{el}(\tilde{\boldsymbol{x}}) = u_{el,\parallel}(\|\tilde{\boldsymbol{x}}_{\parallel}\|) + u_{el,\perp}(\|\tilde{\boldsymbol{x}}_{\perp}\|)$$

where $u_{el,*}(z) = \int f_{el,*}(z)dz$ is the primitive of $f_{el,*}(\cdot)$ such that $u_{el,*}(0) = 0$.

Tangent Direction: Linear Elasticity

If we assume $f_{el,\parallel}(z) = \kappa\, z$ where κ is a positive constant, the constitutive equation of a standard linear spring is obtained:

$$\boldsymbol{f}_{el,\parallel}(\tilde{\boldsymbol{x}}_{\parallel}) = \kappa\,\tilde{\boldsymbol{x}}_{\parallel}. \tag{6.33}$$

This expression is used along the tangent direction, where a large value of κ helps ensure minimal tracking error. However, due to equations (6.27) and (6.28), this component is not perceived by the user when moving slowly along the curve (since at equilibrium $f_{\parallel} = 0$).

Orthogonal Direction: Nonlinear Virtual Channel

A more effective way to define a fixture for rehabilitation applications in the normal plane to the desired path is based on the function:

$$f_{el,\perp}(z) = \chi\frac{\delta^2 z}{\delta^2 - z^2} \;\;\Rightarrow\;\; \boldsymbol{f}_{el,\perp}(\tilde{\boldsymbol{x}}_{\perp}) = \chi\frac{\delta^2}{\delta^2 - \|\tilde{\boldsymbol{x}}_{\perp}\|^2}\tilde{\boldsymbol{x}}_{\perp} \tag{6.34}$$

where χ and δ are free parameters that define the stiffness for small deformations ($z \approx 0$) and the maximum allowable displacement, respectively. As shown in

Fig. 6.4, when the error z approaches δ, the magnitude of the elastic force tends to infinity. In this way, the motion of the patient is restricted to a maximum distance δ in the normal direction to the desired geometric path.

Interestingly, the potential function derived from (6.34):

$$U_{el,\perp}(\tilde{\boldsymbol{x}}_\perp) = \frac{\chi\delta^2}{2}\log\left(\frac{\delta^2}{\delta^2 - \|\tilde{\boldsymbol{x}}_\perp\|^2}\right), \tag{6.35}$$

has the same form as standard Barrier Lyapunov Functions [136], used for preventing constraint violation in dynamic systems.

The behavior of the overall system is illustrated in Fig. 6.5 by means of an equivalent mechanical representation: while the human force $\boldsymbol{f}_h$ affects the robot, only its tangent component moves the mass along the desired path. At equilibrium, when this component is equal to zero, the normal component $F_\perp$ causes a deviation from the desired geometric path along the normal direction.

The control scheme obtained by combining these components:

$$\boldsymbol{f}_{el}(\tilde{\boldsymbol{x}}) = \kappa\,\tilde{\boldsymbol{x}}_\parallel + \chi\frac{\delta^2}{\delta^2 - \|\tilde{\boldsymbol{x}}_\perp\|^2}\tilde{\boldsymbol{x}}_\perp \tag{6.36}$$

is a specific instance of a band-type controller. This type of controller defines the boundaries of a virtual channel [112], [128]. Within the channel, there exists a residual elastic force towards the reference trajectory whose intensity can be freely chosen by adjusting χ.

Key advantages of this scheme include:

- **No time constraints:** The movement of the human limb is not restricted to a specific trajectory or velocity profile [137], but is determined by the interaction between the user and the robot/virtual mass. The absence of a time constraint makes the duration of the motion a useful parameter for estimating the functional ability of the subjects.

- **Robustness:** The implementation, based on force-to-position causality, does not require knowledge of the normal direction to the desired reference path [138], avoiding computational issues and singularities (e.g., at path intersections).

- **Flexibility:** Assistive (help-as-needed) or resistive forces can be easily integrated into the control scheme by adding an appropriate virtual force in Equation (6.14) governing the mass dynamics.

6.4.5 Extension to 6-DoF Orientational Virtual Channel

While the previous sections detailed the design of a virtual channel for translational motions, the proposed HIC architecture can be naturally extended to encompass the full $SE(3)$ task space. This is particularly relevant when the rehabilitation exercise requires the patient to follow a specific evolution of the limb's orientation along the path, rather than maintaining a fixed posture. To achieve this, the geometric definition of the path is expanded. Alongside the Cartesian position $\boldsymbol{\varphi}(s)$, a desired orientation profile parameterized by the arc-length s is introduced. To avoid representation singularities, such as gimbal lock, unit quaternions are employed. Let $\mathbf{q}_d(s) = \{\eta_d(s), \boldsymbol{\epsilon}_d(s)\}$ denote the desired orientation along the curve, where η_d is the scalar part and $\boldsymbol{\epsilon}_d$ is the vector part. During the LbD phase, this continuous rotational path is generated using Spherical Linear Interpolation (Slerp) between the recorded key-poses. As the virtual mass progresses along the path, providing the instantaneous reference $s(t)$, the corresponding target orientation $\mathbf{q}_d(s(t))$ is evaluated. The orientation error between the actual end-effector orientation $\mathbf{q} = \{\eta, \boldsymbol{\epsilon}\}$ and the desired one is computed using the quaternion product:

$$\mathbf{q}_{err} = \mathbf{q}_d^{-1}(s) \otimes \mathbf{q} = \{\eta_{err}, \boldsymbol{\epsilon}_{err}\}. \tag{6.37}$$

To enforce an orientational virtual channel that mirrors the behavior of the translational one, an elastic restoring torque $\boldsymbol{\tau}_{el}$ is formulated at the control level. By leveraging the vector part of the orientation error, $\boldsymbol{\epsilon}_{err}$, which is proportional to the axis-angle deviation, the nonlinear band-type controller defined in (6.34) can be directly mapped into the rotational domain:

$$\boldsymbol{\tau}_{el}(\boldsymbol{\epsilon}_{err}) = \chi_o \frac{\delta_o^2}{\delta_o^2 - \|\boldsymbol{\epsilon}_{err}\|^2} \boldsymbol{\epsilon}_{err} \tag{6.38}$$

where χ_o represents the rotational stiffness inside the channel, and δ_o defines the maximum allowable angular deviation boundary. To ensure passivity and provide a smooth haptic interaction, a rotational damping component must be coupled with the nonlinear elastic torque. Let $\boldsymbol{\omega}$ denote the actual angular velocity of the end-effector and $\boldsymbol{\omega}_d$ the desired angular velocity, which can be derived from the time derivative of the reference orientation profile along the curve. The angular velocity error is defined as:

$$\boldsymbol{\omega}_{err} = \boldsymbol{\omega} - \boldsymbol{\omega}_d. \tag{6.39}$$

The rotational damping torque $\boldsymbol{\tau}_d$ is formulated to counteract this velocity error:

$$\boldsymbol{\tau}_d(\boldsymbol{\epsilon}_{err}, \boldsymbol{\omega}_{err}) = -d_o(\|\boldsymbol{\epsilon}_{err}\|, \delta_o)\boldsymbol{\omega}_{err} \tag{6.40}$$

where d_o is a state-dependent rotational damping coefficient. Similar to the translational virtual channel design, this coefficient can be kept to a minimal baseline value near the center of the orientation channel (allowing free rotation) and scaled up progressively as the angular deviation $\|\boldsymbol{\epsilon}_{err}\|$ approaches the boundary δ_o. This provides a viscous haptic cue that intuitively warns the user before the rigid elastic intervention of (6.38). The total rotational viscoelastic control action applied to the robot is the superposition of the elastic and damping components:

$$\boldsymbol{\tau}_{ve} = \boldsymbol{\tau}_{el}(\boldsymbol{\epsilon}_{err}) + \boldsymbol{\tau}_d(\boldsymbol{\epsilon}_{err}, \boldsymbol{\omega}_{err}). \tag{6.41}$$

Consequently, the total generalized force (wrench) $\boldsymbol{W}_{ve}$ applied in the HIC control law (6.22) is thus augmented to a full 6-dimensional vector:

$$\boldsymbol{W}_{ve} = \begin{bmatrix} \boldsymbol{f}_{ve}(\tilde{\boldsymbol{x}}, \dot{\tilde{\boldsymbol{x}}}) \\ \boldsymbol{\tau}_{ve}(\boldsymbol{\epsilon}_{err}, \boldsymbol{\omega}_{err}) \end{bmatrix}. \tag{6.42}$$

This full $SE(3)$ formulation guarantees that the user is smoothly guided not only along the 3D spatial trajectory but also through the required rotational sequence. By adopting the nonlinear barrier function for the orientation, the system allows the patient a predefined, safe degree of rotational freedom (defined by δ_o) to accommodate natural wrist movements, while rigidly preventing excessive postural deviations that could compromise the ergonomics or safety of the rehabilitation task.

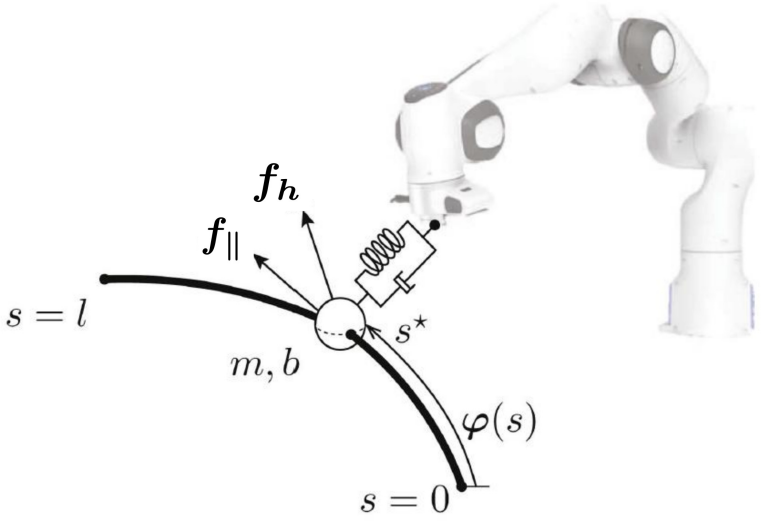

(a)

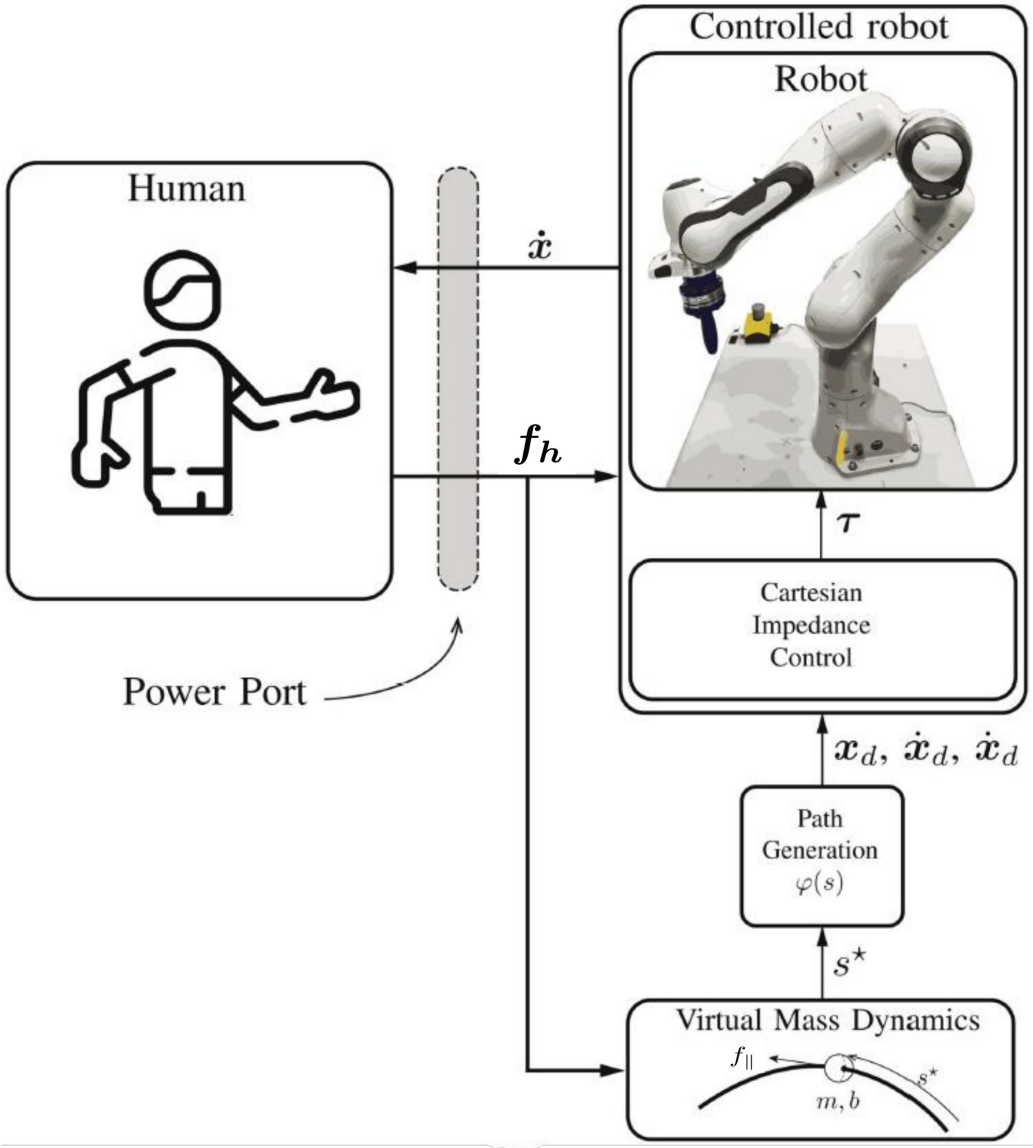

(b)

Figure 6.3: Working principle of the proposed control architecture based on a constrained point-wise mass (a), and related block scheme representation (b).

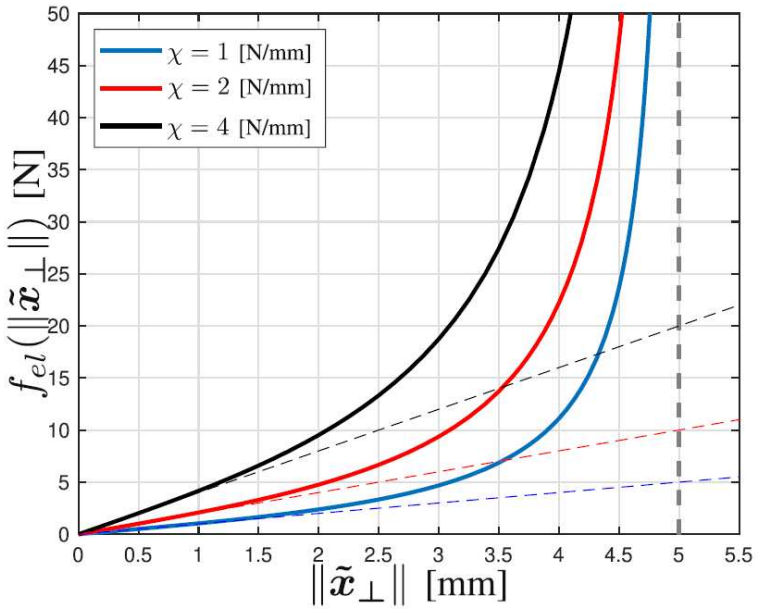

Figure 6.4: Nonlinear elastic function $f_{el}(||\tilde{\boldsymbol{x}}_\perp||) = \chi \frac{\delta^2 ||\tilde{\boldsymbol{x}}_\perp||}{\delta^2 - ||\tilde{\boldsymbol{x}}_\perp||^2}$ for different values of parameter χ ($\delta = 5$ mm). The force diverges as the error approaches the limit δ.

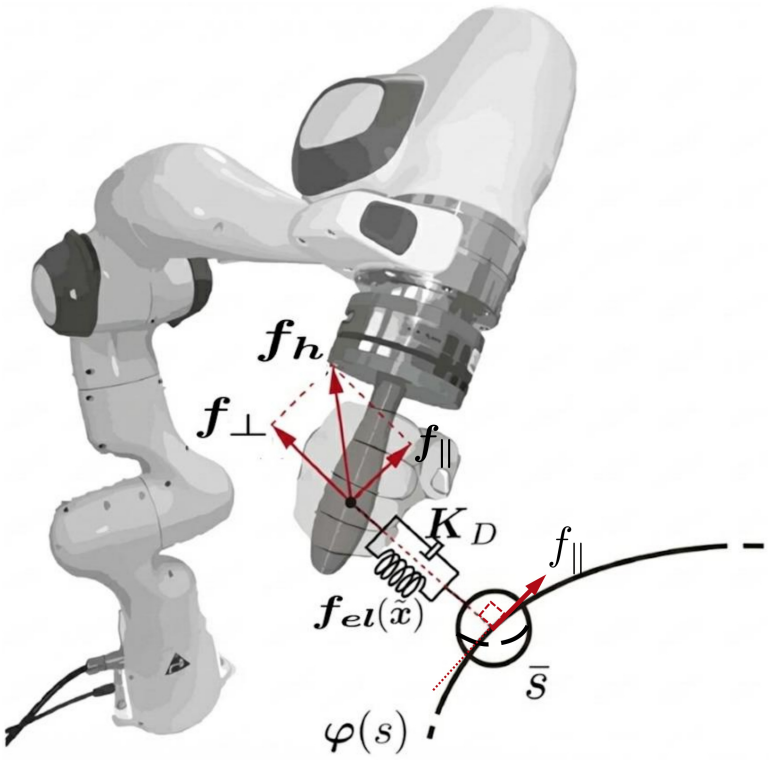

Figure 6.5: Equivalent mechanical system of the proposed controller in an equilibrium configuration.

6.5 Experimental Setup and Task Specification Using LbD

The proposed methodology, which involves selecting the optimal robot configuration, programming the rehabilitative task through demonstration, and executing it via human-robot interaction, has been tested using a Franka Emika Panda, a collaborative robot with 7 degrees of freedom equipped with an Axia80-M20 force-torque sensor mounted on its terminal flange. Since the robot is redundant, a torque vector defined in the null space of the Jacobian transpose, which maximizes the distance from the joint limits, has been added to the torque control defined by (6.17), see [84].

The experimental setup is shown in Fig. 6.6, where two possible end-effectors are considered. Specifically, since the initial goal of the experiments is to evaluate the impact of control parameters on task execution—particularly the stiffness level χ, the channel radius δ, and the implementation of additional assisting or opposing mechanisms—a simple handle has been attached to the force/torque sensor, as shown in Fig. 6.6(a). In the second phase of the experiments, to test the proposed architecture during the assisted execution of Activities of Daily Living (ADL) [6], a purpose-designed constraining mechanism for the patient's wrist was installed on the robot, as shown in Fig. 6.6(b).

6.5.1 Path Generation via LbD

In order to define the geometric path for an exercise, the therapist guides the robot's end-effector within its operational range, and the sequence of points is recorded. As detailed in Chapter 3, raw temporal data from demonstrations are inherently affected by speed variations and pauses. To overcome these limitations

(a) (b)

Figure 6.6: Experimental setup for basic experiments on human-robot co-manipulation tasks (a) and for the assisted execution of Activities of Daily Living (b).

and ensure a consistent geometric definition suitable for the virtual fixture control, the recorded trajectory is processed using the Spatial Sampling Algorithm (SSA) described in Sec. 3.2. This re-parameterization transforms the time-dependent sequence into a regular, spatial-based sequence, effectively decoupling the geometric path from the specific execution speed of the demonstration.

The spatially sampled points are then interpolated with a B-spline curve, providing the analytical definition required for the control law (6.8). Specifically, we define a parametric curve $\boldsymbol{\varphi}(u) : [u_{\min}, u_{\max}] \to \mathbb{R}^3$ as a linear combination of *control points* $\boldsymbol{p}_j \in \mathbb{R}^3$ weighted by *B-spline basis functions* of degree p, $B_j^p(u)$:

$$\boldsymbol{\varphi}(u) = \sum_{j=0}^{N} \boldsymbol{p}_j B_j^p(u), \quad u_{\min} \leq u \leq u_{\max}. \tag{6.43}$$

The vectorial coefficients $\boldsymbol{p}_j$ determine the shape of the curve and are computed by imposing approximation conditions on the samples $\mathbf{q}_j$ of the recorded trajectory. To suppress unwanted movements (e.g., hand tremors) that affect the user's motion during the demonstration, *smoothing* B-splines are employed. They minimize the following cost function:

$$J := \sum_{j=0}^{n} w_j \|\boldsymbol{\varphi}(u_j^\star) - \mathbf{q}_j\|^2 + \lambda \int_{u_{\min}}^{u_{\max}} \left\| \frac{d^2\boldsymbol{\varphi}(\tau)}{d\tau^2} \right\|^2 d\tau. \tag{6.44}$$

This formulation represents a trade-off between the squared approximation error with respect to the demonstrated trajectory and the smoothness (curvature energy) of the resulting curve. The parameter $\lambda \geq 0$ governs this trade-off.

Since selecting individual weights w_j manually is not feasible, a constrained approach for defining $\boldsymbol{\varphi}(u)$ has been adopted, as suggested in [68]. Accordingly, the control points $\boldsymbol{p}_j$ in (6.43) are computed by minimizing the cost function J in (6.44), subject to the constraint:

$$\|\boldsymbol{\varphi}(u_j^\star) - \mathbf{q}_j\| \leq \varepsilon \tag{6.45}$$

where ε is a scalar tolerance value representing the maximum allowable geometric deviation. This constrained formulation is the exact mechanism used to explicitly set and guarantee the geometric accuracy of the system. By defining ε, the operator imposes a hard upper bound on the approximation error. The optimization algorithm will maximize the smoothness of the curve without ever deviating from the raw data points by more than this prescribed threshold. This determinis-

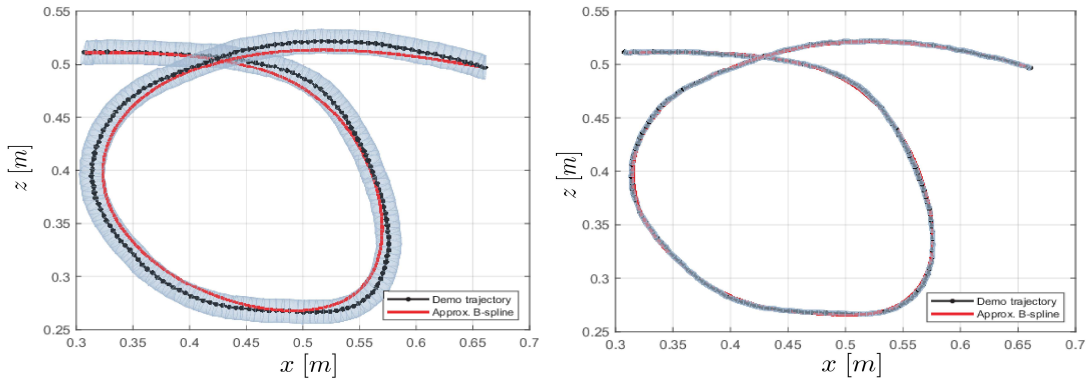

Figure 6.7: Approximation of the demonstrated trajectory using a constrained smoothing B-spline with $\lambda = 0.01$ and a maximum tolerance of $\varepsilon = 0.01$ [m] (a) and $\varepsilon = 0.002$ [m] (b), respectively. The gray zone represents the feasible region within the prescribed tolerance ε from the recorded data points.

tic control over the spatial error makes the framework highly scalable: while a larger tolerance (e.g., 10 mm) can be employed to heavily smooth out pathological tremors in rehabilitation, setting a strictly sub-millimeter ε guarantees the microscopic accuracy necessary to safely deploy this path generation method in robot-assisted surgery.

In Fig. 6.7, the B-spline functions obtained from the same demonstrated trajectory with two different values of ε are shown. It is worth noting that the path exhibits an intersection. Consequently, while the position along the path is unique, the normal direction at the intersection point is not uniquely defined purely by geometry. However, because the control system evaluates the path using the monotonically increasing arc-length parameter s rather than relying on a purely spatial nearest-point search, it inherently resolves this topological ambiguity and traverses the intersection smoothly without losing the correct forward direction. Furthermore, it is crucial to reiterate that the primary advantage of the SSA parameterization lies in its handling of the teaching phase: by entirely decoupling the geometric path from the original temporal domain, it filters out any velocity drops caused by the human pausing or hesitating during the demonstration. This ensures a strictly non-zero and continuous tangent vector $\boldsymbol{\varphi}'(s)$ everywhere, which is the actual mechanism that robustly prevents the stagnation phenomenon during the subsequent robotic execution.

As a final note, in these experiments the orientation of the end-effector was kept constant. However, the proposed framework based on the arc-length variable s can be trivially extended to define a function $\boldsymbol{\varphi}_o(s)$ for orientation, interpolating

the rotation matrices or quaternions recorded during the demonstration.

6.6 Experimental Results and Discussion

To validate the proposed control architecture and evaluate the impact of the control parameters on system performance, several tests were conducted under various control conditions. These tests emulated a rehabilitation exercise along the predefined path shown in Fig. 6.7, collecting forces exchanged during Human-Robot Interaction and measuring the user's deviation from the reference path.

6.6.1 Technical Validation of Control Parameters

In the initial experiments, a healthy user with experience conducted tests to analyze how different control parameters influenced the system's performance. The focus was primarily on the parameters defining the virtual channel: the stiffness $\chi \in \{100, 500, 2500\}\,[\mathrm{N/m}]$ and the radius $\delta \in \{0.01, 0.02, 0.03\}\,[\mathrm{m}]$. This resulted in 3×3 different scenarios, as depicted in Fig. 6.8. For all these tests, mass dynamics parameters were fixed at $m = 5\,[\mathrm{kg}]$ and $b = 15\,[\mathrm{Ns/m}]$.

As qualitatively observed during execution, increasing χ results in stronger guiding forces toward the center of the channel, helping the user stay aligned with the path. Conversely, increasing δ while keeping χ constant weakens the perceived guidance, allowing more lateral movement before encountering resistance (a "wall" effect at the channel boundaries).

Trade-Off Between Stiffness (χ) and Radius (δ)

Figure 6.9 illustrates the magnitude of the deviation from the reference path in the orthogonal direction ($\|\tilde{\boldsymbol{x}}_{\perp}\|$) for each (χ, δ) combination. The results indicate that higher χ values enhance path-following precision, while δ affects the maximum permissible lateral displacement. However, for sufficiently high χ values, δ has minimal impact on the average deviation.

By comparing these tracking errors with the normal forces exerted by the user (Fig. 6.10), the importance of haptic cues becomes evident. Variations in δ do not significantly influence the average normal forces, while increasing χ slightly raises them (remaining around $5 - 6$ N). This suggests a minimum force level is necessary to guide a collaborative user along the path. However, analyzing the *peak forces* (Fig. 6.11) reveals that lower values of χ result in higher force spikes.

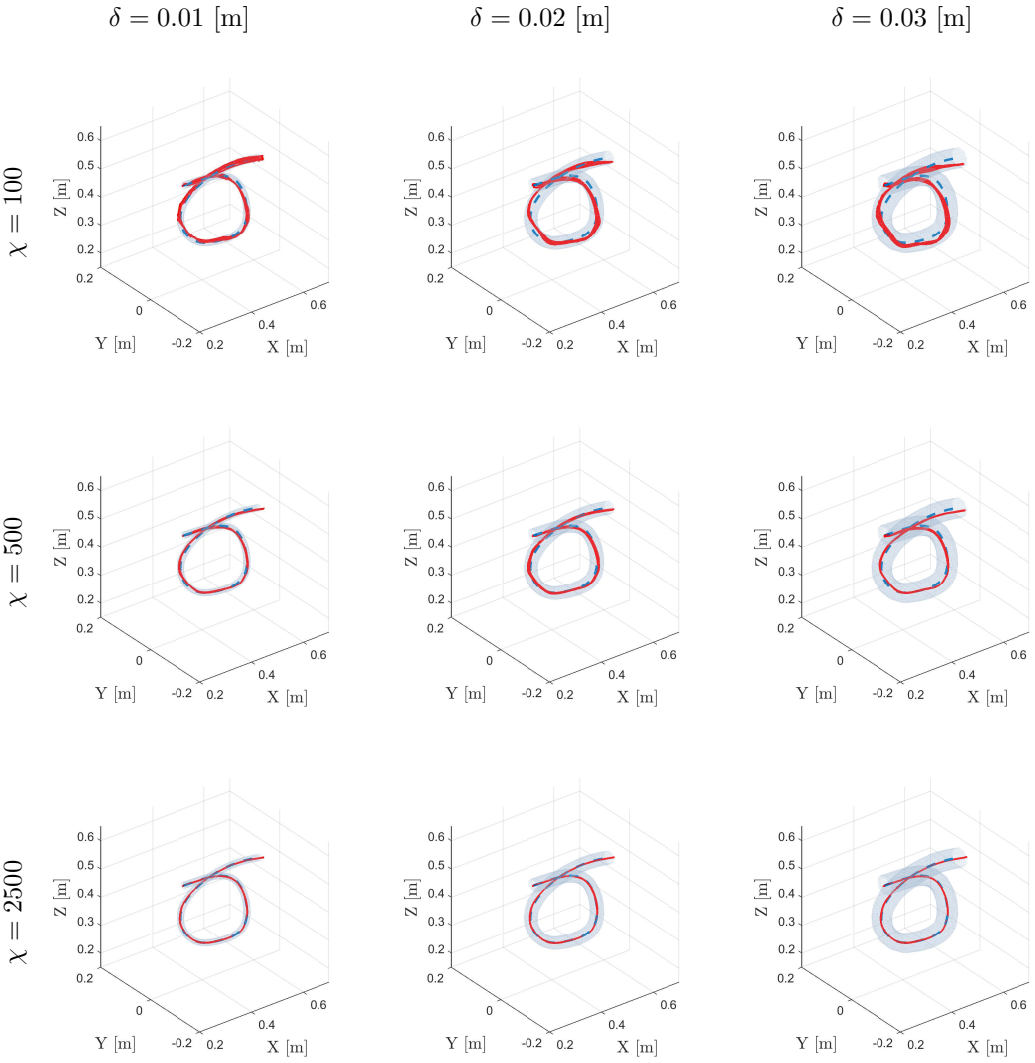

Figure 6.8: Executions of the rehabilitation task defined in Fig. 6.7 recorded under different values for stiffness χ [N/m] and channel radius δ [m].

This phenomenon is particularly pronounced for smaller δ values, where users tend to "bounce" between the virtual channel walls.

In conclusion, stiffness χ and radius δ mainly affect the accuracy of motion reproduction rather than the average exchanged forces. High levels of χ promote smooth guidance, whereas small radii δ combined with low stiffness can induce jerky behaviors.

Influence of Virtual Mass Parameters (m, b)

Additionally, the impact of virtual mass parameters m and b on system dynamics was examined. As shown in Fig. 6.12, reducing the parameters to $m = 1\,[\text{kg}]$ and $b = 3\,[\text{Ns/m}]$ decreased the user-applied tangential force component ($\boldsymbol{f}_{\parallel}$),

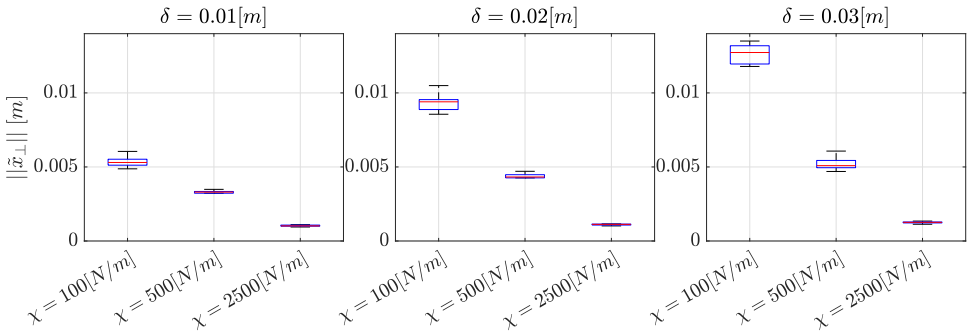

Figure 6.9: Deviation with respect to the reference path in the orthogonal direction obtained in the experiments shown in Fig.6.8.

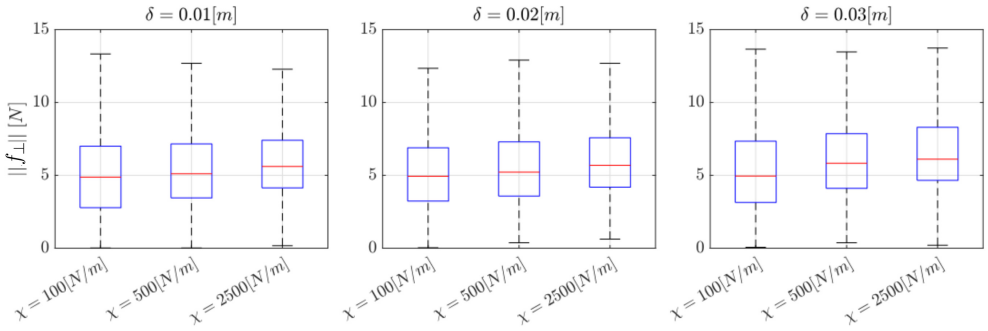

Figure 6.10: Normal forces exchanged in the experiments shown in Fig.6.8.

thereby lowering the physical effort required for task completion. This confirms that tuning m and b effectively adapts the virtual mass dynamics to accommodate different user physical conditions.

Furthermore, Fig. 6.13 illustrates how the introduction of a constant virtual force (± 1 N) can provide either assistive (positive) or resistive (negative) support, directly modifying the tangential forces exerted by the user without affecting the constraint parameters.

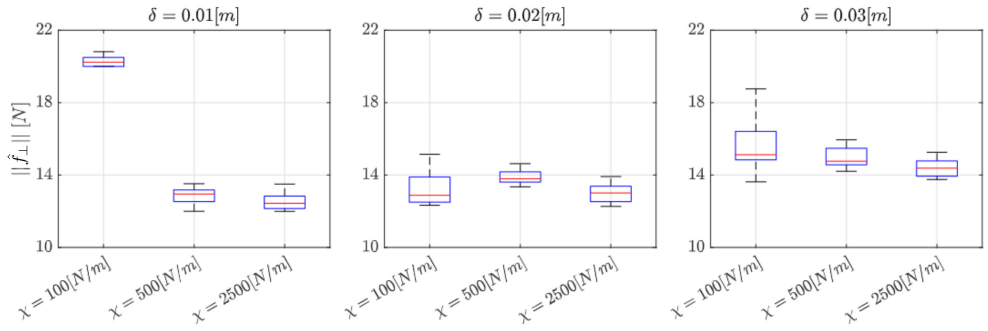

Figure 6.11: Peak values of the normal forces exchanged in the experiments shown in Fig.6.8.

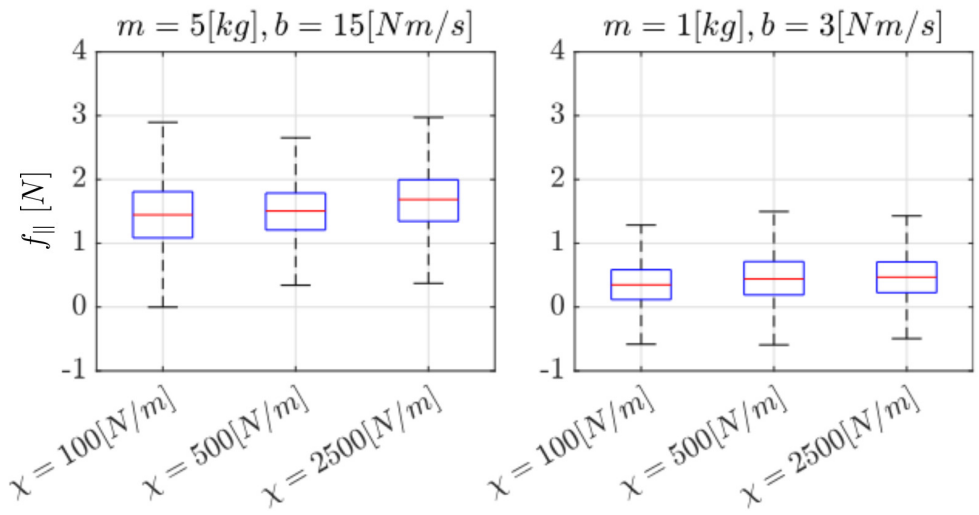

Figure 6.12: Tangential forces exerted by the user with different values of m and b ($\delta = 0.03$ m).

6.6.2 Statistical Analysis of User Perception

To validate the system from a user experience perspective, 10 healthy participants (7 males, 3 females, mean age 32) with no prior robotic experience were recruited. A questionnaire adapted from the NASA-TLX [139] was administered to assess *Physical Demand, Performance, Effort,* and *Frustration* across six different parameter configurations (increasing χ and δ).

A one-way ANOVA analysis (significance $p < 0.05$) revealed the following insights (Fig. 6.14):

- *Performance ($p < 0.001$):* Significant improvement with higher χ. Users felt more efficient and precise when the guidance was stiffer.
- *Effort ($p < 0.01$):* Higher χ values significantly reduced perceived effort, as the robot provided clearer haptic cues.
- *Frustration ($p < 0.01$):* Increasing the channel radius δ reduced frustration, allowing users more freedom without feeling constantly constrained ("wall" effect).
- *Physical Demand:* No significant differences were observed across conditions, confirming that physical effort is primarily determined by m and b (as discussed in Sec. 6.6.1) rather than the geometric constraints.

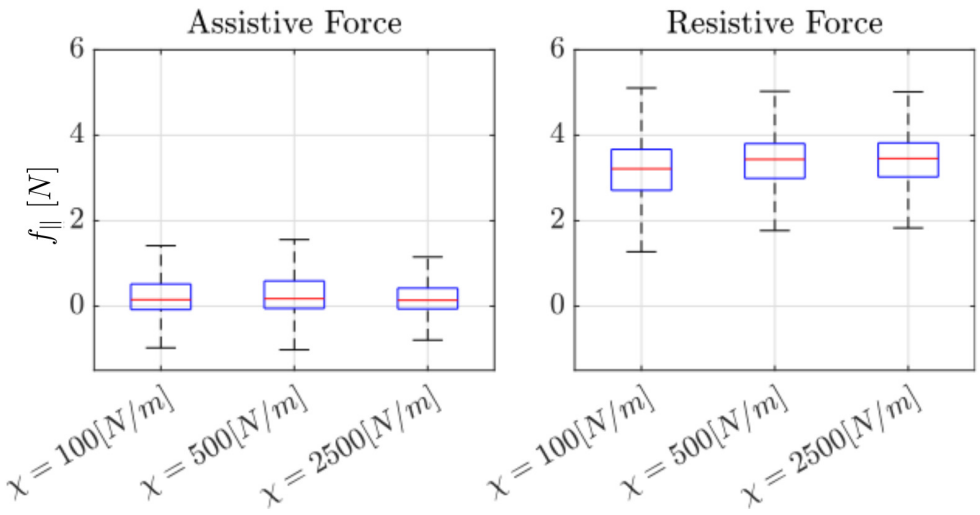

Figure 6.13: Tangential forces exerted by the user with the application of 1 N assistive or resistive force.

Retrospective Power Analysis

Given the relatively small sample size ($N = 10$) employed in the experimental validation, a retrospective power analysis was conducted ($\alpha = 0.05$, two-sided paired t-test) to mathematically assess the robustness of the findings and contextualize the pilot nature of the study. The analysis reveals that a sample size of 10 participants requires an exceptionally large effect size (Cohen's $d \geq 1.0$) to achieve the standard statistical power of $1 - \beta = 0.80$. For the primary *objective metrics*, the transition between different stiffness parameters generated highly deterministic mechanical responses. Specifically, comparing the lowest and highest stiffness conditions ($\chi = 100$ vs $\chi = 2500$ N/m at $\delta = 0.01$ m), the mean orthogonal tracking error ($\|\tilde{\boldsymbol{x}}_{\perp}\|$) yielded a massive effect size of $d = 12.84$, and the peak orthogonal interaction force ($\|\hat{\boldsymbol{F}}_{\perp}\|$) yielded $d = 1.72$. These massive effect sizes effectively bring the statistical power to $> 99.8\%$. This formally confirms that the objective kinematic and dynamic validation of the control algorithm is statistically robust and entirely unaffected by the small sample size. Regarding the *subjective human-factors evaluations* (NASA-TLX), the power analysis perfectly mirrored the ANOVA results. For highly divergent conditions (e.g., the perceived Effort and Performance between $\chi = 100$ and $\chi = 2500$ N/m), the subjective responses yielded large effect sizes (e.g., $d = 1.23$ for Effort), achieving a robust power of $> 93\%$. However, standard subjective usability studies frequently deal with moderate effect sizes ($d \approx 0.5 - 0.8$), for which a sample of $N = 10$ provides inadequate power (typically between 30% and 60%). This structural inability

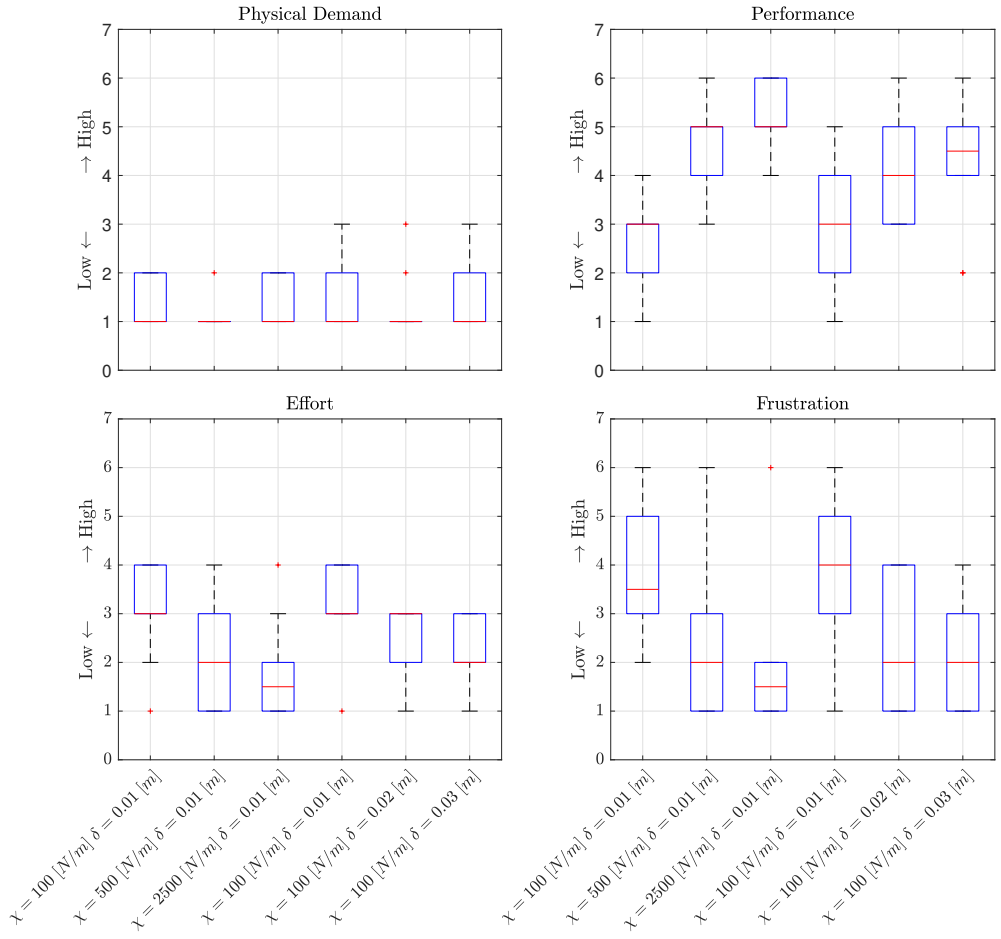

Figure 6.14: Users' opinions about Physical Demand, Performance, Effort, and Frustration related to the tests in Fig. 6.8.

to reliably detect moderate usability trends—such as the non-significant results obtained for Frustration—statistically formalizes the pilot nature of the human-factors assessment. Larger-scale clinical trials are therefore strictly required to confidently generalize these subjective interaction profiles to a broader patient population.

6.6.3 Performance Comparison with State of the Art

To evaluate the advantages of the proposed solution over a widely used method in the rehabilitation field, a comparative study was conducted. Specifically, the proposed method was compared with the approach presented in [6], which is based on the Dynamic Movement Primitive (DMP) formulation. This approach was selected as a benchmark because it explicitly utilizes a Learning by Demonstration (LbD) procedure to define the rehabilitation task—one of the main features of

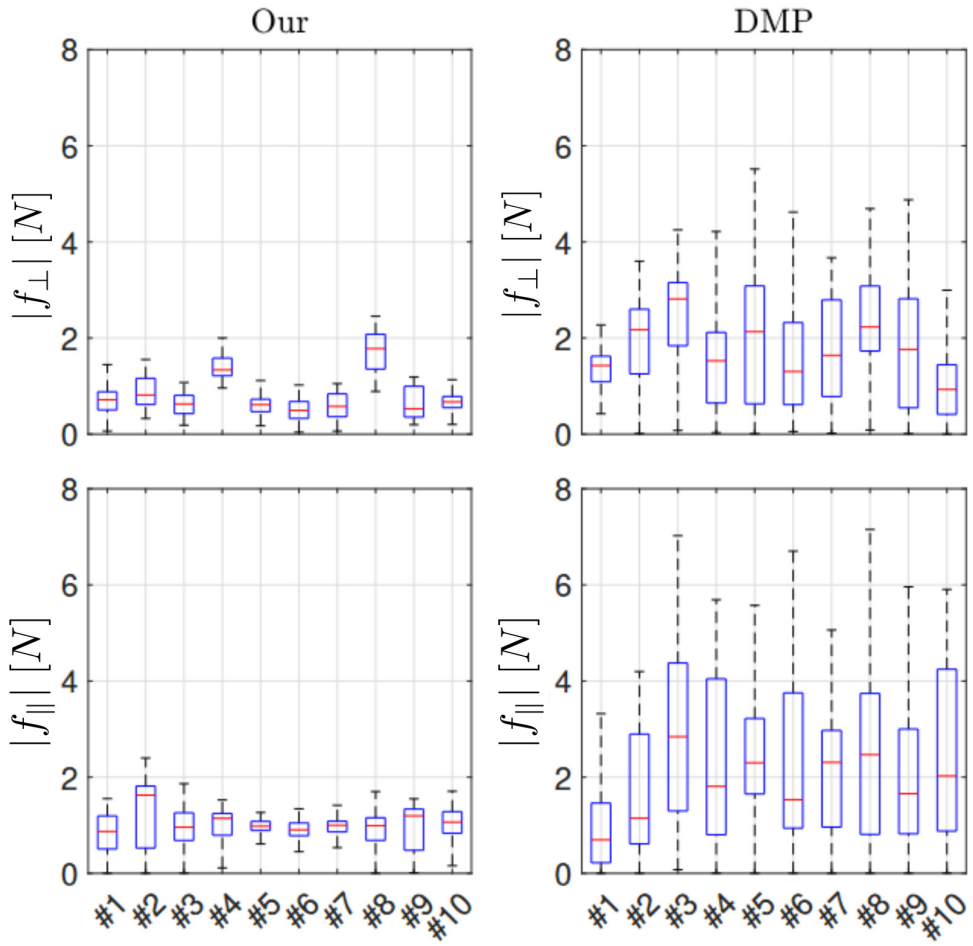

Figure 6.15: Forces recorded during the comparison between our method and the DMP-based approach.

the proposed framework—applied to a typical Activities of Daily Living (ADL).

In this scenario, the robot assists the patient in reaching and picking up a bottle from a table, as illustrated in the experimental setup (Fig. 6.6(b)). For this study, a custom-designed end-effector was developed to securely connect the user's wrist to the robot's terminal flange, ensuring both comfort and effective force transfer between the user and the manipulator during the exercise.

After demonstrating the task by guiding the robot under gravity-compensation conditions, both algorithms were applied to replicate the motion. The interaction forces recorded during the execution are presented in Fig. 6.15.

As shown in Fig. 6.15, the forces exerted during task execution using the DMP-based method [6] were generally higher than those recorded with the proposed method. The force magnitudes are plotted to emphasize their relative intensities.

A key observation relates to the nature of the patient interaction. In the DMP-based approach, the trajectory generation typically embeds a specific time

law (or phase variable). Consequently, the patient operates exclusively in a *passive mode*, often resulting in forces being applied by the robot in the opposite direction to the desired motion if the patient is not perfectly synchronized with the robot's timing. By contrast, the proposed method enables a broader range of rehabilitation modes, from fully passive assistance in the early stages to more *active participation* as the patient's abilities progress, thereby eliminating the rigid passivity inherent in standard DMP-based systems.

The comparison highlights several key advantages of the *Admittance Guidance Virtual Fixture* control that have direct implications for real-world rehabilitation applications:

- **Enhanced Patient Comfort:** The approach significantly reduces interaction forces compared to the DMP-based method. This is due to the adaptive compliance of the virtual fixture, which accommodates natural variations in patient movement without generating excessive corrective forces, thereby enhancing user comfort and reducing fatigue.

- **Active User Engagement:** Unlike the DMP-based approach, which enforces predefined movement patterns (limiting the user to passive following), the proposed method allows controlled deviations within a virtual path. This fosters greater patient participation, making rehabilitation more engaging and motivating, which is crucial for long-term adherence.

- **Improved Adaptability:** The stiffness level (χ) and channel width (δ) can be dynamically adjusted to match different rehabilitation phases, allowing a smooth transition from guided exercises in early rehabilitation to more autonomous movements in later stages.

A crucial distinction of this approach is its flexibility in trajectory execution. Unlike DMP-based methods, which impose rigid timing constraints, the proposed system allows patients to regulate their movement speed autonomously, supporting a more natural rehabilitation process. This adaptability facilitates both passive and active rehabilitation scenarios, adjusting the level of assistance based on the patient's progress.

Moreover, the system enables further customization by allowing the application of assistive or resistive forces, tailoring the rehabilitation experience to the individual's specific needs. This ability to dynamically modulate task difficulty contributes to a patient-centered approach that enhances both comfort and effectiveness. These findings highlight that the proposed method is particularly

advantageous for *progressive rehabilitation*, where the required assistance level evolves over time. By offering greater flexibility in guidance and effort modulation, the approach supports a structured transition from externally guided movements to self-initiated motor execution, which is essential for maximizing motor learning during the rehabilitation process.

6.7 Conclusion

This chapter presented a comprehensive framework for integrating cobots into upper-limb rehabilitation, addressing both the mechanical layout and the control architecture. By combining a workspace optimization method based on a novel payload index with an admittance-type VF control, the proposed system offers a versatile solution capable of adapting to various stages of patient recovery.

A key distinctive feature of this approach is the seamless integration of passive and active interaction modes within a single control strategy. Unlike traditional systems that are often dedicated to a specific modality, the proposed architecture allows the robot to transition from acting as a supportive guide (passive mode) to providing transparency or resistance (active mode). This flexibility is enabled by the LbD interface, which makes task programming intuitive for therapists, and by the tunable virtual constraints (χ and δ), which effectively modulate the task difficulty.

Experimental validation confirmed the robustness of the system. The results demonstrated that the stiffness level (χ) directly correlates with trajectory precision and perceived performance, while the channel radius (δ) affords the necessary compliance for comfortable interaction. Crucially, statistical analysis of user perceptions aligned with technical metrics, validating the system's usability.

Future developments will focus on translating these technical achievements into clinical practice. The primary goal is to extend the validation to a cohort of patients with motor impairments, assessing the impact of cognitive and psychological factors on rehabilitation outcomes. Furthermore, the integration of physiological metrics, such as Electromyography (EMG), is planned. Electromyography (EMG) signals will be used not only for objective assessment but also to drive the assistance-as-needed mechanism directly, closing the loop between patient effort and robotic assistance.

Chapter 7

EMG-Based Adaptation of Anisotropic Virtual Fixtures for Surgical Resection and Dissection

7.1 Introduction

In the previous chapters, we demonstrated how Virtual Fixture can enhance safety and performance in rehabilitation tasks by constraining the user's motion along a predefined path. While effective for repetitive exercises, the fixed geometry of standard fixtures can become a limitation in more dynamic and unpredictable scenarios. As a final application example of the proposed control framework [79], developed in collaboration with the *Institute of Robotics and Mechatronics* of the *German Aerospace Center* (DLR), we introduce a novel constraint strategy specifically designed for robotic surgery. In this context, the Virtual Fixture does not merely guide the user, but adapts its geometry in real-time based on the surgeon's intent, inferred directly from Electromyography (EMG) signals. This evolution represents a shift from static guidance to a responsive, human-in-the-loop assistance paradigm.

7.1.1 Clinical Context and Challenges

Minimally Invasive Surgery (MIS) has deeply transformed modern clinical practice by reducing patient trauma, accelerating recovery, and improving cosmetic outcomes [140], [141]. These advantages, however, come at the expense of increased technical demands: surgeons must operate with limited workspace, restricted haptic feedback, and indirect visualization, which substantially increases cognitive and physical workload, as consistently highlighted in surgical ergonomics studies [142].

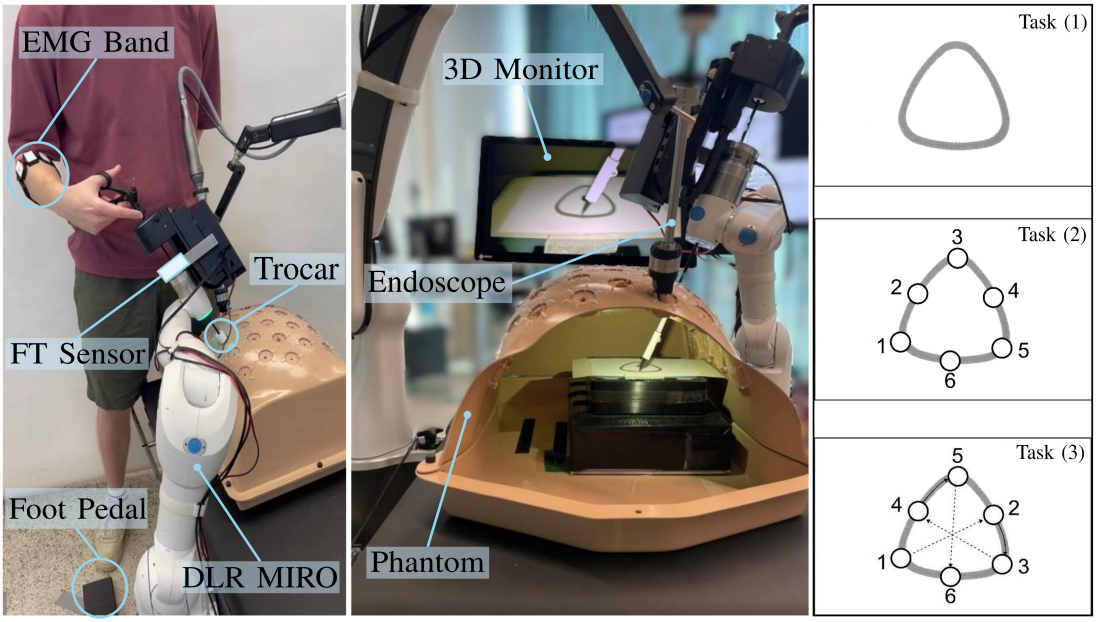

(a) (b) (c)

Figure 7.1: Experimental overview: (a) the robotic platform and user interface, (b) the custom drawing apparatus for the validation study, (c) standardized tasks mimicking surgical surgemes.

Robotic assistance has been progressively introduced to mitigate these challenges, providing enhanced dexterity, motion scaling, and stereoscopic vision [143]. Beyond these well-established advantages, robotic platforms also open the possibility of integrating adaptive assistance mechanisms. In this broader framework, Robotically Assisted Surgical Systems (RASS) are progressively evolving, combining ergonomic improvements with semi-autonomous support functions to enhance surgical precision, to reduce cognitive load, and enable more standardized outcomes across varying surgeon skill levels.

In this regard, Resection and Dissection (R&D) procedures represent a particularly challenging scenario. These tasks are characterized by delicate and often oscillatory ("plucking-like") tool motions, often performed under tissue tension and in close proximity to sensitive anatomical structures. The surgeon must not only maintain precise alignment along the intended dissection line but also frequently detach and re-approach the target region to adjust the entry angle or inspect the resection line. Crucially, safe surgical practice requires that surgeons must never cut blindly; thus, vertical motions of the surgical tool are frequently required to regain line of sight or limit penetration depth. This workflow reflects the known decomposition of complex surgical procedures into a "grammar" of fine-grained surgemes [144]. This context highlights the need for guidance mech-

anisms that are both *anisotropic*, providing selective freedom of motion along task-relevant directions, and *dynamically adaptable*, allowing seamless adaptation of the constraint size, and transitions between guided and free motion [24].

Virtual Fixtures (VF) have been introduced as a promising framework for facilitating such tasks, by modulating the operator's motion through real-time constraints or potential fields enforced by the robot during shared-control [3], [4].

While this strategy has demonstrated benefits in highly-structured applications, such as in orthopedic surgery, where guidance is applied relative to pre-operative models of rigid anatomy [145], their direct application to laparoscopic R&D tasks on soft tissue remains limited. In particular, the deformable nature of the anatomy, the anatomical complexity, the variability of dissection strategies, and the need for frequent re-approaches requires guidance mechanisms that can be adapted online to both the surgical context and the surgeon's intent.

7.1.2 Limitations of Current Guidance Strategies

VFs are categorized into two main classes: *non-adaptive* and *adaptive* [3]. Non-adaptive VFs offer robust guidance but lack flexibility to handle changes in the environment or in the surgical workflow. They are typically defined pre-operatively using 3D anatomical models [20], [21] or vector fields for static safety boundaries [146]. Intra-operative approaches generate fixtures directly within the workflow, relying on motion models like minimum-jerk trajectories [147] or manual point marking [20]. Vision-based methods have also been proposed for dynamic collision avoidance [26]. However, the inherent rigidity of these methods limits their ability to cope with tissue deformation or discontinuous surgical plans.

Adaptive strategies overcome these limitations by modifying constraints online. *Environment-driven* adaptation employs vision algorithms to track anatomical targets and update the path in real-time [148], while *performance-driven* paradigms dynamically adjust fixture parameters, such as the guidance radius, based on automated real-time skill evaluation [149]. Finally, *user-driven* methods place the surgeon in control, allowing not only geometry re-definition via Kinesthetic Teaching (KT) [24] but also the modulation of the VF to match the operator's voluntary engagement.

A direct physiological measure of such engagement is provided by Electromyography (EMG) signals. Beyond estimating operator stiffness for learning-based automation [150], EMG has been applied to real-time shared control. Existing

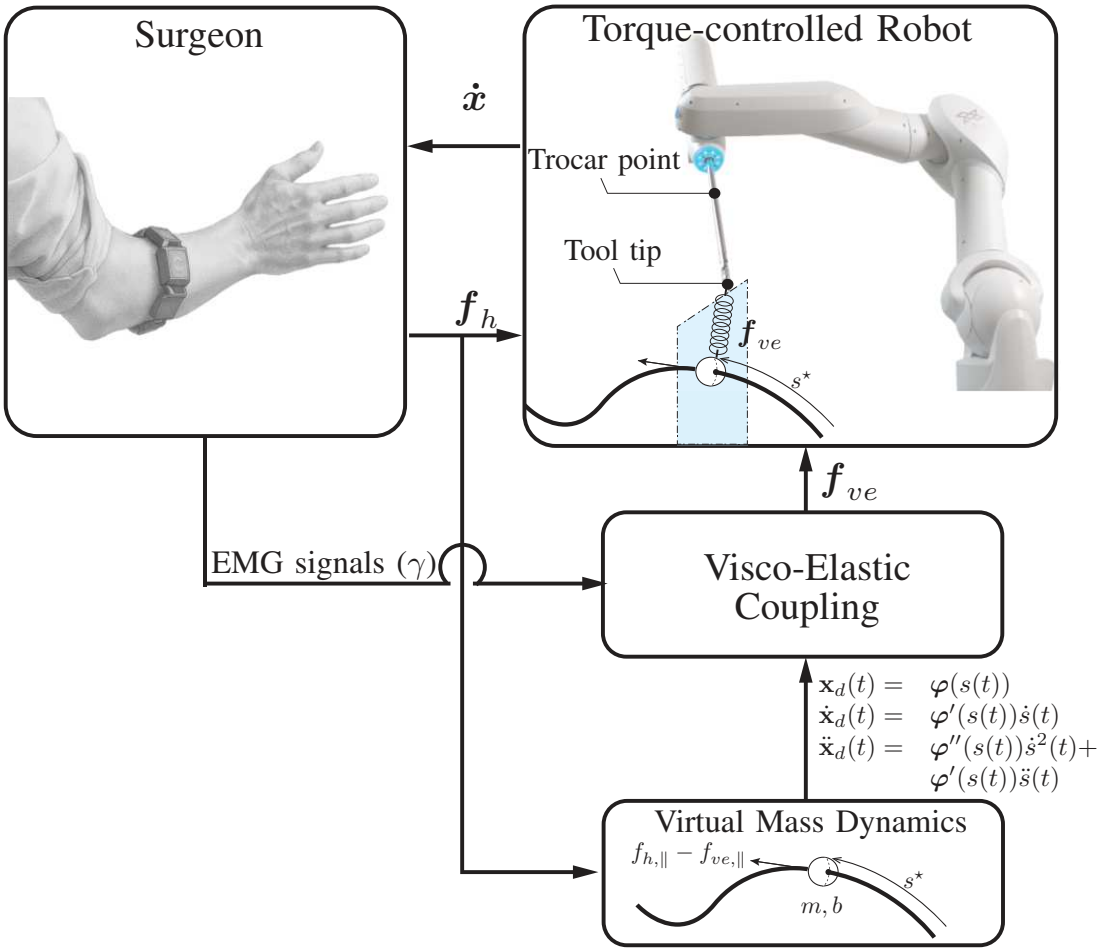

Figure 7.2: Block-diagram of the proposed control architecture for robot-assisted R&D.

approaches typically utilize signal magnitude to continuously regulate the assistance gain [151] or employ classifiers to trigger discrete switches between control modes [152], allowing the user to modulate the robot's behavior.

7.1.3 Proposed Approach and Contributions

In this chapter, we propose a novel control architecture for adaptive virtual fixtures, depicted in Fig. 7.2. A reference path, defined via KT by having the user guide the Tool Center Point (TCP), serves as a constraint for a virtual mass, whose dynamics govern the robot's motion along the curve [67]. This path is utilized to generate anisotropic constraints, defining a guidance corridor with independent geometric bounds and stiffness properties along the normal and binormal directions [64]. These constraints restrict motion to the reference path with high precision, while preserving the necessary workspace for the oscillatory

patterns inherent to R&D tasks.

To the best of our knowledge, this method advances the state of the art by introducing a flexible human-in-the-loop interface for direct, continuous VF modulation. Specifically, the main contributions of this work are threefold:

- Development of an anisotropic Virtual Fixture based on a moving frame, enabling smooth execution of R&D tasks while restricting undesired motion;
- Integration of an EMG-based control mechanism that enables continuous adaptation of the constraint size based on the surgeon's muscular co-contraction;
- Design of a dynamic (dis-)engagement mechanism ensuring consistent initialization of virtual mass dynamics from any user-selected point along the path.

7.2 Adaptive Virtual Fixtures Framework

This section outlines the control architecture adopted to implement the proposed virtual fixture, following the design principles introduced in [67]. As illustrated in Fig. 7.2, the force exchanged between the user and the robot is measured and applied to a virtual mass constrained to the desired Cartesian path

$$\boldsymbol{x}_d(t) = \boldsymbol{\varphi}(s(t)), \tag{7.1}$$

parameterized by its arc length s. A suitable viscoelastic coupling, detailed in Sec. 7.2.2, $\boldsymbol{f}_{ve}(\dot{\tilde{\boldsymbol{x}}}, \tilde{\boldsymbol{x}})$, with $\tilde{\boldsymbol{x}} = \boldsymbol{x} - \boldsymbol{x}_d$, where $\boldsymbol{x} \in \mathbb{R}^3$ denotes the Cartesian position of the tool tip, is then defined between the virtual mass and the robot.

This additional force $\boldsymbol{f}_{ve}$ can be integrated into any torque-based robot control scheme to enforce the virtual constraints. For instance, considering the robot dynamics expressed in the operational space [118]:

$$\boldsymbol{\Lambda}(\boldsymbol{q})\ddot{\boldsymbol{x}} + \boldsymbol{\mu}(\boldsymbol{x}, \dot{\boldsymbol{x}}) = \boldsymbol{f}_c + \boldsymbol{f}_{ext}, \tag{7.2}$$

where $\boldsymbol{\Lambda}$ is the (3×3) Cartesian inertia matrix, $\boldsymbol{\mu}(\boldsymbol{x}, \dot{\boldsymbol{x}})$ represents non-inertial forces, and $\boldsymbol{f}_{ext}$ denotes external user interaction forces, the control input $\boldsymbol{f}_c$ can be designed as:

$$\boldsymbol{f}_c = \boldsymbol{\Lambda}(\boldsymbol{q})\ddot{\boldsymbol{x}}_d + \boldsymbol{\mu}(\boldsymbol{x}, \dot{\boldsymbol{x}}) + \boldsymbol{f}_{ve}(\dot{\tilde{\boldsymbol{x}}}, \tilde{\boldsymbol{x}}). \tag{7.3}$$

Conversely, the tangential component of the viscoelastic coupling $\boldsymbol{f}_{ve}$ influences

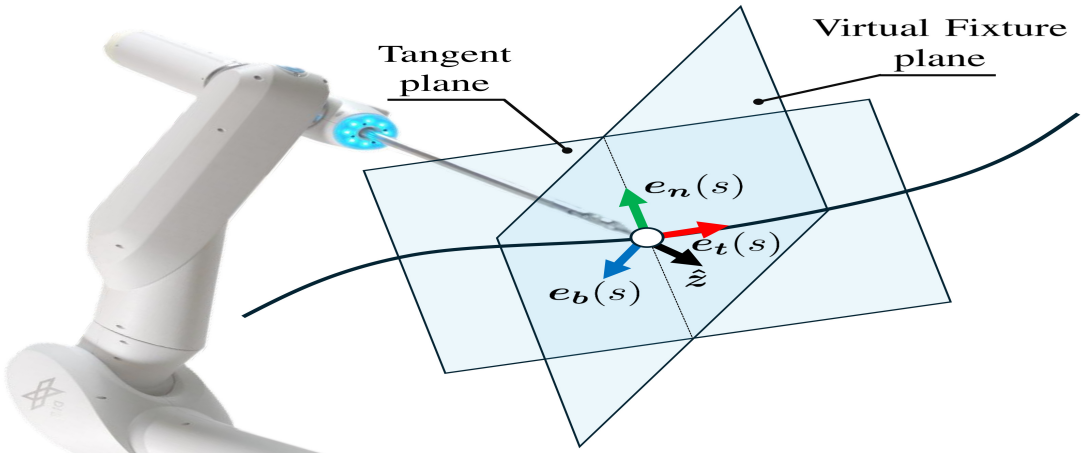

Figure 7.3: Reference path generation and local frame construction based on the tool approach vector.

the dynamics of the virtual mass along the path according to:

$$m\ddot{s}(t) + b\dot{s}(t) = f_{h,\parallel} - f_{ve,\parallel}\big(\dot{\tilde{\boldsymbol{x}}}, \tilde{\boldsymbol{x}}\big). \tag{7.4}$$

Obviously, only the tangential components of the user force $f_{h,\parallel} = \big(\boldsymbol{f}_h\big)^T \boldsymbol{e}_t$ and of the viscoelastic coupling $f_{ve,\parallel}$ determine the progression $s(t)$ of the virtual mass along the path, since the normal components are compensated by the reaction forces imposed by the constraint.

7.2.1 Reference Geometry and Frame Construction

To generate the reference path, we utilize KT [67]. The surgeon manually guides the tool tip within the workspace, and the recorded positions are interpolated via cubic B-splines.

A significant enhancement over the methodology presented in Chapter 6, which was restricted to open path topologies, is the capability of the proposed algorithm to automatically handle both open and closed dissection lines. The algorithm identifies the topology of the demonstrated trajectory by evaluating the Euclidean distance between the first ($\boldsymbol{p}_{start}$) and last ($\boldsymbol{p}_{end}$) recorded samples. If this distance falls below a predefined proximity threshold ϵ_{loop}, i.e., $\|\boldsymbol{p}_{end} - \boldsymbol{p}_{start}\| < \epsilon_{loop}$, the path is classified as a closed loop; otherwise, it is treated as an open line. In the case of an open dissection line, the generation algorithm employs a standard clamped B-spline formulation. Conversely, if a closed loop is detected, the algorithm generates a *periodic* cubic B-spline. This formulation imposes specific cyclic constraints on the control points to guaran-

tee geometric continuity up to the second derivative ($\mathcal{C}^2$) along the entire path, ensuring smoothness even at the junction point. Formally, for a closed path of length L, the following boundary conditions are enforced:

$$\boldsymbol{\varphi}(0) = \boldsymbol{\varphi}(L), \quad \left.\frac{d\boldsymbol{\varphi}}{ds}\right|_{s=0} = \left.\frac{d\boldsymbol{\varphi}}{ds}\right|_{s=L}, \quad \left.\frac{d^2\boldsymbol{\varphi}}{ds^2}\right|_{s=0} = \left.\frac{d^2\boldsymbol{\varphi}}{ds^2}\right|_{s=L}. \tag{7.5}$$

Converting this representation to an arc-length parameterization yields a time-independent geometric description $\boldsymbol{\varphi}(s)$ of the task.

Subsequently, to enable an anisotropic fixture definition, a local orthonormal frame $\{\boldsymbol{e}_t, \boldsymbol{e}_n, \boldsymbol{e}_b\}$ attached to the virtual mass is constructed along this path (Fig. 7.3). Unlike a standard Frenet frame, this basis explicitly accounts for the tool approach direction $\hat{\boldsymbol{z}}$ recorded during KT. The tangent vector $\boldsymbol{e}_t(s)$ aligns with the path derivative $d\boldsymbol{\varphi}/ds$. To facilitate task-specific anisotropy, the normal $\boldsymbol{e}_n(s)$ is defined by projecting $\hat{\boldsymbol{z}}$ onto the plane orthogonal to $\boldsymbol{e}_t$, while the binormal completes the right-handed basis as $\boldsymbol{e}_b = \boldsymbol{e}_t \times \boldsymbol{e}_n$. This construction allows defining independent constraints along the tool axis and its orthogonal plane.

7.2.2 Anisotropic Virtual Fixture Formulation

The viscoelastic force is decomposed into tangential and orthogonal components:

$$\boldsymbol{f}_{ve} = \boldsymbol{f}_{ve,\parallel} + \boldsymbol{f}_{ve,\perp}. \tag{7.6}$$

The tangential component

$$\boldsymbol{f}_{ve,\parallel} = \left(k_t \tilde{x}_t + d_t \dot{\tilde{x}}_t\right)\boldsymbol{e}_t \tag{7.7}$$

enforces synchronization between the TCP and the virtual mass. The orthogonal component $\boldsymbol{f}_{ve,\perp}$ constrains the surgeon motion within a virtual corridor spanned by the normal and binormal directions $\boldsymbol{e}_n$ and $\boldsymbol{e}_b$, respectively (Fig. 7.4):

$$\boldsymbol{f}_{ve,\perp} = f_{ve,n}\,\boldsymbol{e}_n + f_{ve,b}\,\boldsymbol{e}_b. \tag{7.8}$$

Each orthogonal component $i \in \{n, b\}$ follows a nonlinear viscoelastic law

$$f_{ve,i} = k_i\,\mathrm{dz}(|\tilde{x}_i|, \delta_i) + d_i(|\tilde{x}_i|, \delta_i)\,\dot{\tilde{x}}_i, \tag{7.9}$$

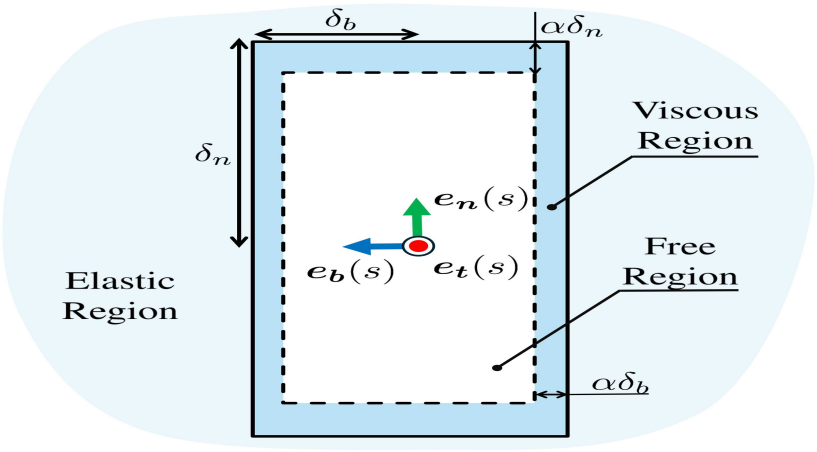

Figure 7.4: Schematic representation of the anisotropic constraint defining the virtual corridor around the path.

where the elastic term is defined through a *dead-zone* function that specifies a free-motion region of width δ_i:

$$\mathrm{dz}(|\tilde{x}_i|, \delta_i) = \begin{cases} 0, & \text{if } |\tilde{x}_i| \leq \delta_i, \\ |\tilde{x}_i| - \delta_i, & \text{if } |\tilde{x}_i| > \delta_i. \end{cases} \tag{7.10}$$

To ensure smooth transitions at the boundary of the dead zone, the damping coefficient d_i is progressively activated within a transition band of width $\alpha\delta_i$, with $\alpha \in [0, 1]$:

$$d_i(|\tilde{x}_i|, \delta_i) = \begin{cases} D_i, & \text{if } |\tilde{x}_i| > \delta_i, \\ \dfrac{|\tilde{x}_i| - (1-\alpha)\delta_i}{\alpha\delta_i} D_i, & \text{if } (1-\alpha)\delta_i \leq |\tilde{x}_i| \leq \delta_i, \\ 0, & \text{otherwise.} \end{cases} \tag{7.11}$$

This independent formulation along the normal and binormal directions results in a rectangular guidance corridor. While simple to implement, the sharp corners of this geometry may lead to abrupt variations in the constraint force. Alternative corridor shapes, such as elliptical or stadium-like geometries, could be adopted to obtain smoother boundaries.

7.3 Constraint Adaptation via EMG-Based Interaction

Standard non-adaptive Virtual Fixtures, defined by fixed geometries, offer robust guidance in structured tasks but lack the flexibility to handle variations in the surgical workflow or the surgeon's immediate intent (e.g., re-approaching a dissection plane). To overcome this limitation, this section introduces a mechanism to dynamically adapt the size of the virtual constraint based on the user's intention, inferred from forearm muscle contractions. The control system is augmented with a wearable interface that records Electromyography (EMG) signals and feeds them back in real-time to the high-level controller to modulate the geometry of the VF.

7.3.1 Signal Processing

To obtain a quantitative measure of the user's muscular contraction from the forearm, EMG signals were acquired using a MYO® Armband (Thalmic Labs, Canada) [153] and processed in real-time. The raw multi-channel data, however, is often noisy and requires a robust processing pipeline to be reliably interpreted. To obtain a robust scalar activation index $\gamma(t) \in [0, 1]$, the raw EMG channels were processed via Mean Absolute Value, smoothed with a 0.5 s moving average window to reject high-frequency noise, and finally normalized.

7.3.2 Constraint Adaptation via an EMG-Based Virtual Clutch

The dimensions of the virtual channel (Fig. 7.4), denoted by δ_i ($i \in \{n, b\}$), are modulated in real-time by a virtual clutch logic driven by the activation index $\gamma(t)$.

When the user wishes to disengage the constraint (e.g., to reposition the tool), they contract their forearm muscles. If the signal exceeds the threshold ($\gamma(t) \geq \bar{\gamma}$), the system activates a *manual widening* mode: the constraint boundary $\delta_i(t)$ instantly expands to match the current deviation, $\delta_i(t) \leftarrow \max(|\tilde{x}_i(t)|, \bar{\delta}_i)$, allowing resistance-free motion.

Conversely, when muscles are relaxed ($\gamma(t) < \bar{\gamma}$), the clutch triggers an *automatic shrinking* mode. In this state, the boundary $\delta_i(t)$ tracks the user's motion only when they move towards the reference path ($d|\tilde{x}_i|/dt < 0$), progressively

Algorithm 1 EMG-Based Constraint Size Adaptation

Require: $|\tilde{x}_i(t)|$; $\gamma(t)$; $\bar{\delta}_i$
Ensure: Adapted constraint width $\delta_i(t)$ for $i \in \{n, b\}$
if $\gamma(t) \geq \bar{\gamma}$ **then** % Manual widening
    Set $\delta_i(t) \leftarrow \max(|\tilde{\boldsymbol{x}}_i(t)|, \bar{\delta}_i)$
else if $\frac{d}{dt}|\tilde{\boldsymbol{x}}_i(t)| < 0$ **then** % Automatic Shrinking
    Update $\delta_i(t) \leftarrow \max(|\tilde{\boldsymbol{x}}_i(t)|, \bar{\delta}_i)$
else % Constraint holding
    Keep current values of δ_i
end if

reducing δ_i until the nominal size $\bar{\delta}_i$ is restored. This unidirectional update logic prevents the user from experiencing sudden elastic forces upon re-engagement.

7.3.3 Technical Note: OR Robustness and False Positives Handling

While the proposed EMG-based virtual clutch demonstrated high efficacy in a controlled laboratory environment, its translation to a real Operating Room (OR) introduces critical technical challenges. The OR is an electrically hostile environment where the Signal-to-Noise Ratio (SNR) of surface EMG can be severely degraded by intense electromagnetic interference from active surgical instruments, variations in skin-electrode impedance due to sweating, and electrode displacement over prolonged procedures. To maintain a reliable SNR, the sensory interface must overcome consumer-grade hardware, necessitating medical-grade differential amplifiers with an exceptionally high Common Mode Rejection Ratio (CMRR), active shielding, and hardware-level notch filtering. Furthermore, a primary safety concern regarding the virtual clutch is the risk of "false positives"—accidental, postural, or reflexive muscle contractions that could trigger an unintended disengagement of the virtual fixture constraints. Unintended loss of guidance during a delicate dissection phase could severely compromise patient safety. To mitigate this risk, the simple amplitude-based thresholding ($\gamma > \bar{\gamma}$) utilized in this proof-of-concept must be reinforced through a multi-layered safety architecture. Basic safeguards could include time-domain hysteresis, which imposes a minimum activation dwell-time (e.g., 200 ms) to filter out brief reflexive twitches, as well as kinematic gating, which acts as a context-aware interlock to prevent disengagement if the robot is exerting high interaction forces against the tissue. Most interestingly, however, the scalar intensity threshold could be entirely replaced by advanced Spatial Pattern Recognition. By training Ma-

chine Learning classifiers to recognize the specific spatial activation pattern of an intentional antagonist co-contraction, the system could reliably distinguish a deliberate disengagement command from the generic forearm tension caused by tightly gripping the tool handle, thereby ensuring a highly robust, intelligent, and safe human-robot interface.

7.4 Experimental Evaluation

To assess the effectiveness of the proposed EMG-based adaptive Virtual Fixture in assisting complex R&D tasks, a pilot user study was conducted comparing the assistance method against free-motion execution. The primary objective was to verify the efficacy of the system. It was hypothesized that the proposed solution would significantly improve task accuracy and movement consistency in path following and target reaching tasks compared to unassisted execution. Furthermore, the adaptive assistance was expected to reduce cognitive workload and perceived effort, particularly in complex tasks requiring frequent transitions between continuous tracking and discrete positioning.

7.4.1 Sample

The study involved seven participants (four male and three female), with ages ranging from 24 to 29 years. All participants were right-handed. The group consisted of untrained users without a specific surgical background, chosen to evaluate the intuitiveness of the system for novice operators.

7.4.2 Apparatus and Experimental Setup

The proposed VF framework was validated utilizing the setup depicted in Fig. 7.1. It includes a 7-DoF lightweight robotic arm, the DLR MIRO, part of the DLR MiroSurge system [154], a research platform for robotic assistance in laparoscopic surgery. The DLR MIRO was equipped with a DLR telescopic linear axis [155], which serves as the drive unit for inserting and extracting conventional laparoscopic tools, typically including standard instruments such as grasping forceps (e.g., KARL STORZ CLICKline). Both systems are torque-controlled at the joint level [156], [157]; therefore, they form a redundant robotic system with a total of 8 DoF, which can be modeled according to the standard Lagrangian formulation as:

$$\boldsymbol{M}(\boldsymbol{q})\,\ddot{\boldsymbol{q}} + \boldsymbol{C}(\boldsymbol{q},\dot{\boldsymbol{q}})\,\dot{\boldsymbol{q}} + \boldsymbol{g}(\boldsymbol{q}) = \boldsymbol{\tau} + \boldsymbol{\tau}_{ext}, \tag{7.12}$$

where $\boldsymbol{q} \in \mathbb{R}^8$ denotes the vector of joint coordinates, $\boldsymbol{M}(\boldsymbol{q})$ is the inertia matrix, $\boldsymbol{C}(\boldsymbol{q}, \dot{\boldsymbol{q}})$ collects Coriolis and centrifugal terms, $\boldsymbol{g}(\boldsymbol{q})$ represents the gravity contribution, $\boldsymbol{\tau}$ is the vector of joint torques, and $\boldsymbol{\tau}_{ext}$ accounts for external torques induced by interaction forces with both environment and user.

A hierarchical impedance control structure with three levels, inspired by [158], has been implemented, commanding the desired joint torques:

$$\boldsymbol{\tau}^{\star} = \boldsymbol{g}(\boldsymbol{q}) + \boldsymbol{\tau}_{tp} + \boldsymbol{N}_{tp}\boldsymbol{\tau}_{tcp} + \boldsymbol{N}_{tp}\boldsymbol{N}_{tcp}\boldsymbol{\tau}_{j_3} \tag{7.13}$$

where

$$\boldsymbol{\tau}_{tp} = \boldsymbol{J}_{tp}^{\top}\left(\boldsymbol{K}_p\,\tilde{\boldsymbol{r}}_{tp} + \boldsymbol{K}_d\,\dot{\tilde{\boldsymbol{r}}}_{tp}\right), \tag{7.14}$$

$$\boldsymbol{\tau}_{tcp} = \boldsymbol{J}_{tcp}^{\top}\,\boldsymbol{f}_{ve}. \tag{7.15}$$

Here, $\tilde{\boldsymbol{r}}_{tp} = \boldsymbol{r}_{tp} - \boldsymbol{r}_{tp,d}$, where $\boldsymbol{r}_{tp} = [\,\boldsymbol{x}_{tp}^{\top}, \varphi_{tp}\,]^{\top} = \boldsymbol{f}_{tp}(\boldsymbol{q})$ denotes the coordinates of the trocar point, including the position $\boldsymbol{x}_{tp}$ and the rotation angle φ_{tp} about the tool z-axis. The task Jacobian is computed as $\boldsymbol{J}_{tp}(\boldsymbol{q}) = \frac{\partial \boldsymbol{f}_{tp}(\boldsymbol{q})}{\partial \boldsymbol{q}}$, and $\boldsymbol{K}_p = \mathrm{diag}\{k_t, k_t, k_t, k_r\}$, with the translational stiffness $k_t = 2000\frac{N}{m}$ and rotational stiffness $k_r = 50\frac{Nm}{rad}$. The damping matrix $\boldsymbol{K}_d$ is obtained by the double-diagonalisation design based on [159] with a damping ratio of $\xi = 0.7$. Matrix $\boldsymbol{J}_{tcp}(\boldsymbol{q})$ is the Jacobian related to the tool center point position $\boldsymbol{x}$. Finally, the torque null-space projectors $\boldsymbol{N}_{tp}$ and $\boldsymbol{N}_{tcp}$ are computed using the dynamically consistent formulation.

In conclusion, apart from gravity compensation, the first priority level in (7.14) enforces the fulcrum constraint at the trocar point (TP). The second priority level, given by (7.15), provides the interface for applying the viscoelastic force $\boldsymbol{f}_{ve}$, enforcing the virtual fixture at the tip of the instrument. Finally, the redundancy of the MIRO robot is resolved through a joint impedance control $\boldsymbol{\tau}_{j_3}$ applied to joint 3. With this impedance-based formulation, the robot behaves as a transparent interface: in the absence of VF forces, the user perceives the instrument behavior as that of a conventional free-floating laparoscopic tool constrained only by the trocar, without significant resistance from the robotic structure.

A phantom of an insufflated abdomen was positioned on an Operating Room (OR) table. To maintain a standardized endoscope position for every participant, a SOLOASSIST$^{\text{II}}$ robotic camera control was used to hold the stereoscopic endoscope used for the study. The endoscopic video stream was displayed on a standard stereoscopic display positioned on the OR table. For the specific vali-

dation purposes of this study, instead of using an actual surgical tool, a custom tool was designed by attaching a permanent marker to the instrument tip. This allowed converting a surgical task into a path-following drawing task on a flat surface (Fig. 7.1). Additionally, a foot pedal was integrated into the setup to allow the user to voluntarily enable robot control and initiate task execution safely. Finally, to estimate user intention and modulate the constraint, a Myo Armband was attached to the user's dominant arm.

7.4.3 Experimental Task and Design

Guidance Virtual Fixtures hold significant potential for assisting in complex R&D tasks. To validate the proposed control architecture in a representative yet standardized scenario, we selected a benchmark that demands both high continuous path-following precision and the ability to handle sharp directional changes. Therefore, the experimental task was adapted from the cutting exercises of the Fundamentals of Laparoscopic Surgery and the *'Triangle Cut'* exercise of the Lübeck Toolbox (LTB) curriculum [160], [161], as well as recent validated robotic training curricula such as *RoSTraC [162]*.

The study followed a within-subjects design [163], where each participant performed the tasks under both experimental conditions. To avoid carry-over effects from the guidance system to the unassisted performance, the Free Motion condition was always presented first to establish a baseline. To mitigate potential learning effects resulting from this fixed order, a dedicated familiarization phase was conducted prior to data collection, allowing participants to practice until they were comfortable with the task dynamics.

To ensure the simplified experimental design remained representative of the real surgical procedure, we identified three fundamental motor elements characteristic of dissection: *continuous cutting*, *discrete "plucking-like" motions*, and the *repositioning* of the tool along the resection line. Consequently, three distinct experimental tasks were defined:

- **Task 1** requires the user to continuously trace the reference curve. Participants were allowed to choose their preferred travel direction to maximize biomechanical comfort. Since the tracking error and the virtual fixture assistance are independent of the motion direction, this degree of freedom does not introduce a confounding variable.

- **Task 2** requires the user to mark the center of a set of circular targets distributed clockwise along the path. In this task, the user operates utilizing

the predefined anisotropic constraint, without the need to adapt its size.

- **Task 3** combines elements of Task 1 and Task 2, requiring the user to alternately mark the target centers and connect them by drawing continuous lines. This mimics real surgical scenarios where tools are repositioned to adjust tissue retraction or inspection angles. To execute these transitions, the user must utilize the EMG-based virtual clutch to dynamically (dis-)engage the constraint.

7.4.4 Procedure, Objective and Subjective Measures

A standardized procedure was followed for all participants. Prior to each recording block, participants underwent a dedicated familiarization phase lasting approximately 30 to 60 seconds. During this time, they practiced the specific task dynamics—either free-hand drawing or engaging the EMG-clutch—until they reported feeling comfortable with the system. Subsequently, the actual performance was recorded. In this study, a single trial is defined as the complete execution of one specific task under one condition.

To quantify the system's performance, kinematic and dynamic data were logged during the execution of each task. The primary *objective metrics* defined for the evaluation include:

- *Tracking Error:* defined as the deviation between the TCP position and the reference path when touching the paper. Specifically, for Task 2 and 3, the error component binormal to the path ($\tilde{\boldsymbol{x}}_{\boldsymbol{b}}$) is analyzed to assess targeting precision.

- *Interaction Forces:* the forces $\boldsymbol{f}_{\boldsymbol{h}}$ exerted by the user are recorded to evaluate physical effort and the transparency of the assistance.

For *subjective evaluation*, participants were asked to complete the NASA Task Load Index (NASA-TLX) questionnaire [139] at the end of each trial, to assess their perceived workload. This ensures that the workload evaluation reflects the immediate perception of each specific task, thereby minimizing recall bias. The tasks were presented to all participants in the same fixed sequence. Once all tasks were completed, each user was asked to fill in the System Usability Scale (SUS) questionnaire [164]. This combination of objective and subjective evaluations allowed for a comprehensive analysis of both system performance and user experience.

Statistical Analysis

Statistical methods were selected based on data distribution, verified via Shapiro-Wilk tests. For objective metrics, due to the limited sample size ($N = 7$) and deviations from normality observed in specific experimental conditions and paired differences, a non-parametric Wilcoxon signed-rank test was consistently employed for all pairwise comparisons. In contrast, subjective workload ratings (NASA-TLX) were analyzed using Linear Mixed Model (LMM) to accommodate the 2×3 factorial design, after confirming that model residuals followed a normal distribution ($p > 0.05$). The model included *Condition* and *Task* (and their interaction) as fixed effects, while *Subject* was modeled as a random intercept. This structure accounts for subject-specific baselines and rating variability, ensuring robust estimates despite the small sample size [165]. Additionally, SUS scores exhibited a normal distribution ($p = 0.32$), justifying the use of descriptive mean statistics. Significance levels were determined using Type III F-tests for LMMs and standard p-values for Wilcoxon tests. All reported p-values are two-tailed with a significance threshold of $\alpha < 0.05$.

7.5 Experimental Results and Discussion

Given the distinct nature of the experimental tasks, results are presented and immediately discussed within their specific context to facilitate interpretation.

7.5.1 Objective Evaluation

This section presents the performance metrics evaluated during the execution of the tasks described in Section 7.4.

Task 1 - Continuous Tracking

We assessed tracking performance by computing the deviation between the actual TCP position $\boldsymbol{x}$ and reference trajectory $\boldsymbol{x_d}$ in the xy-plane. Since $\boldsymbol{x_d}$ was generated via Kinesthetic Teaching using the robot kinematics, this metric directly quantifies the user's adherence to the intended path.

Figure 7.5(a) displays the distribution of the pointwise position error for Task 1. As illustrated, the application of the VF led to a significant reduction in tracking error ($p < 0.05$), with an average decrease of 27.7% compared to the free motion condition.

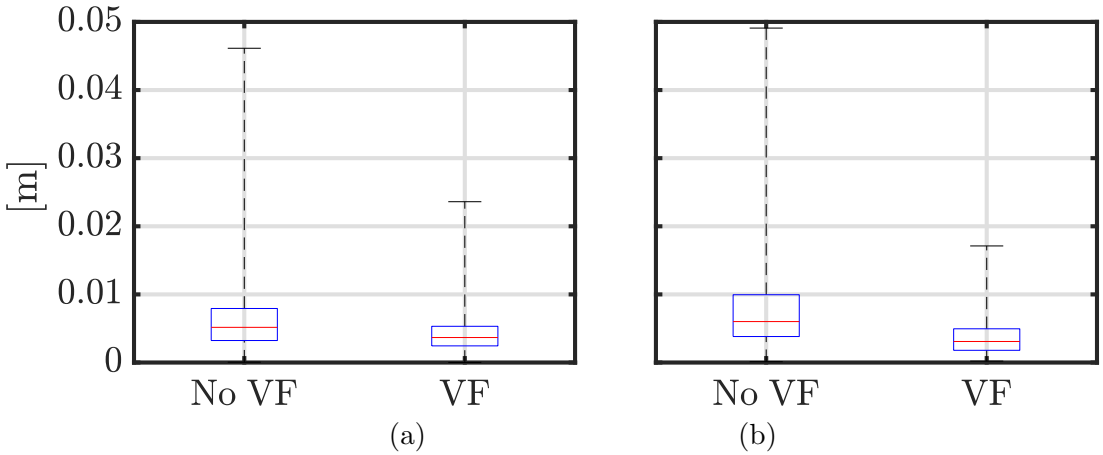

Figure 7.5: Deviation with respect to the reference path, obtained during the execution of (a) Task 1 and (b) Task 3.

Since Task 3 combines elements derived from both Task 1 and Task 2, we evaluated the same positional error metric for the path-following segments of Task 3 (Fig. 7.5(b)) to assess the effectiveness of the VF in this more complex scenario. Notably, the reduction in position error achieved through the use of the Virtual Fixture is even more pronounced in Task 3 than in Task 1. This improvement was found to be statistically significant, yielding the maximum possible test statistic for this sample size ($p < 0.05$). On average, the constrained condition resulted in an improvement of 50.3% compared to the free motion condition.

This enhanced performance is attributable to the hybrid nature of Task 3. Unlike Task 1, which allows the user to maintain a continuous motion state and benefit from short-term adaptation to the path dynamics, Task 3 imposes frequent *task-switching*. These interruptions prevent the user from settling into a steady tracking rhythm, making the stabilization provided by the VF crucial to compensate for the cognitive and motor overhead during transitions.

Task 2 - Discrete Target Reaching

To assess the precision in reaching the predefined targets, the analyzed metric is defined as the position error $\tilde{x}_b$ from the target center along $\boldsymbol{e_b}$. As shown in Fig. 7.6(a), the VF condition resulted in a notable performance improvement in Task 2, producing a reduction of 30.1% in the binormal error component. Although the statistical analysis did not reach the significance threshold ($p = 0.109$), the substantial effect size indicates a clear trend toward improved precision.

Specifically, for $\tilde{x}_b$, the Interquartile Range (IQR) decreased from 0.0017 m to 0.0011 m, marking a 34.6% reduction. This result indicates a substantial im-

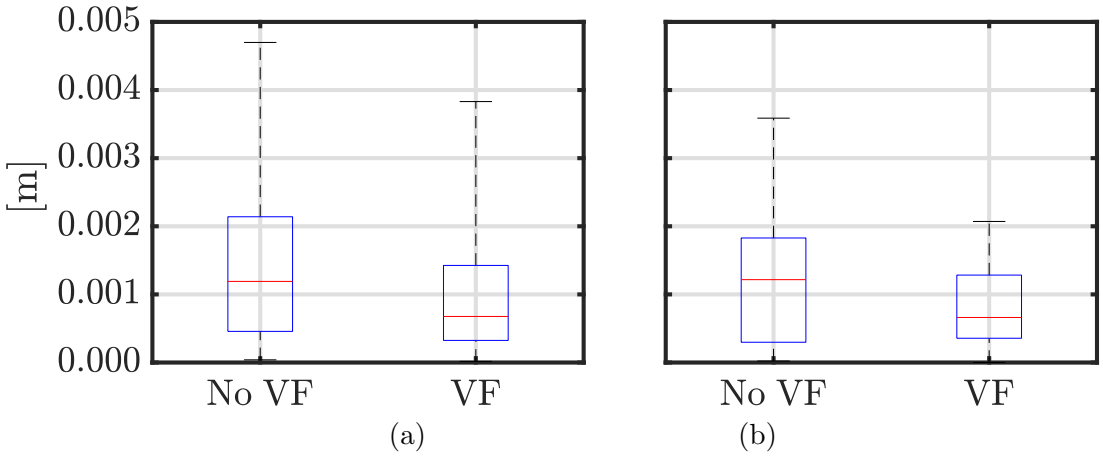

Figure 7.6: Boxplots of the binormal component of the position error $\tilde{x}_b$ in (a) Task 2 and (b) Task 3.

provement in execution consistency and repeatability when using the assistance. This reduction in variability suggests that the lack of statistical significance in the mean comparison may be attributed to the limited sample size rather than a lack of system efficacy. These results confirm that the VF not only mitigates the error magnitude but also improves the consistency of the user's behavior across trials, especially in the direction orthogonal to the reference path where the constraint is most effective.

Results for the targeting subtasks within Task 3, collected in Fig. 7.6(b), mirror the trends observed in Task 2. The VF condition yielded a 29.8% reduction in mean error and a 39.4% reduction in IQR. Crucially, in this scenario involving task-switching, statistical analysis confirmed that the improvement in accuracy is significant ($p < 0.05$). This reinforces the finding that the VF provides robust assistance particularly when the cognitive and motor demand increases.

Task 3 - Constraint Size Adaptation

We evaluated the effectiveness of the EMG-based adaptation mechanism. In this task, users were required to temporarily *disengage* the constraint to transition between targets and *re-engage* it for the continuous tracing segments.

The temporal alignment of the EMG activation peaks and the corresponding drop in constraint force (Fig. 7.7(b)) demonstrates the correct functionality of the proposed adaptation method. Specifically, whenever the EMG signal $\gamma(t)$ exceeds the threshold $\bar{\gamma}$, the virtual clutch triggers the *disengaged state*, forcing the constraint force to null and allowing free repositioning. Conversely, as the signal drops, the clutch *re-engages*. Notably, during the subsequent approach towards

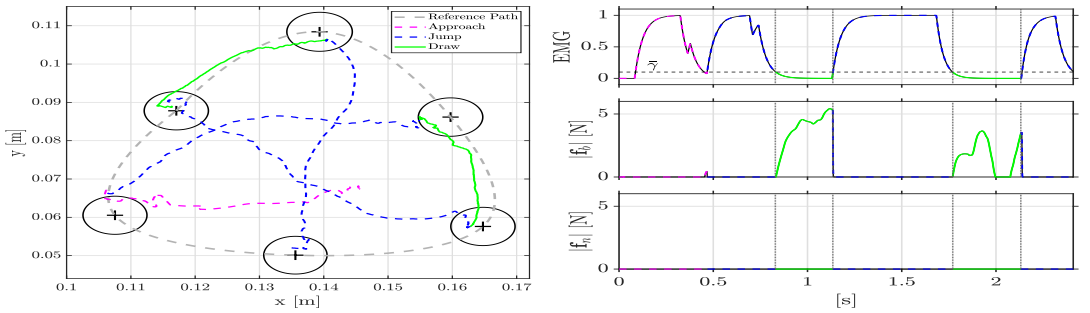

(a) (b)

Figure 7.7: Analysis of Task 3 execution. (a) Trajectory followed by the TCP, highlighting transitions between constrained and unconstrained segments. (b) VF normal and binormal forces vs. the user's EMG signal and system activation.

the reference path, the user perceives no resistive force despite the constraint being active, ensuring a smooth re-entry. During the tracking phase, the force is primarily exerted along $\boldsymbol{e_b}$, consistent with the intended guidance geometry.

To assess the physical burden of this interaction, we compared the average user-applied forces along the normal ($\boldsymbol{f_{h,n}}$) and binormal ($\boldsymbol{f_{h,b}}$) directions across the entire population (Table 7.1). Here, $\boldsymbol{f_h}$ denotes the vector of interaction forces estimated from joint torque measurements [166], expressed in the workspace reference frame.

Statistical analysis revealed two distinct behaviors consistent with the anisotropic design of the virtual fixture. For the *normal* component, corresponding to the direction of allowed motion, no significant difference was found ($p > 0.05$), confirming that the assistance remains perfectly transparent where the user is intended to move freely. Conversely, for the *binormal* component, which aligns with the stricter constraint boundaries, a statistically significant increase in interaction force was observed ($p < 0.05$), reflecting the active corrective action of the fixture against deviations.

This indicates that users actively utilized the constraint boundary for stabilization orthogonal to the path. However, as the absolute force magnitude remains below 1 N, this interaction reflects helpful guidance rather than resistive burden. Overall, this lack of significant force increase combined with the low absolute values indicates that the assistance is transparent: the user accepts the guidance during tracking and, crucially, the virtual clutch disengages sufficiently fast during transitions to prevent the user from having to overcome resistive forces to break free.

Table 7.1: Average user-applied forces along constraint directions

Condition	$\lvert f_{h,n} \rvert$ [N]	$\lvert f_{h,b} \rvert$ [N]
No VF	0.817	0.696
VF	0.868	0.848

7.5.2 Subjective Evaluation

This section reports the users' perception of the system. We analyzed the workload for each specific task using the NASA-TLX questionnaire, specifically focusing on *mental demand*, *physical demand*, *effort*, and *frustration*. These dimensions were selected as they directly reflect the cognitive and physical challenges, as well as the overall perceived difficulty and stress associated with the task execution under both experimental conditions. Finally, the overall system usability was assessed via the SUS questionnaire.

NASA-TLX

Fig. 7.8 summarizes the subjective workload ratings reported by participants. The LMM analysis revealed a significant main effect of the experimental *Condition* across the key cognitive metrics. Specifically, the use of Virtual Fixtures significantly reduced *Mental Demand* ($F(1, 36) = 6.23, p < 0.05$), *Effort* ($F(1, 36) = 16.15, p < 0.05$), and *Frustration* ($F(1, 36) = 20.47, p < 0.05$).

Conversely, no significant main effect was found for *Physical Demand* ($F(1, 36) = 3.32, p > 0.05$). This subjective perception aligns with the objective interaction force data reported in Table 7.1, suggesting that the active guidance did not result in a statistically significant increase in physical demand, thereby preserving the system's transparency.

Furthermore, no significant interaction effects between *Task* and *Condition* were observed for any of the metrics ($p > 0.05$). This indicates that the beneficial impact of VFs is consistent across different levels of task complexity.

As shown in Fig. 7.8(b), in the absence of guidance, metrics such as *Mental Demand* and *Frustration* were notably higher and exhibited greater variability, particularly in Task 3. The activation of the VF not only lowered the absolute scores but also homogenized the user experience.

Since *Physical Demand* remained unchanged, the significant reduction in *Effort* can be primarily attributed to the lowered cognitive burden, confirming that the virtual constraint allows users to achieve task goals with significantly lower overall exertion.

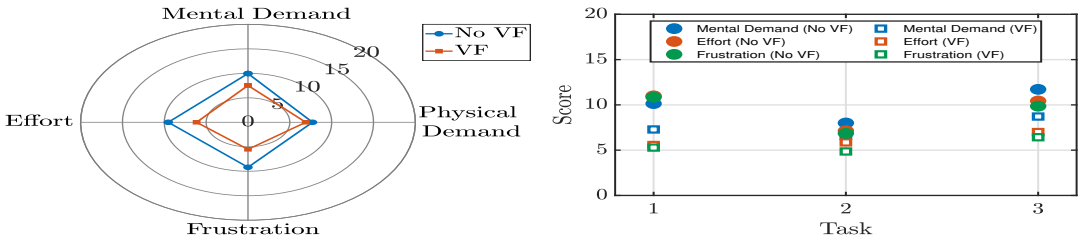

(a) (b)

Figure 7.8: (a) Subjective evaluation scores from NASA-TLX. (b) Estimated marginal means of NASA-TLX scores for the statistically significant dimensions ($p < 0.05$).

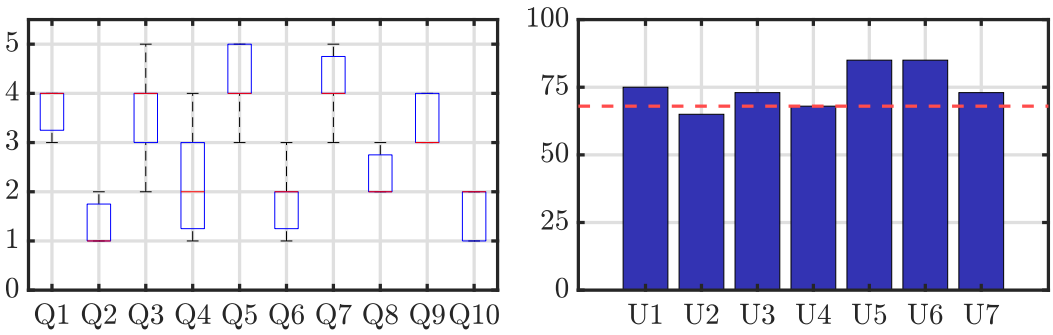

(a) (b)

Figure 7.9: System Usability Scale results. (a) Questionwise distribution of scores. The items correspond to the standard SUS questions [164]. (b) Total SUS scores for each participant.

System Usability Scale

Finally, the overall usability of the proposed assistance system was assessed via the System Usability Scale (SUS) [164]. This standardized questionnaire was administered as a summative evaluation at the end of the experimental session to provide a global measure of subjective usability (scaled 0-100), quantifying perceived ease of use and learnability.

The SUS scores averaged 74.6, exceeding the commonly accepted benchmark of 68 [167]. Most participants rated the system positively, with Users 5 and 6 reaching excellent levels (SUS = 85). Only User 2 scored slightly below the benchmark (SUS = 65). However, given the high consistency among the other participants and the contradictory responses within User 2's questionnaire, this case can be considered an outlier related to individual confidence rather than a reflection of system usability issues.

Retrospective Power Analysis

Given the relatively small sample size ($N = 7$) employed in the experimental validation, a retrospective power analysis was conducted ($\alpha = 0.05$) to mathematically assess the robustness of the findings and contextualize the pilot nature of the study. The analysis revealed that for basic operations, such as continuous tracking (Task 1) and static targeting (Task 2), the virtual fixture yielded moderate-to-large effect sizes ($d = 0.81$ and $d = 0.65$, respectively). Due to the limited sample size, these metrics achieved inadequate statistical power (43.4% and 31.0%). However, the system's efficacy became overwhelmingly evident in the highly demanding hybrid scenario (Task 3). In this context, the assistance on the continuous tracking error yielded a massive effect size of $d = 2.27$, effectively bringing the statistical power to 99.8%. Similarly, targeting accuracy and binormal interaction forces in Task 3 exhibited large effect sizes ($d = 1.07$ and $d = 1.10$), achieving power levels approaching 70%. This formally confirms that the kinematic validation of the control algorithm is statistically robust exactly where the cognitive and motor demands are highest. Regarding the *subjective human-factors evaluations*, the NASA-TLX results for Task 3 perfectly mirrored the objective data. The significant reductions in perceived Effort and Frustration generated huge effect sizes ($d = 1.27$ and $d = 1.33$), yielding robust power levels of 79.9% and 83.4%, respectively. Mental Demand, conversely, yielded a lower power (51.9%). While the core kinematic tracking and primary workload mitigations successfully achieved standard power thresholds ($\approx 80\%$), the sub-optimal power on dynamic interactions and secondary cognitive metrics mathematically highlights the susceptibility of these parameters to high inter-subject variability. This structural inability to reliably generalize all moderate usability trends (including the global SUS score) without high variance formally categorizes the human-factors assessment as a *pilot study*. Consequently, larger-scale clinical trials are strictly required to confidently confirm the overall usability trends and generalize these subjective interaction profiles to a broader population of surgeons.

7.5.3 Overall Discussion

The findings presented above confirm our hypothesis and positively validate the intended efficacy of the EMG-based adaptive Virtual Fixture. The alignment between objective performance metrics and subjective feedback demonstrates that the proposed assistance method significantly improves task execution compared

to free motion.

Specifically, being able to utilize the guidance VF leads to demonstrably lower tracking errors and higher movement consistency. By confining the tool motion within a safe corridor, the system implicitly addresses the critical safety requirement of limiting penetration depth, preventing accidental damage to underlying structures during blind cutting phases. The lower NASA-TLX scores and high SUS ratings indicate a substantial reduction in perceived workload, which could facilitate efficient tissue manipulation in complex surgical tasks.

A cross-task comparison reveals that these benefits are most pronounced in Task 3. Unlike the single-task scenarios, Task 3 imposes a cognitive overhead due to frequent switching between tracking and targeting. The fact that the VF induces the highest relative improvement in this hybrid task confirms that the assistance becomes increasingly critical as dynamic demands rise.

Although the proposed application shows promising results, it is crucial to address the limitations encountered. First, the validation was conducted on a simplified drawing task rather than actual tissue dissection, which excludes factors such as tissue deformation and bleeding. It is crucial to note that the proposed proxy-based framework, while highly effective for static environments, relies on the assumption of structural rigidity after the definition of the path $\boldsymbol{\varphi}(s)$. In scenarios involving soft tissues, anatomical deformations, physiological motions, or organ shifts induce a time-varying discrepancy between the statically defined virtual fixture and the actual surgical target. If the target moves away from the predefined path, the surgeon is forced to actively override the guidance to reach the new correct position, thereby increasing both the cognitive load and the interaction forces. Consequently, the reliance on *a priori* paths defined via Kinesthetic Teaching represents a boundary condition for the current control architecture. Second, the pilot study involved a limited sample size of novice users. While this choice was appropriate for assessing the initial intuitiveness of the interface, evaluating the system with experienced surgeons in a realistic clinical simulation will be crucial to confirm its efficacy in professional practice.

7.6 Conclusion

In this work, we presented a novel control framework for robot-assisted surgery that leverages the user's muscle contraction signals to intuitively adapt Virtual Fixtures. By introducing an EMG-based *virtual clutch*, the proposed system allows seamless transitions between precise guidance and free motion, addressing

the specific dynamic requirements of R&D tasks.

The pilot user study confirmed the effectiveness of this human-in-the-loop approach. The results demonstrated that the adaptive assistance significantly enhances tracking precision and movement consistency without imposing additional physical effort. Crucially, the system proved capable of mitigating the cognitive load associated with complex task-switching, validating the transparency and intuitiveness of the interface.

Finally, from a dynamic stability perspective, it is important to contextualize the performance of the EMG-controlled virtual clutch within the theoretical boundaries established in Chapter 5. A critical question is whether the rapid (dis-)engagement of the constraints approached the instability regions characterized by limit cycles. During the experimental validation in this chapter, the core admittance parameters governing the virtual mass dynamics (m, b) were conservatively tuned to remain well within the stable region, intentionally avoiding the critical thresholds where system delays and actuator saturation induce persistent oscillations. To achieve the required transparency during the free-motion phases, the proposed virtual clutch did not dangerously reduce the viscous-inertial parameters; rather, it dynamically modulated the geometric boundaries of the deadzone (δ_n, δ_b). Consequently, the rapid mode transitions did not excite unmodeled high-frequency dynamics, and no limit cycles were observed during the user study. This confirms that modulating the spatial constraint geometry via EMG serves as a robust and stable alternative to pure parameter adaptation, allowing seamless transitions between guided and free motion without threatening the coupled system's stability.

Future research will focus on validating these findings with expert surgeons in realistic clinical scenarios. To address the limitations associated with static paths in deformable anatomies, a critical future direction involves the evolution of the proposed framework into *Dynamic Virtual Fixtures*. By integrating real-time intra-operative sensory feedback—such as stereoscopic endoscopic vision or depth-sensing cameras—coupled with non-rigid registration algorithms, the system could continuously estimate the tissue deformation field. This would allow the control architecture to dynamically update the reference curve in real-time, enabling the virtual fixture to warp, translate, and move in unison with the pulsating anatomy. Beyond the current explicit control, we aim to advance the system's autonomy by integrating multi-modal data (e.g., gaze tracking and instrument kinematics). This will enable the development of a context-aware controller capable of autonomously recognizing surgical phases and adapting the assistance level

to the surgeon's intent, paving the way for intelligent and collaborative surgical robotics.

Chapter 8

Conclusion and Future Directions

This dissertation has presented a comprehensive research effort aimed at enhancing physical Human-Robot Interaction (pHRI) in medical robotics. Motivated by the need to bridge the gap between the precision of autonomous robots and the decision-making capabilities of human operators, this work has developed a unified control framework based on Virtual Fixtures. By integrating intuitive task definition methods, rigorous stability analyses, and adaptive control strategies, the proposed architecture has been successfully applied to two distinct yet complementary domains: upper-limb rehabilitation and robot-assisted surgery.

8.1 Summary of Main Contributions

The research path followed in this thesis allows us to draw several key conclusions regarding the design and control of collaborative robots in healthcare:

8.1.1 Methodological Foundations

The adoption of the Spatial Sampling Algorithm (SSA) (Chapter 3) proved to be a critical enabler for robust human-in-the-loop control. By decoupling the geometric definition of the task from its temporal execution, we overcame the limitations of time-dependent trajectory tracking. This approach resolved the "stagnation phenomenon" often encountered in admittance control when users pause or hesitate, ensuring that the guidance remains consistent regardless of the execution speed.

8.1.2 Theoretical Reliability

Safety is the non-negotiable prerequisite for medical robotics. The theoretical analysis in Chapter 4 provided the formal certification of the framework's stability. Using Lyapunov theory and the framework of dissipative systems, we demon-

strated that the coupled human-robot system remains asymptotically stable even in the presence of kinematic redundancy. Furthermore, the investigation into non-ideal operating conditions (Chapter 5)—such as time delays and actuator saturation—highlighted the practical stability boundaries, providing guidelines for tuning the admittance parameters (m, b) to maximize transparency without compromising safety.

8.1.3 Versatility in Rehabilitation

In the domain of rehabilitation (Chapter 6), the framework demonstrated remarkable versatility. The introduction of a novel workspace optimization method based on a *payload index* ensured that commercial cobots could be effectively deployed for weight-bearing exercises. The experimental validation confirmed that the proposed Hybrid Impedance Control allows for a seamless transition between passive assistance and active participation. The ability to modulate the virtual channel's stiffness (χ) and size (δ) proved effective in adapting the task difficulty, a crucial feature for promoting neuroplasticity and patient engagement.

8.1.4 Adaptivity in Surgery

In the surgical domain (Chapter 7), the framework evolved from static guidance to dynamic assistance. The development of an anisotropic virtual fixture combined with an Electromyography (EMG)-based interface introduced a novel "Virtual Clutch" mechanism. This allowed the system to infer the surgeon's intent in real-time, enabling dynamic switching between high-precision guidance for dissection and free motion for repositioning. The user study confirmed that this adaptive approach significantly reduces cognitive load and frustration compared to rigid guidance or free-hand execution.

8.2 Limitations and Open Challenges

Despite the promising results, this research is not without limitations, which must be acknowledged to contextualize the findings:

- **Clinical Validation and Human Passivity:** The experimental validation in both rehabilitation and surgery was conducted with healthy participants or on phantom models. While these studies provided necessary proof-of-concept data and usability metrics, they do not fully capture the

complexities of interacting with patients suffering from motor impairments or the unpredictable nature of live biological tissue. Crucially, the formal stability guarantees of the proposed control framework (detailed in Chapter 4) rely on the fundamental assumption of human passivity. It must be explicitly stated that this assumption may not hold true for patients with active movement disorders. Neurologically impaired patients often exhibit non-passive motor control strategies, such as involuntary spasticity, clonus, or high-frequency tremors, which can actively inject energy into the control loop. These uncontrolled active inputs could interact adversely with the proposed admittance parameters; for instance, high-frequency tremors could excite the system if the virtual mass (m) and damping (b) are tuned for high transparency, potentially leading to coupled instability.

To address this limitation, future iterations of the framework must be adapted to detect and safely react to non-passive human inputs. A primary strategy involves integrating real-time energy observers to continuously monitor the power flow at the human-robot interface. Building upon this, Time-Domain Passivity Controllers or Energy Tank architectures could be implemented. The Energy Tank approach is particularly promising for this domain: it allows the system to accumulate energy dissipated during stable interaction phases and utilize this stored energy to safely manage active energy injections. Upon detecting the onset of a spasm, the system could exploit the tank to dynamically adapt the admittance parameters—such as rapidly increasing the virtual damping (b) to absorb the excess energy—thus preserving coupled stability without permanently degrading the transparency of the robotic assistance. Furthermore, the EMG-based interface proposed in Chapter 7 could be extended to preemptively recognize pathological muscle co-activations, allowing the controller to filter out tremors or adapt its response before the kinematic perturbation is fully transferred to the robot.

- **Sample Size and Statistical Generalizability:** The user studies presented in Chapter 6 and Chapter 7 were conducted with relatively small sample sizes ($N = 10$ and $N = 7$, respectively). While statistically significant differences ($p < 0.05$) were successfully achieved for both objective performance metrics and specific subjective workload assessments (NASA-TLX, SUS), the generalizability of these results to a broader population remains statistically fragile. These experiments must therefore be interpreted

strictly as *pilot studies* aimed at validating the technical feasibility, safety, and initial usability of the proposed control architectures. As detailed in the retrospective power analyses (Sections 6.6.2 and 7.5.2) explicitly conducted for these tests, the effect sizes for the primary kinematic tracking metrics across both applications were massive ($d > 2.0$), guaranteeing a statistical power approaching 100% that mathematically validates the control robustness. Similarly, major perceptual shifts (e.g., reduction in perceived Effort) achieved robust statistical power ($80\% - 93\%$). However, the analyses also revealed that dynamic interactions (e.g., interaction forces) and secondary cognitive metrics frequently deal with moderate effect sizes, for which samples of $N \leq 10$ provide inadequate power (often $< 70\%$). Consequently, to robustly confirm these overall usability trends and ensure a standard statistical power of $1 - \beta = 0.80$ across all dynamic and human-factors metrics, future larger-scale clinical trials involving diverse demographic groups and expert medical professionals are strictly required.

- **Sensing Complexity:** The surgical application relies on surface EMG, which requires careful calibration and electrode placement. In a real operating room, issues such as sweat, electrical noise, or sterile draping could affect signal reliability.

- **Model Dependency:** The generation of virtual fixtures currently relies on kinematic demonstrations. In scenarios with significant tissue deformation (e.g., soft tissue surgery), a geometric path recorded *a priori* might become invalid, requiring real-time registration methods that were not integrated into this specific implementation.

8.3 Future Research Perspectives

The framework established in this thesis lays the groundwork for several future research directions:

8.3.1 Towards Clinical Trials

The natural next step is the translation of these technologies into clinical trials. For rehabilitation, this involves testing the system with stroke survivors to assess the therapeutic efficacy of the adaptive assistance modes. For surgery, *ex-vivo*

and *in-vivo* animal studies are necessary to validate the utility of the EMG-based clutch in realistic dissection scenarios involving bleeding and tissue dynamics.

8.3.2 Multimodal Intention Detection

While this work successfully utilized EMG for explicit intent detection (clutching), future iterations could explore *implicit* intention estimation. By fusing EMG data with gaze tracking and force/torque patterns, the system could predict the surgeon's next move or the patient's fatigue level without requiring explicit muscle contractions, making the interaction even more seamless.

8.3.3 Augmented Reality for Visual-Haptic Guidance

A fundamental limitation of purely haptic Virtual Fixtures is their inherent "invisibility". Currently, operators must often interact physically with the robot and rely on reactive force feedback to discover the boundaries of a constrained channel or the limits of a forbidden region. A highly promising future direction is the integration of visual feedback through Augmented Reality (AR) headsets (e.g., Microsoft HoloLens or Apple Vision Pro). Projecting the geometric intent—such as the desired trajectory, the safety boundaries, or the real-time payload maps—directly into the user's field of view would drastically reduce the cognitive load. By combining the robust admittance control developed in this thesis with predictive visual cues, the system would transition from purely reactive haptic guidance to a fully intuitive, visual-haptic multimodal collaboration.

8.3.4 AI-Driven Parameter Tuning

Currently, the control parameters (e.g., stiffness χ, damping b) are tuned based on theoretical stability margins or manual selection. Future research could investigate the use of Reinforcement Learning (RL) to automatically tune these parameters in real-time, optimizing the trade-off between stability and transparency based on the specific user's behavior and the current task phase.

8.4 Final Remarks

In conclusion, this thesis has demonstrated that a unified control architecture, rooted in rigorous stability theory but designed for flexibility, can effectively address the diverse challenges of medical robotics. By placing the human at the

center of the control loop—whether a patient relearning to move or a surgeon performing a delicate procedure—the proposed technologies represent a concrete step towards safer, more intuitive, and more effective robot-assisted healthcare.

Acknowledgements

Il dottorato è stato un'esperienza sicuramente piena di alti e bassi. Mi sono iscritto con grandi dubbi sulla scelta fatta e sono arrivato al terzo anno, arricchito dall'esperienza al DLR, che ritengo una delle più gratificanti della mia "carriera". Sicuramente non è stata una passeggiata, ma col senno di poi la rifarei. Di certo, non sarei stato in grado di percorrere questa strada da solo; approfitto quindi della stesura di questa tesi per ringraziare le persone senza il cui supporto non sarebbe stato possibile concludere questo percorso.

Innanzitutto, vorrei ringraziare il mio supervisore, *Luigi*. Fin dai tempi della tesi magistrale, è stato lui a introdurmi e guidarmi nel mondo della robotica. Non dimenticherò mai quando, in seguito a un incidente che ha causato la deformazione dei sensori di coppia ai giunti del robot, mi ha aiutato personalmente a trovare una soluzione per compensare i problemi hardware, salvando i miei esperimenti e permettendomi di andare avanti.

Un ringraziamento speciale va ai miei colleghi e amici dell'Università di Modena e Reggio Emilia, in particolare ai gruppi *AutoLab* e *Ideativa*. A *Davide*, per la collaborazione e le discussioni di questi anni. A *Giovanni*, per la collaborazione ma soprattutto per la vita condivisa fuori dal laboratorio: per la scoperta di Carlos Moreno, per la gita a Monaco e, soprattutto, per il concerto del maestro BelloFigo. Una menzione particolare va a "mamma" *Elisa*, per aver condiviso quotidianamente con me tutte le gioie e i dolori di questo percorso di dottorato indipendentemente dalla posizione geografica. Voglio ringraziare anche *Matteo*, *Niccolò* e *Federico* per aver contribuito a creare un ambiente di lavoro stimolante e piacevole.

Il mio sincero apprezzamento va all'*Institute of Robotics and Mechatronics del German Aerospace Center (DLR)* a Wessling. Il mio periodo di ricerca lì è stato un momento determinante del mio dottorato. Sono in debito con *Julian* per avermi dato l'opportunità di lavorare su piattaforme chirurgiche così avanzate e per la sua supervisione. Ricordo ancora quella domenica passata a lavorare insieme al progetto e il Döner che abbiamo condiviso quel giorno. Vorrei esprimere un ringraziamento speciale anche a *Michael*. Grazie per avermi aiutato con l'implementazione del codice, l'esecuzione dei test e la realizzazione dei

video. Ma soprattutto, grazie per i pranzi insieme, le passeggiate subito dopo e per avermi fatto iniziare *The Office*.

Infine, il ringraziamento più importante va a coloro che mi hanno sostenuto fuori dal laboratorio. A mamma e papà, che sono sempre stati al mio fianco per sostenermi e incoraggiare le mie iniziative, credendo ciecamente in me e nelle mie capacità anche quando nemmeno per me la strada era chiara. Ringrazio Alberto, che, nonostante le imprevedibilità della vita, trova sempre tempo per condividere con me interessi e passioni che negli anni non sono mai cambiati.

Ringrazio i miei amici *Nicolas* e *Duccio*, che insieme a me hanno condiviso la (dis-)avventura del dottorato, anche se in ambiti e dipartimenti differenti.

Ringrazio i miei amici di Rubiera, i "reduci" dello Zanelli e le vecchie glorie dell'Università. Grazie per avermi ricordato in questi anni che nella vita c'è molto di più oltre a MATLAB e LaTeX.

Un grazie davvero speciale va a *Roberta*. Grazie per aver sopportato le mie crisi esistenziali e i miei complessi, e per avermi raggiunto fino in Germania durante il mio periodo al DLR per farmi sentire a casa. Grazie per avermi aiutato a crescere; grazie a te stiamo riuscendo a diventare "grandi" (o vecchi, se preferisci) inZieme. Sei stata al mio fianco fin dall'inizio e spero, anzi, sono convinto, che ci sarai per sempre.

Ultimo, ma non per importanza, *Giulio*, il mio piccolo adorabile sacco di pulci. Grazie per aver portato peli, graffi e soprattutto gioia a casa nostra.

Appendix A

Mathematical Derivations

In this appendix, the detailed coefficients for the transfer functions used in the stability analysis (Chapter 5) are reported.

A.1 Coefficients of the Control Function $G_c(s)$

The transfer function $G_c(s)$, describing the relationship between the actuator speed and the reference speed, is characterized by the following coefficients:

$$b'_1 = J_t J_{lr} \tag{A.1}$$
$$b'_2 = J_t(D_{el} + K_D J_{lr}) \tag{A.2}$$
$$b'_3 = J_t(K_{el} + K_D D_{el} + K_P J_{lr}) \tag{A.3}$$
$$b'_4 = J_t(K_D K_{el} + K_P D_{el}) \tag{A.4}$$
$$b'_5 = J_t K_P K_{el} \tag{A.5}$$

$$a'_1 = J_{lr} J_m \tag{A.6}$$
$$a'_2 = J_{lr}(D_m + J_t K_D) + D_{el} J_t \tag{A.7}$$
$$a'_3 = J_t(J_{lr} K_P + D_{el} K_D) + J_t K_{el} + D_m D_{el} \tag{A.8}$$
$$a'_4 = K_{el}(D_m + J_t K_D) + D_{el} J_t K_P \tag{A.9}$$
$$a'_5 = K_{el} J_t K_P \tag{A.10}$$

A.2 Coefficients of the Loop Gain Function $G_l(s)$

The coefficients of the numerator (β_i) and denominator (α_i) of the loop gain function $G_l(s)$ are derived as follows:

Numerator Coefficients (β_i)

$$\beta_1 = D_{el} b'_1 b_h \tag{A.11}$$
$$\beta_2 = D_{el}(K_h b'_1 + b'_2 b_h) + K_{el} b'_1 b_h \tag{A.12}$$
$$\beta_3 = D_{el}(K_h b'_2 + b_h b'_3) + K_{el}(K_h b'_1 + b'_2 b_h) \tag{A.13}$$
$$\beta_4 = D_{el}(K_h b'_3 + b_h b'_4) + K_{el}(K_h b'_2 + b_h b'_3) \tag{A.14}$$
$$\beta_5 = D_{el}(K_h b'_4 + b_h b'_5) + K_{el}(K_h b'_3 + b_h b'_4) \tag{A.15}$$
$$\beta_6 = D_{el} K_h b'_5 + K_{el}(K_h b'_4 + b_h b'_5) \tag{A.16}$$
$$\beta_7 = K_{el} K_h b'_5 \tag{A.17}$$

Denominator Coefficients (α_i)

$$\alpha_1 = J_{lr} a'_1 mn \tag{A.18}$$
$$\alpha_2 = J_{lr} n(a'_1 b + a'_2 m) + D_{el} a'_1 mn \tag{A.19}$$
$$\alpha_3 = J_{lr} n(a'_2 b + a'_3 m) + D_{el} n(a'_1 b + a'_2 m) + K_{el} a'_1 mn \tag{A.20}$$
$$\alpha_4 = J_{lr} n(a'_3 b + a'_4 m) + D_{el} n(a'_2 b + a'_3 m) + K_{el} n(a'_1 b + a'_2 m) \tag{A.21}$$
$$\alpha_5 = J_{lr} n(a'_4 b + a'_5 m) + D_{el} n(a'_3 b + a'_4 m) + K_{el} n(a'_2 b + a'_3 m) \tag{A.22}$$
$$\alpha_6 = J_{lr} n a'_5 b + D_{el} n(a'_4 b + a'_5 m) + K_{el} n(a'_3 b + a'_4 m) \tag{A.23}$$
$$\alpha_7 = D_{el} n a'_5 b + K_{el} n(a'_4 b + a'_5 m) \tag{A.24}$$
$$\alpha_8 = K_{el} a'_5 bn \tag{A.25}$$

List of Publications

Accepted/Published Papers

[1] **D. Onfiani**, M. Caramaschi, L. Biagiotti, and F. Pini, "Optimizing Design and Control Methods for Using Collaborative Robots in Upper Limb Rehabilitation," *IEEE/ASME Transactions on Mechatronics*, 2025. (DOI: 10.1109/TMECH.2025.3567128).

[2] D. Tebaldi, **D. Onfiani**, and L. Biagiotti, "On the Analysis of Stability, Sensitivity and Transparency in Variable Admittance Control for pHRI Enhanced by Virtual Fixtures," in *2025 IEEE/RSJ International Conference on Intelligent Robots and Systems (IROS)*, 2025, pp. 16665-16672.

[3] G. Braglia, **D. Onfiani**, D. Tebaldi, A. E. Lazzaretti, and L. Biagiotti, "Spatial Sampling for Alignment of Robot Demonstrated Trajectories in Upper Limb Rehabilitation Tasks," in *8th Conference on Robot Learning (CoRL 2024)*, Workshop on Learning for Caregiving Robots, Munich, Germany, 2024.

[4] M. Caramaschi, **D. Onfiani**, F. Pini, L. Biagiotti, and F. Leali, "Workspace Placement of Motion Trajectories by Manipulability Index for Optimal Design of Cobot Assisted Rehabilitation Solutions," *Computer-Aided Design and Applications*, vol. 20, no. S6, pp. 1–12, 2022.

[5] **D. Onfiani**, M. Caramaschi, L. Biagiotti, and F. Pini, "Path-Constrained Admittance Control of Human-Robot Interaction for Upper Limb Rehabilitation," in *Social Robotics: 13th International Conference (ICSR 2021)*, Springer International Publishing, 2022, pp. 143–153.

In Preparation

[4] **D. Onfiani**, D. Tebaldi, L. Biagiotti, and F. Pini, "A Survey on Virtual Fixtures for Enhancing Human-Robot Interaction,' Submitted to Transaction on Human Machine Systems' 2025.

[5] **D. Onfiani**, M. Dyck, L. Biagiotti, and J. Klodmann, "EMG-Based Adaptation of Anisotropic Virtual Fixtures for Surgical Resection and Dissection,' Submitted to Robotics and Automation Letters ' 2025.

Bibliography

[1] D. Onfiani, D. Tebaldi, and L. Biagiotti, *A survey on virtual fixtures for enhancing human-robot interaction*, Submitted for publication, 2025.

[2] L. B. Rosenberg, "The use of virtual fixtures to enhance operator performance in time delayed teleoperation.", 1993.

[3] S. A. Bowyer, B. L. Davies, and F. Rodriguez y Baena, "Active constraints/virtual fixtures: A survey", *IEEE Transactions on Robotics*, vol. 30, no. 1, pp. 138–157, 2014. DOI: 10.1109/TRO.2013.2283410.

[4] J. J. Abbott, P. Marayong, and A. M. Okamura, "Haptic virtual fixtures for robot-assisted manipulation", in *Robotics Research*, S. Thrun, R. Brooks, and H. Durrant-Whyte, Eds., Berlin, Heidelberg: Springer Berlin Heidelberg, 2007, pp. 49–64, ISBN: 978-3-540-48113-3.

[5] P. Marayong, M. Li, A. M. Okamura, and G. D. Hager, "Spatial motion constraints: Theory and demonstrations for robot guidance using virtual fixtures", in *2003 IEEE International Conference on Robotics and Automation (Cat. No. 03CH37422)*, IEEE, vol. 2, 2003, pp. 1954–1959.

[6] C. Lauretti, F. Cordella, E. Guglielmelli, and L. Zollo, "Learning by demonstration for planning activities of daily living in rehabilitation and assistive robotics", *IEEE Robotics and Automation Letters*, 2017.

[7] H. J. Asl, M. Yamashita, T. Narikiyo, and M. Kawanishi, "Field-based assist-as-needed control schemes for rehabilitation robots", *IEEE/ASME Transactions on Mechatronics*, vol. 25, no. 4, pp. 2100–2111, 2020. DOI: 10.1109/TMECH.2020.2992090.

[8] M. M. Marinho, H. Ishida, K. Harada, K. Deie, and M. Mitsuishi, "Virtual fixture assistance for suturing in robot-aided pediatric endoscopic surgery", *IEEE Robotics and Automation Letters*, vol. 5, no. 2, pp. 524–531, 2020. DOI: 10.1109/LRA.2019.2963642.

[9] M. Li, M. Ishii, and R. H. Taylor, "Spatial motion constraints using virtual fixtures generated by anatomy", *IEEE Transactions on Robotics*, vol. 23, no. 1, pp. 4–19, 2007.

[10] A. Cherubini, R. Passama, A. Crosnier, A. Lasnier, and P. Fraisse, "Collaborative manufacturing with physical human–robot interaction", *Robotics and Computer-Integrated Manufacturing*, vol. 40, pp. 1–13, 2016, ISSN: 0736-5845. DOI: https://doi.org/10.1016/j.rcim.2015.12.007.

[11] D. Sirintuna, T. Kastritsi, I. Ozdamar, J. M. Gandarias, and A. Ajoudani, "Enhancing human–robot collaborative transportation through obstacle-aware vibrotactile warning and virtual fixtures", *Robotics and Autonomous Systems*, vol. 178, p. 104 725, 2024, ISSN: 0921-8890.

[12] F. Ryden and H. J. Chizeck, "Forbidden-region virtual fixtures from streaming point clouds: Remotely touching and protecting a beating heart", in *2012 IEEE/RSJ International Conference on Intelligent Robots and Systems*, IEEE, 2012, pp. 3308–3313.

[13] S. Nia Kosari, F. Rydén, T. S. Lendvay, B. Hannaford, and H. J. Chizeck, "Forbidden region virtual fixtures from streaming point clouds", *Advanced Robotics*, vol. 28, no. 22, pp. 1507–1518, 2014.

[14] S. Moccia et al., "Toward improving safety in neurosurgery with an active handheld instrument", *Annals of biomedical engineering*, vol. 46, pp. 1450–1464, 2018.

[15] V. Villani, F. Pini, F. Leali, and C. Secchi, "Survey on human–robot collaboration in industrial settings: Safety, intuitive interfaces and applications", *Mechatronics*, vol. 55, pp. 248–266, 2018, ISSN: 0957-4158. DOI: https://doi.org/10.1016/j.mechatronics.2018.02.009.

[16] A. Ajoudani, A. M. Zanchettin, S. Ivaldi, A. Albu-Schäffer, K. Kosuge, and O. Khatib, "Progress and prospects of the human–robot collaboration", *Autonomous robots*, vol. 42, no. 5, pp. 957–975, 2018.

[17] N. Hogan, "Impedance control: An approach to manipulation: Part i—theory", *Journal of Dynamic Systems, Measurement, and Control*, vol. 107, no. 1, pp. 1–7, 1985.

[18] N. Diolaiti, G. Niemeyer, F. Barbagli, and J. Salisbury, "Stability of haptic rendering: Discretization, quantization, time delay, and coulomb effects", *IEEE Trans. on Robotics*, vol. 22, no. 2, pp. 256–268, 2006.

[19] F. Dimeas, V. C. Moulianitis, and N. Aspragathos, "Manipulator performance constraints in human-robot cooperation", *Robotics and Computer-Integrated Manufacturing*, vol. 50, pp. 222–233, 2018, ISSN: 0736-5845.

[20] J. Feng, X. Li, et al., "Virtual fixtures assistance for safe polyp dissection in minimally invasive robotic surgery", in *2021 5th International Conference on Automation, Control and Robots (ICACR)*, IEEE, 2021, pp. 150–155.

[21] Z. Li, A. Gordon, T. Looi, J. Drake, C. Forrest, and R. H. Taylor, "Anatomical mesh-based virtual fixtures for surgical robots", in *2020 IEEE/RSJ International Conference on Intelligent Robots and Systems (IROS)*, IEEE, 2020, pp. 3267–3273.

[22] A. Sharp and M. Pryor, "Virtual fixture generation for task planning with complex geometries", *Journal of computing and information science in engineering*, vol. 21, no. 6, p. 061 001, 2021.

[23] S. Calinon and A. Billard, "Active teaching in robot programming by demonstration", in *RO-MAN 2007-The 16th IEEE International Symposium on Robot and Human Interactive Communication*, IEEE, 2007, pp. 702–707.

[24] M. Selvaggio, G. A. Fontanelli, F. Ficuciello, L. Villani, and B. Siciliano, "Passive virtual fixtures adaptation in minimally invasive robotic surgery", *IEEE Robotics and Automation Letters*, vol. 3, no. 4, pp. 3129–3136, 2018.

[25] X. Duan et al., "Virtual-fixture based drilling control for robot-assisted craniotomy: Learning from demonstration", *IEEE Robotics and Automation Letters*, vol. 6, no. 2, pp. 2327–2334, 2021.

[26] R. Moccia, C. Iacono, B. Siciliano, and F. Ficuciello, "Vision-based dynamic virtual fixtures for tools collision avoidance in robotic surgery", *IEEE Robotics and Automation Letters*, vol. 5, no. 2, pp. 1650–1655, 2020.

[27] M. Selvaggio, G. Notomista, F. Chen, B. Gao, F. Trapani, and D. Caldwell, "Enhancing bilateral teleoperation using camera-based online virtual fixtures generation", in *2016 IEEE/RSJ International Conference on Intelligent Robots and Systems (IROS)*, IEEE, 2016, pp. 1483–1488.

[28] A. Billard, S. Calinon, R. Dillmann, and S. Schaal, "Survey: Robot programming by demonstration", *Springer handbook of robotics*, pp. 1371–1394, 2008.

[29] R. Wang, Y. Wu, W. L. Chan, and K. P. Tee, "Dynamic movement primitives plus: For enhanced reproduction quality and efficient trajectory modification using truncated kernels and local biases", in *2016 IEEE/RSJ International Conference on Intelligent Robots and Systems (IROS)*, 2016, pp. 3765–3771.

[30] W. Si, N. Wang, and C. Yang, "A review on manipulation skill acquisition through teleoperation-based learning from demonstration", *Cognitive Computation and Systems*, vol. 3, no. 1, pp. 1–16, 2021.

[31] Y. Wang et al., "A guiding and positioning motion strategy based on a new conical virtual fixture for robot-assisted oral surgery", *Machines*, vol. 11, no. 1, 2023, ISSN: 2075-1702.

[32] G. Braglia, S. Calinon, and L. Biagiotti, "A minimum-jerk approach to handle singularities in virtual fixtures", *IEEE Robotics and Automation Letters*, 2024, doi:10.1109/LRA.2024.3469814.

[33] M. Dyck, A. Sachtler, J. Klodmann, and A. Albu-Schäffer, "Impedance control on arbitrary surfaces for ultrasound scanning using discrete differential geometry", *IEEE Robotics and Automation Letters*, vol. 7, no. 3, pp. 7738–7746, 2022.

[34] T. Kastritsi and Z. Doulgeri, "A passive admittance controller to enforce remote center of motion and tool spatial constraints with application in hands-on surgical procedures", *Robotics and Autonomous Systems*, vol. 152, p. 104 073, 2022.

[35] J. Wang, S. Yang, H. Liu, C. Lu, and Y. Shen, "Dynamic control with a remote center-of-motion constraint for human–robot collaboration", *Robotics and Computer-Integrated Manufacturing*, vol. 96, p. 103 060, 2025.

[36] D. Papageorgiou, S. Stavridis, C. Papakonstantinou, and Z. Doulgeri, "Task geometry aware assistance for kinesthetic teaching of redundant robots", in *2021 IEEE/RSJ International Conference on Intelligent Robots and Systems (IROS)*, 2021, pp. 7285–7291.

[37] W. Hu, X. Pan, and H. Wang, "Proxy-based guidance virtual fixtures with orientation constraints", *International Journal of Intelligent Robotics and Applications*, pp. 1–11, 2024.

[38] J. Wang, C. Lu, Y. Lv, S. Yang, M. Zhang, and Y. Shen, "Task space compliant control and six-dimensional force regulation toward automated robotic ultrasound imaging", *IEEE Transactions on Automation Science and Engineering*, 2023.

[39] D. Bazzi, F. Roveda, A. M. Zanchettin, and P. Rocco, "A unified approach for virtual fixtures and goal-driven variable admittance control in manual guidance applications", *IEEE Robotics and Automation Letters*, vol. 6, no. 4, pp. 6378–6385, 2021.

[40] F. Shao and F. Ficuciello, "An intuitive manual guidance scheme to operate rotation and translation simultaneously", in *2024 IEEE International Conference on Robotics and Automation (ICRA)*, IEEE, 2024, pp. 15 180–15 186.

[41] Y. Cai, P. Choi, C.-W. V. Hui, R. H. Taylor, and K. W. S. Au, "A task space virtual fixture architecture for teleoperated surgical system with slave joint limit constraints", *IEEE/ASME Transactions on Mechatronics*, vol. 27, no. 1, pp. 69–80, 2021.

[42] B. Bischof, T. Glück, M. Böck, and A. Kugi, "A path/surface following control approach to generate virtual fixtures", *IEEE Transactions on Robotics*, vol. 34, no. 6, pp. 1577–1592, 2018.

[43] D. Nicolis, A. M. Zanchettin, and P. Rocco, "A hierarchical optimization approach to robot teleoperation and virtual fixtures rendering", *IFAC-PapersOnLine*, vol. 50, no. 1, pp. 5672–5679, 2017, 20th IFAC World Congress, ISSN: 2405-8963.

[44] O. Khatib, "Real-time obstacle avoidance for manipulators and mobile robots", *The international journal of robotics research*, vol. 5, no. 1, pp. 90–98, 1986.

[45] S. M. Khansari-Zadeh and O. Khatib, "Learning potential functions from human demonstrations with encapsulated dynamic and compliant behaviors", *Autonomous Robots*, vol. 41, pp. 45–69, 2017.

[46] T. Kastritsi, D. Papageorgiou, and Z. Doulgeri, "On the stability of robot kinesthetic guidance in the presence of active constraints", in *2018 European Control Conference (ECC)*, 2018, pp. 622–627.

[47] N. Turro and O. Khatib, "Haptically augmented teleoperation", in *Experimental Robotics VII*, Springer, 2001, pp. 1–10.

[48] M. Saveriano and D. Lee, "Incremental skill learning of stable dynamical systems", in *2018 IEEE/RSJ International Conference on Intelligent Robots and Systems (IROS)*, 2018, pp. 6574–6581.

[49] M. Saveriano, "An energy-based approach to ensure the stability of learned dynamical systems", in *2020 IEEE International Conference on Robotics and Automation (ICRA)*, 2020, pp. 4407–4413.

[50] A. J. Ijspeert, J. Nakanishi, H. Hoffmann, P. Pastor, and S. Schaal, "Dynamical movement primitives: Learning attractor models for motor behaviors", *Neural computation*, 2013.

[51] M. Saveriano, F. J. Abu-Dakka, A. Kramberger, and L. Peternel, "Dynamic movement primitives in robotics: A tutorial survey", *The International Journal of Robotics Research*, vol. 42, no. 13, pp. 1133–1184, 2023.

[52] G. Braglia, D. Tebaldi, and L. Biagiotti, "Phase-independent dynamic movement primitives with applications to human–robot co-manipulation and time optimal planning", *Robotics and Autonomous Systems*, vol. 194, p. 105 120, 2025, ISSN: 0921-8890.

[53] A. Sidiropoulos and Z. Doulgeri, "A reversible dynamic movement primitive formulation", in *2021 IEEE International Conference on Robotics and Automation (ICRA)*, IEEE, 2021, pp. 3147–3153.

[54] F. Dimeas, F. Fotiadis, D. Papageorgiou, A. Sidiropoulos, and Z. Doulgeri, "Towards progressive automation of repetitive tasks through physical human-robot interaction", in *Human Friendly Robotics: 10th International Workshop*, Springer, 2019, pp. 151–163.

[55] A. Kramberger, E. Shahriari, A. Gams, B. Nemec, A. Ude, and S. Haddadin, "Passivity based iterative learning of admittance-coupled dynamic movement primitives for interaction with changing environments", in *2018 IEEE/RSJ International Conference on Intelligent Robots and Systems (IROS)*, IEEE, 2018, pp. 6023–6028.

[56] S. Calinon, *Robot programming by demonstration*. EPFL Press, 2009.

[57] D. Lee and C. Ott, "Incremental kinesthetic teaching of motion primitives using the motion refinement tube", *Autonomous Robots*, vol. 31, pp. 115–131, 2011.

[58] S. Calinon, F. Guenter, and A. Billard, "On learning, representing, and generalizing a task in a humanoid robot", *IEEE Transactions on Systems, Man, and Cybernetics, Part B (Cybernetics)*, vol. 37, no. 2, pp. 286–298, 2007.

[59] G. Raiola et al., "Co-manipulation with a library of virtual guiding fixtures", *Autonomous Robots*, vol. 42, pp. 1037–1051, 2018.

[60] M. Cheng, R. Li, R. Ding, and S. Luo, "Dynamic guidance virtual fixture for hydraulic manipulator via learning from demonstration", *Proceedings of the Institution of Mechanical Engineers, Part C*, vol. 237, no. 4, pp. 952–962, 2023.

[61] J. Mirabel and F. Lamiraux, "Handling implicit and explicit constraints in manipulation planning", in *Robotics: Science and Systems 2018*, Pittsburg, United States, Jun. 2018, 9p. [Online]. Available: https://hal.science/hal-01804774.

[62] L. Zhang, S. Guo, and Q. Sun, "An assist-as-needed controller for passive, assistant, active, and resistive robot-aided rehabilitation training of the upper extremity", *Applied Sciences*, vol. 11, no. 1, p. 340, 2020.

[63] J. Abbott, G. Hager, and A. Okamura, "Steady-hand teleoperation with virtual fixtures", in *The 12th IEEE International Workshop on Robot and Human Interactive Communication, 2003. Proceedings. ROMAN 2003.*, 2003, pp. 145–151. DOI: 10.1109/ROMAN.2003.1251824.

[64] A. Bettini, P. Marayong, S. Lang, A. M. Okamura, and G. D. Hager, "Vision-assisted control for manipulation using virtual fixtures", *IEEE Transactions on Robotics*, vol. 20, no. 6, pp. 953–966, 2004.

[65] M. Sagardia and T. Hulin, "Fast and accurate distance, penetration, and collision queries using point-sphere trees and distance fields", in *SIGGRAPH 2013*, Jul. 2013. DOI: 10.1145/2503385.2503476. [Online]. Available: https://elib.dlr.de/82751/.

[66] M. Sagardia and T. Hulin, "A fast and robust six-dof god object heuristic for haptic rendering of complex models with friction", in *ACM Symposium on Virtual Reality Software and Technology (VRST)*, Nov. 2016, pp. 163–172. DOI: 10.1145/2993369.2993374. [Online]. Available: https://elib.dlr.de/107438/.

[67] D. Onfiani, M. Caramaschi, L. Biagiotti, and F. Pini, "Optimizing design and control methods for using collaborative robots in upper limb rehabilitation", *IEEE/ASME Transactions on Mechatronics*, 2025.

[68] L. Biagiotti, R. Meattini, D. Chiaravalli, G. Palli, and C. Melchiorri, "Robot programming by demonstration: Trajectory learning enhanced by semg-based user hand stiffness estimation", *IEEE Transactions on Robotics*, vol. 39, no. 4, pp. 3259–3278, 2023.

[69] P. Pastor, H. Hoffmann, T. Asfour, and S. Schaal, "Learning and generalization of motor skills by learning from demonstration", in *2009 IEEE International Conference on Robotics and Automation*, IEEE, 2009, pp. 763–768.

[70] T. Ga***v***spar, B. Nemec, J. Morimoto, and A. Ude, "Skill learning and action recognition by arc-length dynamic movement primitives", *Robotics and Autonomous Systems*, vol. 100, pp. 225–235, 2018.

[71] G. Braglia, D. Onfiani, D. Tebaldi, A. E. Lazzaretti, and L. Biagiotti, "Spatial sampling for alignment of robot demonstrated trajectories in upper limb rehabilitation tasks", in *8th Conference on Robot Learning (CoRL 2024)*, Workshop on Learning for Caregiving Robots (CoRoboLearn), Munich, Germany, 2024.

[72] M. Müller, "Dynamic time warping", in *Information retrieval for music and motion*, Springer, 2007, pp. 69–84.

[73] P. Senin, "Dynamic time warping algorithm review", *Information and Computer Science Department University of Hawaii at Manoa Honolulu, USA*, vol. 855, no. 1-23, p. 40, 2008.

[74] G. Braglia, D. Tebaldi, A. E. Lazzaretti, and L. Biagiotti, "Arc-length-based warping for robot skill synthesis from multiple demonstrations", *arXiv preprint arXiv:2410.13322*, 2024.

[75] H. Su, A. Mariani, S. E. Ovur, A. Menciassi, G. Ferrigno, and E. De Momi, "Toward teaching by demonstration for robot-assisted minimally invasive surgery", *IEEE Transactions on Automation Science and Engineering*, vol. 18, no. 2, pp. 484–494, 2021.

[76] J. Zheng et al., "A gmm-dtw-based locomotion mode recognition method in lower limb exoskeleton", *IEEE Sensors Journal*, vol. 22, no. 20, pp. 19 556–19 566, 2022.

[77] G. Braglia, D. Tebaldi, and L. Biagiotti, "Phase-free dynamic movement primitives applied to kinesthetic guidance in robotic co-manipulation tasks", *arXiv preprint arXiv:2401.08238*, 2024.

[78] D. Onfiani, M. Caramaschi, L. Biagiotti, and F. Pini, "Path-constrained admittance control of human-robot interaction for upper limb rehabilitation", in *Social Robotics: 13th International Conference, ICSR 2021*, Springer, 2022, pp. 143–153.

[79] D. Onfiani, M. Dyck, L. Biagiotti, and J. Klodmann, *Emg-based adaptation of anisotropic virtual fixtures for surgical resection and dissection*, Submitted for publication, 2025.

[80] A. Van der Schaft, *L2-gain and passivity techniques in nonlinear control*. Springer, 2000.

[81] A. Albu-Schäffer, C. Ott, and G. Hirzinger, "A unified passivity-based control framework for position, torque and impedance control of flexible joint robots", *The International Journal of Robotics Research*, vol. 26, no. 1, pp. 23–39, 2007.

[82] A. Dietrich, C. Ott, and A. Albu-Schäffer, "Multi-objective compliance control of redundant manipulators: Hierarchy, control, and stability", in *2013 IEEE/RSJ International Conference on Intelligent Robots and Systems*, IEEE, 2013, pp. 3043–3050.

[83] A. Q. Keemink, H. Van der Kooij, and A. H. Stienen, "Admittance control for physical human–robot interaction", *The International Journal of Robotics Research*, vol. 37, no. 11, pp. 1421–1444, 2018.

[84] B. Siciliano, L. Sciavicco, L. Villani, and G. Oriolo, *Robotics: Modelling, Planning and Control*, 1st. Springer Publishing Company, Incorporated, 2008.

[85] G. Braglia, D. Tebaldi, and L. Biagiotti, "Phase-independent dynamic movement primitives with applications to human–robot co-manipulation and time optimal planning", *Robotics and Autonomous Systems*, vol. 194, p. 105 120, 2025, ISSN: 0921-8890.

[86] E. Shahriari, P. Svarny, S. A. B. Birjandi, M. Hoffmann, and S. Haddadin, "Path-constrained haptic motion guidance via adaptive phase-based admittance control", *IEEE Transactions on Robotics*, 2024.

[87] D. Tebaldi, D. Onfiani, and L. Biagiotti, "On the analysis of stability, sensitivity and transparency in variable admittance control for phri enhanced by virtual fixtures", in *2025 IEEE/RSJ International Conference on Intelligent Robots and Systems (IROS)*, 2025, pp. 16 665–16 672. DOI: 10.1109/IROS60139.2025.11246940.

[88] A. Peer and M. Buss, "Robust stability analysis of bilateral teleoperation systems using admittance-type devices", in *2008 SICE Annual Conference*, 2008, pp. 2883–2889.

[89] D. Surdilovic, "Contact transition stability in the impedance control", in *Proceedings of International Conference on Robotics and Automation*, vol. 1, 1997, 847–852 vol.1.

[90] T. Tsumugiwa, R. Yokogawa, and K. Hara, "Variable impedance control based on estimation of human arm stiffness for human-robot cooperative calligraphic task", in *Proceedings 2002 IEEE International Conference on Robotics and Automation (Cat. No.02CH37292)*, vol. 1, 2002, 644–650 vol.1.

[91] F. Dimeas and N. Aspragathos, "Online stability in human-robot cooperation with admittance control", *IEEE Transactions on Haptics*, vol. 9, no. 2, pp. 267–278, 2016.

[92] W. Gallagher, D. Gao, and J. Ueda, "Improved stability of haptic human–robot interfaces using measurement of human arm stiffness", *Advanced Robotics*, vol. 28, no. 13, pp. 869–882, 2014.

[93] Y.-H. Wang, G.-Y. Liu, G. Huang, and Y. Wang, "Variable admittance force feedback device and its human-robot interaction stability", *Robotics and Computer-Integrated Manufacturing*, vol. 82, p. 102 537, 2023.

[94] D. Ryu, J.-B. Song, S. Kang, and M. Kim, "Frequency domain stability observer and active damping control for stable haptic interaction", *IET Control Theory & Applications*, vol. 2, no. 4, pp. 261–268, 2008.

[95] S. Grafakos, F. Dimeas, and N. Aspragathos, "Variable admittance control in phri using emg-based arm muscles co-activation", in *2016 IEEE International Conference on Systems, Man, and Cybernetics (SMC)*, 2016, pp. 001 900–001 905.

[96] F. Ferraguti, C. Talignani Landi, L. Sabattini, M. Bonfe, C. Fantuzzi, and C. Secchi, "A variable admittance control strategy for stable physical human–robot interaction", *The International Journal of Robotics Research*, vol. 38, no. 6, pp. 747–765, 2019.

[97] A. Topini, W. Sansom, N. Secciani, L. Bartalucci, A. Ridolfi, and B. Allotta, "Variable admittance control of a hand exoskeleton for virtual reality-based rehabilitation tasks", *Frontiers in neurorobotics*, vol. 15, p. 789 743, 2022.

[98] P. Rocco, G. Ferretti, and G. Magnani, "Implicit force control for industrial robots in contact with stiff surfaces", *Automatica*, vol. 33, no. 11, pp. 2041–2047, 1997, ISSN: 0005-1098.

[99] G. F. Franklin, J. D. Powell, A. Emami-Naeini, and J. D. Powell, *Feedback control of dynamic systems*. Prentice hall Upper Saddle River, 2002, vol. 4.

[100] T. Tsumugiwa, Y. Fuchikami, A. Kamiyoshi, R. Yokogawa, and K. Yoshida, "Stability analysis for impedance control of robot in human-robot cooperative task system", *Journal of Advanced Mechanical Design, Systems, and Manufacturing*, vol. 1, no. 1, pp. 113–121, 2007.

[101] H. Ur, "Root locus properties and sensitivity relations in control systems", *IRE Transactions on Automatic Control*, vol. AC-5, no. 1, pp. 57–65, 1960.

[102] H. Kim and W. Yang, "Variable admittance control based on human–robot collaboration observer using frequency analysis for sensitive and safe interaction", *Sensors*, vol. 21, no. 5, p. 1899, 2021.

[103] A. Lecours, B. Mayer-St-Onge, and C. Gosselin, "Variable admittance control of a four-degree-of-freedom intelligent assist device", in *2012 IEEE international conference on robotics and automation*, 2012, pp. 3903–3908.

[104] R. Gassert and V. Dietz, "Rehabilitation robots for the treatment of sensorimotor deficits: A neurophysiological perspective", *Journal of neuroengineering and rehabilitation*, 2018.

[105] T. Nef, M. Guidali, and R. Riener, "Armin iii–arm therapy exoskeleton with an ergonomic shoulder actuation", *Applied Bionics and Biomechanics*, 2009.

[106] T. G. Sugar et al., "Design and control of rupert: A device for robotic upper extremity repetitive therapy", *IEEE transactions on neural systems and rehabilitation engineering*, 2007.

[107] S. Crea et al., "A novel shoulder-elbow exoskeleton with series elastic actuators", in *IEEE International Conference on Biomedical Robotics and Biomechatronics (BioRob)*, 2016.

[108] H. Krebs and B. Volpe, "Rehabilitation robotics", *Handbook of clinical neurology*, vol. 110, pp. 283–294, 2013.

[109] R. Loureiro, F. Amirabdollahian, M. Topping, B. Driessen, and W. Harwin, "Upper limb robot mediated stroke therapy—gentle/s approach", *Autonomous Robots*, 2003.

[110] A. Toth, D. Nyitrai, M. Jurak, I. Merksz, G. Fazekas, and Z. Denes, "Safe robot therapy: Adaptation and usability test of a three-position enabling device for use in robot mediated physical therapy of stroke", in *2009 IEEE International Conference on Rehabilitation Robotics*, 2009.

[111] A. Bertomeu-Motos, A. Blanco, F. J. Badesa, J. A. Barios, L. Zollo, and N. Garcia-Aracil, "Human arm joints reconstruction algorithm in rehabilitation therapies assisted by end-effector robotic devices", *Journal of neuroengineering and rehabilitation*, 2018.

[112] L. Zhang, S. Guo, and Q. Sun, "Development and assist-as-needed control of an end-effector upper limb rehabilitation robot", *Applied Sciences*, 2020.

[113] J. Mehrholz, A. Hädrich, T. Platz, J. Kugler, and M. Pohl, "Electromechanical and robot-assisted arm training for improving generic activities of daily living, arm function, and arm muscle strength after stroke", *Cochrane database of systematic reviews*, 2012.

[114] P. Maciejasz, J. Eschweiler, K. Gerlach-Hahn, A. Jansen-Troy, and S. Leonhardt, "A survey on robotic devices for upper limb rehabilitation", *Journal of NeuroEngineering and Rehabilitation*, 2014.

[115] Z. Qian and Z. Bi, "Recent development of rehabilitation robots", *Advances in Mechanical Engineering*, 2015.

[116] B. Siciliano, O. Khatib, and T. Kröger, *Springer handbook of robotics*. Springer, 2008.

[117] M. Caramaschi, D. Onfiani, F. Pini, L. Biagiotti, and F. Leali, "Workspace placement of motion trajectories by manipulability index for optimal design of cobot assisted rehabilitation solutions", *Computer-Aided Design and Applications*, pp. 1–12, 2022.

[118] F. Ficuciello, A. Romano, L. Villani, and B. Siciliano, "Cartesian impedance control of redundant manipulators for human-robot co-manipulation", in *IEEE/RSJ International Conference on Intelligent Robots and Systems*, 2014.

[119] C. Tamantini et al., "Patient-tailored adaptive control for robot-aided orthopaedic rehabilitation", in *International Conference on Robotics and Automation (ICRA)*, IEEE, 2022.

[120] Z. Pezzementi, A. M. Okamura, and G. D. Hager, "Dynamic guidance with pseudoadmittance virtual fixtures", in *IEEE International Conference on Robotics and Automation*, 2007, pp. 1761–1767.

[121] D. Papageorgiou, T. Kastritsi, Z. Doulgeri, and G. A. Rovithakis, "A passive phri controller for assisting the user in partially known tasks", *IEEE Transactions on Robotics*, vol. 36, no. 3, pp. 802–815, 2020.

[122] L. Zhang, S. Guo, and Q. Sun, "An assist-as-needed controller for passive, assistant, active, and resistive robot-aided rehabilitation training of the upper extremity", *Applied Sciences*, vol. 11, no. 1, 2021.

[123] C. Zilles and J. Salisbury, "A constraint-based god-object method for haptic display", in *Proceedings 1995 IEEE/RSJ International Conference on Intelligent Robots and Systems. Human Robot Interaction and Cooperative Robots*, vol. 3, 1995, 146–151 vol.3.

[124] J. Aleotti and S. Caselli, "Robust trajectory learning and approximation for robot programming by demonstration", *Robotics and Autonomous Systems*, 2006.

[125] L. Biagiotti and C. Melchiorri, *Trajectory Planning for Automatic Machines and Robots*, first. Heidelberg, Germany: Springer, 2008.

[126] T. Yoshikawa, "Manipulability of robotic mechanisms", *The international journal of Robotics Research*, vol. 4, no. 2, pp. 3–9, 1985.

[127] P. Chiacchio, Y. Bouffard-Vercelli, and F. Pierrot, "Force polytope and force ellipsoid for redundant manipulators", *Journal of Robotic Systems*, vol. 14, no. 8, pp. 613–620, 1997.

[128] C.-H. Lin, Y.-Y. Su, Y.-H. Lai, and C.-C. Lan, "A spatial-motion assist-as-needed controller for the passive, active, and resistive robot-aided rehabilitation of the wrist", *IEEE Access*, 2020.

[129] J. Zhang and C. C. Cheah, "Passivity and stability of human–robot interaction control for upper-limb rehabilitation robots", *IEEE Transactions on Robotics*, 2015.

[130] S. Y. A. Mounis, N. Z. Azlan, and F. Sado, "Assist-as-needed control strategy for upper-limb rehabilitation based on subject's functional ability", *Measurement and Control*, 2019.

[131] M. Najafi, C. Rossa, K. Adams, and M. Tavakoli, "Using potential field function with a velocity field controller to learn and reproduce the therapist's assistance in robot-assisted rehabilitation", *IEEE/ASME Transactions on Mechatronics*, 2020.

[132] C. Rossa, M. Najafi, M. Tavakoli, and K. Adams, "Robotic rehabilitation and assistance for individuals with movement disorders based on a kinematic model of the upper limb", *IEEE Transactions on Medical Robotics and Bionics*, vol. 3, no. 1, pp. 190–203, 2021.

[133] A. Albu-Schaffer, C. Ott, U. Frese, and G. Hirzinger, "Cartesian impedance control of redundant robots: Recent results with the dlr-light-weight-arms", in *2003 IEEE International Conference on Robotics and Automation*, vol. 3, 2003, 3704–3709 vol.3.

[134] M. Dyck, A. Jazayeri, and M. Tavakoli, "Is the human operator in a teleoperation system passive?", in *2013 World Haptics Conference (WHC)*, 2013, pp. 683–688.

[135] R. Anderson and M. Spong, "Asymptotic stability for force reflecting teleoperators with time delays", IEEE, 2023.

[136] K. P. Tee, S. S. Ge, and E. H. Tay, "Barrier lyapunov functions for the control of output-constrained nonlinear systems", 2009.

[137] H. J. Asl, T. Narikiyo, and M. Kawanishi, "An assist-as-needed velocity field control scheme for rehabilitation robots", in *2018 International Conference on Intelligent Robots and Systems (IROS)*, IEEE, 2018.

[138] H. R. Z. L. Q. W. D. Wu, "Guidance priority adaptation in human-robot shared control", in *2022 IEEE International Conference on Mechatronics and Automation (ICMA) —*, IEEE, 2022.

[139] S. G. Hart and L. E. Staveland, "Development of nasa-tlx (task load index): Results of empirical and theoretical research", in *Advances in psychology*, vol. 52, Elsevier, 1988, pp. 139–183.

[140] M. Tonutti, D. Elson, et al., "The role of technology in minimally invasive surgery: State of the art, recent developments and future directions", *Postgraduate medical journal*, vol. 93, no. 1097, pp. 159–167, 2017.

[141] G. Dagnino and D. Kundrat, "Robot-assistive minimally invasive surgery: Trends and future directions", *International Journal of Intelligent Robotics and Applications*, vol. 8, no. 4, pp. 812–826, 2024.

[142] M. Van Det, W. Meijerink, et al., "Optimal ergonomics for laparoscopic surgery in minimally invasive surgery suites: A review and guidelines", *Surgical endoscopy*, vol. 23, no. 6, pp. 1279–1285, 2009.

[143] J. Klodmann, C. Schlenk, et al., "An introduction to robotically assisted surgical systems: Current developments and focus areas of research", *Current Robotics Reports*, vol. 2, no. 3, pp. 321–332, 2021.

[144] B. van Amsterdam, M. J. Clarkson, et al., "Gesture recognition in robotic surgery: A review", *IEEE Transactions on Biomedical Engineering*, vol. 68, no. 6, 2021.

[145] B. Davies, S. Harris, et al., "Active compliance in robotic surgery—the use of force control as a dynamic constraint", *Proceedings of the Institution of Mechanical Engineers, Part H: Journal of Engineering in Medicine*, vol. 211, no. 4, pp. 285–292, 1997.

[146] M. M. Marinho, B. V. Adorno, et al., "Active constraints using vector field inequalities for surgical robots", in *2018 IEEE International Conference on Robotics and Automation (ICRA)*, IEEE, 2018, pp. 5364–5371.

[147] A. Lin, Y. Tang, et al., "A virtual fixtures control method of surgical robot based on human arm kinematics model", *IEEE Access*, vol. 7, pp. 135 656–135 664, 2019.

[148] R. Moccia, M. Selvaggio, L. Villani, B. Siciliano, and F. Ficuciello, "Vision-based virtual fixtures generation for robotic-assisted polyp dissection procedures", in *2019 IEEE/RSJ International Conference on Intelligent Robots and Systems (IROS)*, IEEE, 2019, pp. 7934–7939.

[149] M. Shahbazi, S. F. Atashzar, et al., "A dual-user teleoperated system with virtual fixtures for robotic surgical training", in *2013 IEEE International Conference on Robotics and Automation*, IEEE, 2013, pp. 3639–3644.

[150] R. Arduini, Y. Michel, et al., "Learning from demonstration of robot motions and stiffness behaviors for surgical blunt dissection", in *2024 33rd IEEE International Conference on Robot and Human Interactive Communication (ROMAN)*, IEEE, 2024, pp. 1491–1496.

[151] Y. Fan, J. Luo, et al., "A regulable linear guidance flexible virtual fixture based on EMG in teleoperation system", in *2021 26th International Conference on Automation and Computing (ICAC)*, IEEE, 2021, pp. 1–6.

[152] F. Patriarca, P. Di Lillo, et al., "EMG-driven shared control architecture for human–robot co-manipulation tasks", *Machines*, vol. 13, no. 8, p. 669, 2025.

[153] S. Rawat, S. Vats, et al., "Evaluating and exploring the myo armband", in *2016 International Conference System Modeling & Advancement in Research Trends (SMART)*, IEEE, 2016, pp. 115–120.

[154] U. Seibold, B. Kübler, T. Bahls, R. Haslinger, and F. Steidle, "The DLR mirosurge surgical robotic demonstrator", in *The Encyclopedia of MEDICAL ROBOTICS: Volume 1 Minimally Invasive Surgical Robotics*, World Scientific, 2019, pp. 111–142.

[155] S. Müller-Spahn, "Further development of a backdrivable linear axis for collaborative laparoscopic surgery", M.S. thesis, Institut für Robotik und Mechatronik, 2024. [Online]. Available: https://elib.dlr.de/204413/.

[156] L. Le Tien, A. A. Schaffer, and G. Hirzinger, "Mimo state feedback controller for a flexible joint robot with strong joint coupling", in *Proceedings 2007 IEEE International Conference on Robotics and Automation*, IEEE, 2007, pp. 3824–3830.

[157] L. Le Tien, A. Albu-Schaffer, A. De Luca, and G. Hirzinger, "Friction observer and compensation for control of robots with joint torque measurement", in *2008 IEEE/RSJ International Conference on Intelligent Robots and Systems*, IEEE, 2008, pp. 3789–3795.

[158] A. Dietrich and C. Ott, "Hierarchical impedance-based tracking control of kinematically redundant robots", *IEEE Transactions on Robotics*, vol. 36, no. 1, pp. 204–221, 2019.

[159] A. Albu-Schaffer, C. Ott, U. Frese, and G. Hirzinger, "Cartesian impedance control of redundant robots: Recent results with the dlr-light-weight-arms", in *2003 IEEE International Conference on Robotics and Automation (Cat. No.03CH37422)*, vol. 3, 2003, 3704–3709 vol.3. DOI: 10.1109/ROBOT.2003.1242165.

[160] Lübeck Toolbox Ltd., *Lübecker toolbox training exercises*, http://www.luebeck-toolbox.com/training.html, Accessed: 2024-01-24.

[161] M. Thomaschewski, T. Laubert, et al., "Efficacy of goal-directed minimally invasive surgery simulation training with the lübeck toolbox-curriculum prior to first operations on patients: Study protocol for a multi-centre randomized controlled validation trial (novice)", *International Journal of Surgery Protocols*, vol. 21, pp. 13–20, 2020.

[162] M. Thomaschewski, M. Kist, et al., "Conception and prospective multicentric validation of a robotic surgery training curriculum (rostrac) for surgical residents: From simulation via laboratory training to integration into the operation room", *Journal of Robotic Surgery*, vol. 18, no. 1, p. 18, 2024. DOI: 10.1007/s11701-023-01813-6.

[163] R. Budiu. "Between-subjects vs. within-subjects study design". Accessed: 2025-02-26, Nielsen Norman Group. [Online]. Available: https://www.nngroup.com/articles/between-within-subjects/.

[164] J. Brooke, "SUS: A quick and dirty usability scale", Digital Equipment Co., Reading, UK, Tech. Rep. TR-26, 1996.

[165] R. H. Baayen, D. J. Davidson, et al., "Mixed-effects modeling with crossed random effects for subjects and items", *Journal of memory and language*, vol. 59, no. 4, pp. 390–412, 2008.

[166] S. Haddadin, A. Albu-Schaffer, et al., "Collision detection and reaction: A contribution to safe physical human-robot interaction", in *2008 IEEE/RSJ International Conference on Intelligent Robots and Systems*, IEEE, 2008, pp. 3356–3363.

[167] A. Bangor, P. T. Kortum, et al., "An empirical evaluation of the system usability scale", *International Journal of Human-Computer Interaction*, vol. 24, no. 6, pp. 574–594, 2008.